

# **X-ray Imaging of Three-dimensional Spatial Structure of Coatings**

A dissertation presented by

Bo Chen

Submitted for the requirements for  
the degree of Doctor of Philosophy  
at University College London

Supervised by  
Prof. Dr. Ian K. Robinson



London Centre for Nanotechnology  
& Department of Physics and Astronomy  
University College London  
September, 2012

Copyright © 2012 by Bo Chen

All rights reserved.

## DECLARATION

---

I, Bo Chen, confirm that the work presented in this dissertation is my own. Where information has been derived from other sources, I confirm that this has been indicated in the dissertation.

---

Bo Chen

September 2012

To my dear mother and FATHER.

献给我敬爱的父亲与母亲！

The world is colourful, and the coatings contribute!

## **Abstract**

Bo Chen: X-ray Imaging of Three-dimensional Spatial Structure of Coatings

(Under the direction of Prof. Ian K. Robinson)

Coatings, typically painted films, one of the most important and widely-used surface treatment materials, were selected as the subject of this research project. In this dissertation, detailed three-dimensional (3D) spatial structures of three types of coating specimens: silver epoxy adhesive, iron oxide alkyd paint and aluminium epoxy marine coating were obtained by using different 3D X-ray imaging methods and comparative 3D electron imaging means. The shapes and spatial distributions of particles of the main functional ingredients of all these coating specimens were demonstrated. Specifically, for the aluminium epoxy marine coating, the quantitative analysis of the sizes, volumes, orientations and spatial distributions and correlations of the aluminium flakes in the matrix materials of the coating were carried out. Furthermore, the 3D structures of the aluminium epoxy marine coating samples were used for the finite element simulations of the (ion) percolation properties of the coating film. This potentially provides us a practical method to engineer the efficacy of coatings by modelling their performances based on the actual structures instead of using assumed model structures. This is a new way to evaluate the performance of materials, and also can be an approach for validating their mechanistic assumptions. It could help to shorten the product research and development lifetime, complementing endurance studies of original specimens. The work presented in the dissertation is the first systematic research of 3D spatial structures of coatings and it could help guide coating researchers how to choose the most suitable 3D investigation method for a specific coating specimen.

Through comparative experiments, transmission X-ray microscopy (TXM), ptychographic X-ray computed tomography (PXCT), X-ray holo-tomography and serial block-face scanning

electron microscopy (SBFSEM) have been verified as effective ways to reveal 3D spatial structures of complex industrial specimens. A comparison among these 3D imaging approaches and their advantages and disadvantages are discussed.

The wave-front modulation coherent X-ray diffraction imaging was also implemented. It proved to be a capable method of measuring structures of coating samples and reaches similar resolution as TXM. Developing it into a 3D coherent X-ray imaging methodology with capabilities of obtaining a unique image solution from a single diffraction pattern is left as future work.

## Acknowledgements

This dissertation would not be completed without helps from many friends and exceptional persons in the last a few years.

Firstly, I would like to sincerely present my gratitude to my supervisor Prof. Ian K. Robinson, whose enthusiasm for science inspired me to do the research with passions. His profound knowledge, intelligent guidelines, friendly discussions and endless encouragement and supports on both study and life have made this work possible.

I would like to thank the financial support from the EPSRC (UK) and AkzoNobel Co. Ltd. to my PhD through a Dorothy Hodgkin Postgraduate Award (DHPA). Additional funding of the PhD work came from the European Research Council (ERC) Advanced Grant 227711 “nanosculpture”. I also acknowledge support from the European Community’s Seventh Framework Programme (FP7/2007–2013) through grant no. 226716 for funding all costs of one of my travels to Swiss Light Source, Paul Scherrer Institut, Villigen PSI, Switzerland.

I would also like to acknowledge Dr. Andrew Burgess at AkzoNobel (UK) Co. Ltd. for his role as an external industrial supervisor for the project. Acknowledgements also go to Dr. Frank Vergeer and Dr. Paul Jackson at AkzoNobel Co. Ltd. for fruitful discussions on coating materials, and Mr. Alexander Monteith at Gatan (UK) Ltd and Dr. Joel Mancuso at Gatan, Inc. for promoting work on serial block-face scanning electron microscopy.

The wave-front modulation coherent X-ray diffraction imaging experiment was carried out at the cSAXS beamline at Swiss Light Source, and was supported by a Basic Technology Grant (“Ultimate Microscopy”, EP/E034055/1), a Phase Modulation Technology for X-ray Imaging Grant (EP/I022562/1) and a facility exploitation grant (EP/F020767/1). The ptychography X-ray computed tomography experiments were also carried out at the cSAXS beamline at the

Swiss Light Source. The serial block-face scanning electron microscopy measurements were performed on the Gatan 3View system at Gatan Inc. The synchrotron X-ray based full-field transmission X-ray microscopy measurements were done at the beamline 32-ID-C of the Advanced Photon Source, an Office of Science User Facility operated for the U.S. Department of Energy (DOE) Office of Science by Argonne National Laboratory, was supported by the U.S. DOE under Contract No. DE-AC02-06CH11357.

I would also give a big thanks to the (former) members in our group, Loren Beitra, Felisa Berenguer, Jesse Clark, Xiaowen Shi, Gang Xiong and Fucai Zhang, and the scientists at the synchrotron X-ray beamlines and laboratories, Dr. Manuel Guizar-Sicairos, Dr. Ana Diaz, Dr. Yong Chu, Dr. Yuxing Wang, Dr. Peter Cloetens, Dr. Heikki Suhonen and Dr. Robert Bradley, who I worked together for their helps and supports to my daily life and work.

Finally, to my family, it is their supports throughout my whole education make me come to this point.

Bo Chen

September, 2012

University College London

# Contents

Abstract.....	6
Acknowledgements.....	8
List of Figures.....	13
List of Tables.....	15
<b>1 Introduction.....</b>	<b>16</b>
1.1 Coating History and Development.....	17
1.2 Coating Components.....	17
1.3 Specimens of Interest.....	19
References.....	20
<b>2 Three-dimensional Imaging Methods at Nano-scale.....</b>	<b>24</b>
2.1 Transmission X-ray Microscopy.....	25
2.1.1 Absorption Contrast in TXM.....	26
2.1.2 Zernike Phase Contrast in TXM.....	30
2.1.3 Transmission X-ray Microscopy (TXM) Instrumentation.....	32
2.2 Ptychographic X-ray Computed Tomography.....	40
2.3 X-ray Holo-tomography (Based on Free Space Propagation Phase Contrast).....	45
2.4 Other X-ray Imaging Techniques.....	49
2.5 Serial Block-Face Scanning Electron Microscopy (SBFSEM).....	49
2.6 Focused Ion Beam (FIB) Tomography.....	52
References.....	56
<b>3 Investigation of Three-Dimensional Spatial Structures of the Silver Epoxy Adhesive by Transmission X-ray Microscopy.....</b>	<b>65</b>

3.1 Introduction.....	65
3.2 Experiments .....	66
3.3 Results and Discussion .....	67
3.4 Conclusions and Future Work .....	70
References.....	71
<b>4 Wave-front Modulation Coherent X-ray Diffraction Imaging of the Iron Oxide Alkyd Paint .....</b>	<b>73</b>
4.1 Introduction.....	74
4.2 Experiment and Methods .....	75
4.3 Results and Discussion .....	78
4.4 Conclusions and Future Work .....	83
References.....	85
<b>5 Investigation of Three-Dimensional Spatial Structure of Iron Oxide Alkyd Paint .....</b>	<b>88</b>
5.1 Introduction.....	88
5.2 3D Spatial Structure Investigation by X-ray Holo-tomography .....	90
5.2.1 Experiments and Methods.....	90
5.2.2 Results.....	91
5.3 3D Spatial Structure Investigation by PXCT .....	93
5.3.1 Experiments and Methods.....	93
5.3.2 Results.....	94
5.4 3D Spatial Structure Investigation by TXM .....	96
5.4.1 Experiments .....	96
5.4.2 Results.....	97
5.5 3D Spatial Structure Investigation by SBFSEM.....	99

5.5.1 Experiments .....	99
5.5.2 Results .....	99
5.6 Discussions .....	100
5.7 Conclusions and Future Work .....	102
References .....	104
<b>6 Three-Dimensional Structure and Percolation Properties of a Barrier Marine Coating</b> .....	<b>106</b>
6.1 Introduction .....	107
6.2 Experiments .....	108
6.3 Results and Discussion .....	111
6.4 Conclusions .....	120
References .....	120
Author contributions of the submitted paper .....	123
<b>7 Conclusions and Future Work.....</b>	<b>124</b>
7.1 Conclusions .....	124
7.2 Future Work .....	127
Curriculum Vitae .....	130

## List of Figures

Figure 2. 1: Schematic working principle of X-ray microscope .....	26
Figure 2. 2: An X-ray beam goes through a homogenous object .....	26
Figure 2. 3: An X-ray beam goes through an inhomogeneous object .....	27
Figure 2. 4: A projection of an object to the detector .....	29
Figure 2. 5: Fourier/frequency domain parameters pertinent to parallel projection data .....	29
Figure 2. 6: Schematically optical layout of a transmission X-ray microscope .....	30
Figure 2. 7: Vector diagrams describing the amplitude and phase relations .....	32
Figure 2. 8: Pre-alignment optical microscope system of the NanoXCT .....	32
Figure 2. 9: Xradia's NanoXCT at the beamline 32-ID-C, Advanced Photon Source .....	33
Figure 2. 10: Regions of interest and reference point candidates of samples .....	36
Figure 2. 11: Photographic diagram showing the gold micro-particle transfer .....	36
Figure 2. 12: The external telescope of the Xradia's NanoXCT at the 32-ID-C, APS .....	38
Figure 2. 13: Schematic of working principle of ptychographic imaging .....	41
Figure 2. 14: Experimental set-up of ptychographic X-ray computed tomography .....	43
Figure 2. 15: A single tomogram slice of the reconstructed 3D volume from PXCT .....	44
Figure 2. 16: Free space propagation phase contrast based X-ray imaging .....	46
Figure 2. 17: Schematic diagram of the X-ray holo-tomography experimental setup .....	47
Figure 2. 18: Schematics of the holographic computed X-ray laminography setup .....	49
Figure 2. 19: Schematic presentation of working process of SBFSEM .....	50

Figure 2. 20: 3D reconstruction of all the Ni <sub>4</sub> Ti <sub>3</sub> precipitates from FIB tomography .....	53
Figure 2. 21: Topological characterization of particle–particle interfaces .....	53
Figure 2. 22: Relationships of the imaging plane with electron and ion beams .....	55
Figure 2. 23: External markers for FIB tomography .....	55
Figure 3. 1: A series of projections of a silver epoxy adhesive sample .....	68
Figure 3. 2: Rendering of the 3D image of the silver epoxy adhesive .....	69
Figure 3. 3: Tomographic cross-sections of the 3D image of the silver epoxy adhesive .....	70
Figure 4. 1: Schematic of the wave-front modulation CXDI experimental set-up .....	76
Figure 4. 2: Results from the wave-front modulation CXDI .....	80
Figure 4. 3: Schematic comparison between the algorithms .....	84
Figure 5. 1: An example of an alkyd resin.....	89
Figure 5. 2: Schematic experimental set-up of X-ray holo-tomography .....	91
Figure 5. 3: Results of the iron oxide alkyd paint from X-ray holo-tomography .....	92
Figure 5. 4: FIB fabricated iron oxide alkyd paint samples .....	94
Figure 5. 5: Results of the iron oxide alkyd paints from PXCT measurements .....	95
Figure 5. 6: TXM measurement results of the iron oxide alkyd paint applied on PE foil .....	97
Figure 5. 7: TXM measurement results of the iron oxide alkyd paint applied on PP plate ....	98
Figure 5. 8: Results of the iron oxide alkyd paint from SBFSEM measurements .....	100
Figure 6. 1: Results of the aluminium epoxy barrier marine coating from TXM .....	109
Figure 6. 2: Results for the degassed aluminium marine coating imaged by SBFSEM .....	111
Figure 6. 3: Results for the degassed coating imaged by PXCT .....	112
Figure 6. 4: Geometry of 3D coordination system .....	113
Figure 6. 5: Results for the non-degassed aluminium marine coating from PXCT .....	117
Figure 6. 6: Finite element simulation results .....	119

## List of Tables

Table 1.1: Sample information .....	20
Table 2. 1: A typical recipe of the embedding resin .....	52
Table 6. 1: Quantitative analysis of results from SBFSEM measurement .....	115
Table 6. 2: Quantitative analysis of results from PXCT measurement .....	116

# **Chapter 1**

## **Introduction**

Coatings, the most important and most widely-used surface treatment materials, covered surfaces of the majority of objects we have been touching or seeing. As the fundamental topic of materials science, the correlation between structures and performances of materials never fails to fascinate us scientists. Since material structure investigation is a three-dimensional (3D) task, it would particularly benefit materials science if structures can be revealed in three dimensions rather than just in two dimensions [1]. However, currently, characterisations of the structures of coatings is still directed by two-dimensional (2D) imaging using such as optical microscope [2], scanning electron microscope (SEM) [3-5] and transmission electron microscope (TEM) [6-8], and 3D spatial structures of coatings have hardly been investigated in details [9, 10]. Although these 2D imaging methods have been sophisticatedly employed and some of them can provide extremely high resolution, they do not feature the structures of samples in three dimensions and have high potential possibility leading us to the wrong conclusion on the real object shapes, sizes, spatial distribution and connectivity in materials which need to be characterised in three dimensions. In this dissertation, 3D spatial structure of coatings was investigated by X-ray imaging with tens of nanometre resolution. For

comparisons, 3D electron imaging was employed in the work as well. This study is the beginning part of the first systematic research of structure of coatings in three dimensions using both X-ray and electron imaging.

## **1.1 Coating History and Development**

Coating is a general term denoting any material that is applied to a surface as a thin continuous layer. The terms ‘paint’ and ‘coating’ are often used interchangeably, however, the paint was traditionally used to describe pigmented materials [11, 12].

There are thousands of years of experience of making and using coatings in human history. However, the first combination of coating and scientific technology is the Duco® nitrocellulose lacquer, the first sprayable automotive finish, which was introduced by DuPont Company in 1923 [13]. From 1930, the alkyd resins began to be produced and grew into the most important variety of coating - alkyd paints [14]. During the 1940s, the epoxy resin coating had been commercialised by Ciba Company which was a breakthrough of the anti-corrosive coating technology [15]. The electrophoretic paint had been developed in the 1950s and the polyurethane paint largely expanded in the 1960s. In the 1970s, the powder coating was highly-developed under the help of evolution of the coating technology. The discovery of the group transfer polymerization by the DuPont Company was the milestone of development of coating in the 1980s [16, 17]. From the 1990s, nanomaterial had been begun to be applied into coating industry [18], and currently coating is the third major sector for nanomaterial applications [19].

## **1.2 Coating Components**

Generally, coatings are composed by film formers, solvents and pigments [12]. Except these three main components, varieties of additives and extenders are heavily used in the modern coating manufacturing as well [12].

Film formers, which are essential roles for coatings, are also called binders or matrixes. They are usually organic polymers or resins which formed into continuous phases in materials [12] after the coatings were applied on substrates. The performances such as surface protection capabilities and mechanical properties of cured coating films are mainly determined by the film formers. Solvents are usually volatile organic liquids which work more like diluents to make the materials into liquid-dispersing phases [12]. Actually, in many cases, they are also called diluents. The main function of solvents is improving application and spreading performance of the materials, to assist the mixtures of film formers and pigments to be spread on the substrates efficiently. Another requirement to the solvents is that they should have no obvious influence to properties and performances of the cured coating films [18]. Pigments are usually powders, inorganic or organic, which provide opacification, colour and other optical or visual effects to the coatings [12]. The pigment particles are discontinuous phases in the coatings and their particle sizes are usually falling between 0.2 and 10 microns, in which range the majority of pigments generate most efficient performances under illumination of visible light [18]. In addition, pigments can also strengthen or produce some other specific properties such as anti-corrosive [20], anti-fouling [21] or self-cleaning capabilities [22]. They also can improve rheological properties of products [23].

Extenders added in coatings are tending to be relatively cheap materials. They have a particle size distribution similar to that of pigments [11], and normally are used in conjunction with pigments to achieve a specific type of coating [12] and/or to reduce manufacture cost. Paint additives are auxiliary components that are added to coatings, usually in small amounts, to improve particular technical properties of coating films [11].

Extenders and additives, even pigments and solvents are not essential components of coating materials, in extreme cases, all of them can be ignored in the coating formulas.

### **1.3 Specimens of Interest**

Currently, specimens of interest are including marine coating, decorative coating and thermally & electrically conductive coating. Aluminium epoxy barrier marine coating, iron oxide alkyd paint, and silver epoxy adhesive were selected as the representative samples, respectively. Their 3D spatial structures were revealed to characterise shapes, sizes, spatial distribution and connectivity of particles of functional components in the materials, and to explore the relationship between 3D structures and performance of the coatings. Specifically, the shapes and spatial arrangement of the aluminium flakes, main functional component of the aluminium epoxy coating, which sized around several microns wide and only few hundred nanometres thick, are aiming to be disclosed to explain percolation properties of the aluminium epoxy marine coating; the spatial distribution of iron oxide pigment particles in the iron oxide alkyd paint are aiming to be presented to clarify their relation to the coating optical properties and to help to lead the ways of producing pigment-less-consuming products to reduce the carbon footprint of coating industry; the geometrical connectivity/contact of silver grains established inside the silver epoxy adhesive [24] is aiming to be revealed to obtain physical evidence of the origin of the thermally and electrically conductive performances of the materials which is little known.

As sizes of particles of the target components are mainly ranging between few hundred nanometers and a few microns. 3D X-ray imaging methods with tens of nanometre resolution have been employed to carry out the studies, and comparative tests using 3D electron imaging were done as well.

All samples are dried coating films, which are provided by AkzoNobel Co. Ltd. The sample information is presented in the following table 1.1.

Table 1.1: Sample information

Coating Type	Representative Samples	Sample Format
Marine coating	Aluminium epoxy barrier marine coating	Non-degassed samples applied on PTFE
		Non-degassed samples applied on glass slides
		Degassed samples applied on PTFE
		Degassed samples applied on glass slides
Decorative coating	Iron oxide alkyd paint	Samples applied on PE foil and experienced 3 different mixing regimes, respectively.
		Samples applied on PP plate and experienced 3 different mixing regimes, respectively.
Thermally & electrically conductive coating	Silver epoxy adhesive	Free standing/detached film samples
		Samples applied on glass slides

In table 1.1, PTFE is the abbreviation for polytetrafluoroethylene, PE is for polyethylene and PP is for polypropylene. The 3 different mixing regimes that the iron oxide alkyd paint samples were treated are 1 minute mixing by hand, 3 minute mixing in a shaking machine as done in job-site practice and 1 hour shaking in a can with beads which is a heavily severe mixing.

## References

- [1] Möbus, G. & Inkson, B. J. Nanoscale tomography in materials science. *Materials Today*. **10**, 18-25 (2007).
- [2] Wang, Q. *et al.* Influence of carbon content on the microstructure and tribological properties of TiN(C) coatings in water lubrication. *Surface & Coatings Technology*. **206**, 3777-3787 (2012).
- [3] Bestor, M.A., Alfano, J.P. & Weaver M.L. Influences of chromium and hafnium additions on the microstructures of  $\beta$ -nial coatings on superalloy substrates. *Intermetallics*. **19**, 1693-1704 (2011).
- [4] Panjan, P., Kek Merl D., Zupanič, F., Čekada, M. & Panjan M. SEM study of defects in PVD hard coatings using focused ion beam milling. *Surface & Coatings Technology*. **202**, 2302–2305 (2008).
- [5] Wang, D., Tian, Z., Shen, L., Liu, Z. & Huang. Y. Microstructural characteristics and formation mechanism of Al<sub>2</sub>O<sub>3</sub>-13 wt.% TiO<sub>2</sub> coatings plasma-sprayed with nanostructured agglomerated powders. *Surface & Coatings Technology*. **203**, 1298-1303 (2009).
- [6] Martyak, N.M., Characterization of Thin Electroless Nickel Coatings. *Chem. Mater.* **6**, 1667-1674 (1994).
- [7] Gang, J., Morniroli, J. & Grosdidier, T. Nanostructures in thermal spray coatings. *Scripta Materialia*. **48**, 1599-1604 (2003).
- [8] Senderowski, C., Bojar, Z., Wolczyński, W. & Pawłowski, A. Microstructure characterization of D-gun sprayed Fe-Al intermetallic coatings. *Intermetallics*. **18**, 1405-1409 (2010).
- [9] Jaeggi, C., Mooser, R., Frauchiger, V. & Wyss, P. 3D characterization of open porous vacuum plasma sprayed titanium coatings by means of high resolution micro computer tomography. *Mater. Lett.* **63**, 2643-2645 (2009).

- [10] Koller, D.M., Hanneschläger, G., Leitner, M. & Khinast, J.G. Non-destructive analysis of tablet coatings with optical coherence tomography. *Eur. J. Pharm. Sci.* **44**, 142-148 (2011).
- [11] Stoye, D. & Freitag, W. *Paints, Coatings and Solvents* (2nd ed.): 1-10 (Wiley-VCH, Weinheim, New York, Basel et al., 1998).
- [12] Lambourne, R. & Strivens, T. A. *Paint and Surface Coatings-Theory and Practice* (2nd ed.): 1-18 (Woodhead Publishing Ltd., Cambridge, England, 1999).
- [13] <http://pc.dupont.com/dpc/en/US/html/common/about/dr-history.html>, and  
<http://homepage.mac.com/sljohnson/typewriter/corona/Corona-Duco.html>
- [14] Reddy, V. A., Sampathkumaran, P. S. & Gedam, P. H. Effect of oil length of alkyd on the physico-chemical properties of its coatings. *Prog. Org. Coat.* **14**, 87-97 (1986).
- [15] Kulshreshtha, A. K. & Vasile, C. *Handbook of polymer blends and composites* (Volume 1): 22 (Papra Technology Ltd., Shropshire, the U.K., 2002).
- [16] Bandermann, F. & Witkowski, R. Group transfer polymerization of methacrylonitrile. *Makromol. Chem.* **181**, 2691-2696 (1986).
- [17] Webster, O. W. The Discovery and Commercialization of Group Transfer Polymerization. *Journal of Polymer Science: Part A: Polymer Chemistry.* **38**, 2855-2860 (2000).
- [18] Hong, X. & Feng, H. *Coating Chemistry* (written in Chinese, 2nd ed.). (Science Press, Beijing, P. R. China, 2005).
- [19] Jackson, A. Nanocoatings manufacturers seek greater clarity. *Chemistry and Industry.* **16**, 18-19 (2009).
- [20] Sørensen, P. A., Kiil, S., Dam-Johansen, K. & Weinell, C. E. Anticorrosive coatings: a review. *J. Coat. Technol. Res.* **6**, 135-176 (2009).

- [21] Yebra, D. M., Kiil, S. & Dam-Johansen, K. Antifouling technology-past, present and future steps towards efficient and environmentally friendly antifouling coatings. *Progress in Organic Coatings*. **50**, 75-104 (2004).
- [22] Euvananont, C., Junin, C., Inpor, K., Limthongkul, P. & Thanachayanont, C. TiO<sub>2</sub> optical coating layers for self-cleaning applications. *Ceramics International*. **34**, 1067-1071 (2008).
- [23] Morris, G.E., Skinner, W.A., Self, P.G. & Smart, R.St.C. Surface chemistry and rheological behaviour of titania pigment suspensions. *Colloids and Surfaces A: Physicochemical and Engineering Aspects*. **155**, 27-41 (1999).
- [24] Psarras, G.C. Conduction processes in percolative epoxy resin silver particles composites. *Science of Advanced Materials*. **1**, 101-106 (2009).

## Chapter 2

### Three-dimensional Imaging Methods at Nano-scale

Currently, almost all three-dimensional (3D) imaging techniques are based on the concept “tomography”. Generally, tomography refers to any technique that cross-sectional imaging of an object from either transmission or reflection data collected by illuminating the object under a source [1]. Commonly, tomographic imaging deals with reconstructing a 3D image of an object from its two-dimensional (2D) projections acquired at many different directions [1, 2]. When X-rays are employed as the source for measurements and a computer is used as an assistant accessory, the method is called X-ray computed tomography (CT). With evolution of the computer into an essential controlling and analysing composite of the modern CT system and our lives, tomography is used as the substitute for computed tomography in many cases. Yet, some electron tomographic methods such as focused ion beam (FIB) tomography [3] and serial block-face scanning electron microscopy (SBFSEM) [4] generate cross-sections of 3D images directly, and no “reconstruction” needs to be applied.

Solution to the X-ray tomographic reconstruction problem must be dated back to 1917 when Johann Radon, an Australian mathematician, who proved that the original object can be reconstructed from its infinite projections from purely mathematical aspect [1]. However, the report of investigation results from the possible first practically manufactured CT scanner is from Allan M. Cormack [5]. The milestone of tomographic imaging is the installation of the

first clinical X-ray CT scanner, in 1971, which is invented by Godfrey N. Hounsfield who started the work from 1967 [6]. The 3D rendering of reconstructed images from CT was promulgated not long time later by William V. Glenn and his colleagues [2]. In the following years, the X-ray CT technique has been profoundly developed, although, the resolution of X-ray microscopy is still lower than the electron microscopy. This is mainly because of the limitation of fabricating high-performance X-ray optical elements, especially the X-ray lenses. Presently, 10-15 nm spatial resolution has been reached in two dimensions by soft X-ray transmission microscopy [7, 8], and 20-30 nm resolution has been achieved in two dimensional transmission imaging with hard X-ray source [9, 10]. For wider conception of X-ray imaging, sub-10 nm resolution has achieved in two dimensions [11]. The exciting 50-60 nm resolution has been obtained in both soft and hard X-ray 3D tomography [12, 13]. This region of sub-micron resolution X-ray tomography is also popularly called as X-ray nano-tomography.

As complementary technique, 3D electron tomography is also used in various areas. Among different approaches, TEM tomography [14, 15] has similar working principles as the conventional X-ray tomography, while FIB tomography and SBFSEM are, physically, serial-sectioning imaging. These 3D electron tomographic modalities usually give higher spatial resolution than X-ray means, especially on the imaging planes where they can reach the resolution the employed electron microscopes provided. However, in serial-sectioning cases, they are (mechanically) destructive.

## **2.1 Transmission X-ray Microscopy**

The early and most common tomographic measurements are carried out by transmission X-ray microscopes, which record the projections of target objects in forward transmission geometry (see figure 2.1). The primary contrast of the conventional transmission X-ray

microscopy (TXM) imaging is the absorption contrast which generated from the attenuation difference of X-rays through different parts of an object. In the modern TXM set-up, Zernike phase contrast can also be introduced [16].

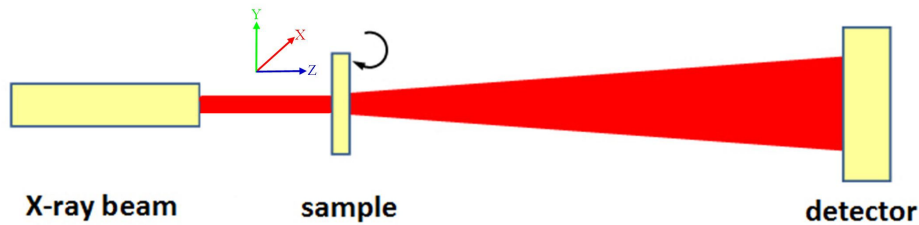


Figure 2. 1: Schematic working principle of X-ray microscope in forward transmission geometry.

### 2.1.1 Absorption Contrast in TXM

(This section is based on contents in references [1] and [17].)

The conventional X-ray tomography produces projections with absorption contrast. Since it is determined by the attenuation of X-rays through materials, the essence of the conventional X-ray tomography is obtaining a set of equations to solve the attenuation coefficient  $\mu$  of the object by scanning it from different directions, then transfer the  $\mu$  values of individual voxels into visible grey scale values in images.

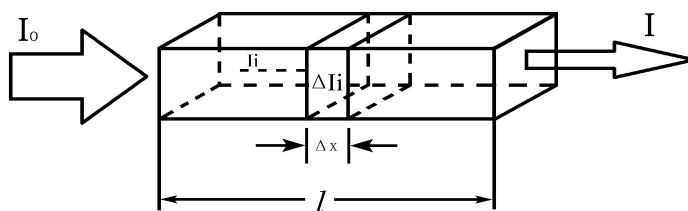


Figure 2. 2: An X-ray beam goes through a homogenous object. This figure is from a website.

When an X-ray beam goes through a homogenous object (see figure 2.2), its attenuation follows the Lambert-Beers Principle given by equation (2.1):

$$I = I_0 e^{-\mu l} \quad (2.1)$$

$I_0$  and  $I$  are intensities of the incident and transmitted X-ray beam, respectively;  $l$  is the thickness of the object, namely, the straight propagation distance of the X-ray beam in the object along the beam direction. The attenuation coefficient  $\mu$  is dominated by the absorption of X-rays in the object, and the influence of X-ray scattering to the  $\mu$  can be neglected in common cases. While, generally, an object is not a homogenous unit. We can assume that the inhomogeneous object consists of great number of voxels which are the minimum spatial volume unit. The size of the voxel is  $l_v \times l_v \times l_v$  and the attenuation coefficient of each voxel is  $\mu_1, \mu_2, \mu_3 \dots \mu_n$ , respectively (showing in figure 2.3). So, the intensity of the transmitted X-ray is expressed as equation (2.2):

$$I = I_0 e^{-(\mu_1 + \mu_2 + \mu_3 + \dots + \mu_n)l_v} \quad (2.2)$$

Then:

$$\mu_1 + \mu_2 + \mu_3 + \dots + \mu_n = -\frac{1}{l_v} \ln \frac{I}{I_0} \quad (2.3)$$

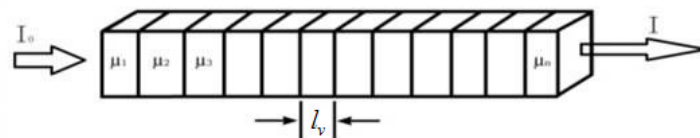


Figure 2. 3: An X-ray beam goes through an inhomogeneous object.  
This figure is from a website.

The tomographic scans from different directions provide enough data to establish a set of equations to solve all the attenuation coefficient  $\mu_1, \mu_2, \mu_3 \dots \mu_n$  of each voxel in the object. However, in order to generate qualified images, the scanning angular range and the number of projections collected need to be enough to sufficiently fill the Fourier domain during the 3D reconstruction. 180° scan, usually performed from -90° to 90°, satisfies the requirement to the scanning angular range. The number of projections should be roughly equal to the number

of rays (or sampling points) in each projection [1]. Generally speaking, the number of rays is the number of columns in the detector which are occupied by the projections of the measured object, see figure 2.4. This can be shown analytically by the following discussion:

In the Fourier/frequency domain presented in figure 2.5, each radial line, such as  $A_1A_2$ , is generated by one projection. If a  $180^\circ$  scan was carried out, the Fourier domain would be fully covered. If there are a number of  $M$  projections uniformly distributed over  $180^\circ$ , the angular interval  $\delta$  between successive radial lines is given by

$$\delta = \pi/M \quad (2.4)$$

Assume that the highest spatial frequency measured for each projection, namely, the radius of the disk shown in figure 2.5 is  $R$ . The distance between consecutive sampling points on the periphery of this disk is equal to  $A_2B_2$  and is given by

$$A_2B_2 = \delta R = \pi R/M \quad (2.5)$$

If there are a number  $N$  of rays in each projection, the total number of independent frequency domain sampling points on a line such as  $A_1A_2$  will also be the same. Therefore, the distance  $\epsilon$  between any two consecutive sampling points on each radial line in figure 2.5 will be

$$\epsilon = 2R/N \quad (2.6)$$

Because in the frequency domain the worst-case azimuthal resolution should be approximately the same as the radial resolution, we must have  $A_2B_2 = \epsilon$

Namely, 
$$\pi R/M = 2R/N \quad (2.7)$$

Equation (2.7) reduces to 
$$M = (\pi/2) \cdot N \quad (2.8)$$

So, in the experiment operations, the number of collected projections is usually roughly the same as the number of rays of the detector occupied by the largest projection of the object. Or, in lots of cases, 361 objects are collected during 180° scan with 0.5° interval.

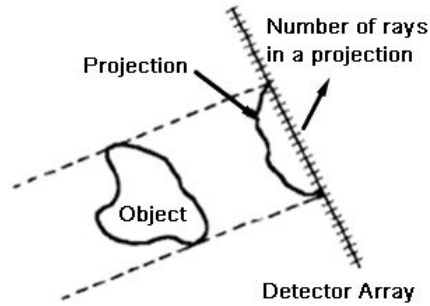


Figure 2. 4: A projection of an object to the detector. (From reference [1] by A. C. Kak et al.)

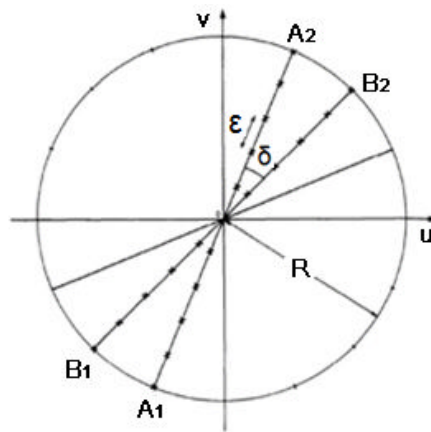


Figure 2. 5: Fourier/frequency domain parameters pertinent to parallel projection data. (From reference [1] by A. C. Kak et al.)

In conventional X-ray tomography, the intensity scale of reconstructed images is defined as CT value whose expression is

$$CT \text{ Value} = \frac{\mu_x - \mu_w}{\mu_w} \times 1000 \quad (2.9)$$

$\mu_w$  is the linear attenuation coefficient of water;  $\mu_x$  is the linear attenuation coefficient of the target part. The unit of the CT value is named Hounsfield Unit which is denoted by HU. Before the CT images become visible by eyes, the CT value is converted into grey scale. For instance, CT values is ranging between -1000 to 1000, accordingly, there are 2001 grey scale

values can be created, specifically, from purely dark (CT value -1000) to purely white (CT value 1000) [17].

### 2.1.2 Zernike Phase Contrast in TXM

The phase contrast method was discovered by Frits Zernike in the 1930s [18]. He introduced it into optical microscopy in 1942 [19] and was awarded the Nobel Prize of Physics in 1953 for his invention of the phase contrast microscope [20]. In the 1990s, Gerd Schneider and his colleagues brought Zernike phase contrast in X-ray microscopy [21, 22]. Since then, lots of work has been done to develop the system with phase contrast into a high resolution X-ray microscopy method [16, 23]. Currently, the NanoXCT, a type of commercialized full-field transmission X-ray microscope allying with Zernike phase contrast imaging mode has been launched into market by Xradia Inc. It can produce, as the manufacturer claimed, 3D images with 50 nm spatial resolution using both synchrotron- and laboratory-based hard X-rays.

Zernike phase contrast in the X-ray microscopy is generated by a phase ring, which is placed downstream of an X-ray lens, usually a (Fresnel) zone plate as shown in the following figure 2.6 [24].

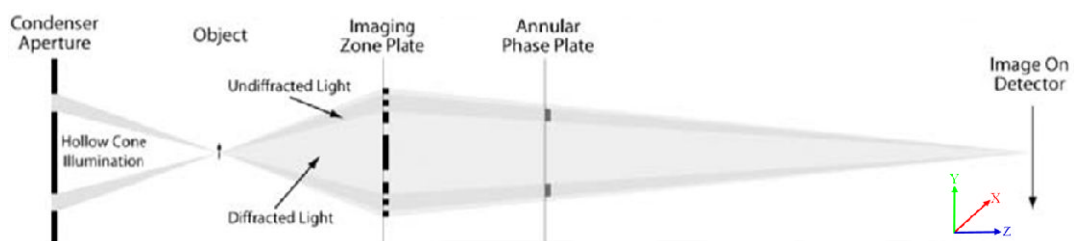


Figure 2. 6: Schematically optical layout of a transmission X-ray microscope allying with Zernike phase contrast. (From reference [24])

Figure 2.6 shows that a hollow core X-ray beam is illuminated on the sample, and then the transmitted X-rays are refocused by a (Fresnel) zone plate and go through an annular phase ring where the Zernike phase contrast is introduced in. Finally, an image with Zernike phase

contrast projects on a two-dimensional detector. The principle of the Zernike phase contrast is as follows:

After the hollow core x-ray beam went through the sample, diffracted light was generated besides directly transmitted (undiffracted) light. In the case of an absorption sample whose components have quite different X-ray attenuation coefficients, the phase shift between undiffracted light (abbreviates to U in following part) and diffracted light (abbreviates to D in following part) is  $\pi$ , then high absorption contrast was resulted as the sum light of U and D (abbreviates to S in following part) is rather smaller than the undiffracted light (shown in figure 2.7 (a)). However, for a phase sample whose components have similar X-ray attenuation coefficients, the outcome is different where the phase shift between undiffracted and diffracted light is in good approximation of  $\pi/2$  which results in the sum light in the image plane having almost the same amount as the undiffracted light thus showing very weak contrast for the sample structures (figure 2.7 (b)). In order to obtain the phase information of the sample, a phase ring is placed at the back focal plane of the objective (here is a Fresnel zone plate) that is matched in its geometry to the distribution of the undiffracted light. By this means, the undiffracted light can be phase shifted either by  $\pi/2$  (the case of figure 2.7 (c)) or  $3\pi/2$  (the case of figure 2.7 (d)) in respect to the diffracted light. The introduced phase shift,  $\pi/2$  or  $3\pi/2$ , is determined by the thickness of the phase ring along the X-ray beam propagation direction. In addition, the undiffracted light is reduced in its amplitude because of the absorption by the phase ring material, thus better matching the intensity level of the diffracted light. Consequently, U and D can be superimposed in the image plane as parallel or antiparallel vectors, in both cases the sum light have mature difference from the undiffracted light and high contrast can be generated [16, 22].

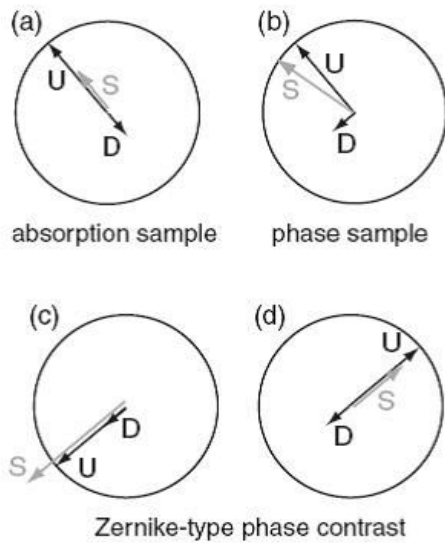


Figure 2. 7: Vector diagrams describing the amplitude and phase relations between undiffracted (U) and diffracted light (D) and their superimposition (S) as measured in the image plane. (a) and (b) show the situation for an absorption and a phase sample. (c) and (d) illustrated the phase shift of the wave vector of the undiffracted light, shown in (b), by  $\pi/2$  (c) or  $3\pi/2$  (d). (From reference [16] by G. Schneider et al.)

### 2.1.3 Transmission X-ray Microscopy (TXM) Instrumentation

As a powerful 3D imaging tool at nano-scale, the NanoXCT from Xradia, a commercialized full-field transmission X-ray microscope, was employed to investigate our specimens. The whole system of the NanoXCT consists of a pre-alignment optical microscope system (figure 2.8), a transmission X-ray microscope (figure 2.9) and a controlling computer.



Figure 2. 8: Pre-alignment optical microscope system of the NanoXCT from Xradia.

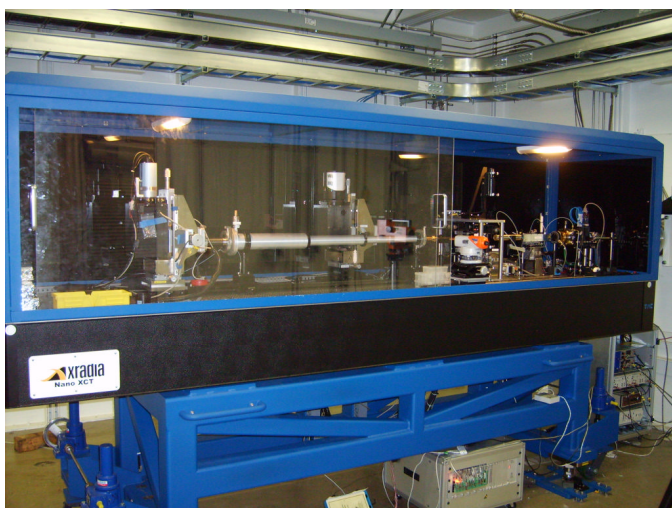


Figure 2. 9: Xradia's NanoXCT at the beamline 32-ID-C, Advanced Photon Source, Argonne National Laboratory, Argonne, IL, USA.

The pre-alignment microscope system is designed for aiding in locating the region of interest (RoI) of the specimen before the X-ray measurements. It is equipped with two objective lenses with 10 times and 50 times magnification, respectively, and two illuminators to provide both transmission and reflection illumination. More importantly, it has the identical sample stage with the same coordinate system as the one installed in the transmission X-ray microscope. From the pre-alignment microscope, a set of rough x, y and z coordinates of the RoI can be obtained quickly and much faster than using the X-ray microscope. These coordinates are then input into the controlling computer and help to locate the accurate RoI in the transmission X-ray microscope.

The schematically optical layout of the transmission X-ray microscope is presented in figure 2.6. The incident X-ray beam is focused by a condenser which works together with a center beam stop and a pinhole to produce a hollow cone beam to illuminate onto the sample. X-rays through the sample are then magnified by a (Fresnel) zone plate. Finally, the projections of the sample are formed on a charge-coupled device (CCD) detector. If necessary, the phase ring can be placed downstream of the zone plate to generate Zernike phase contrast to help visualizing, usually, low X-ray absorption structures of the sample.

The condenser is a tapered capillary, which focuses X-rays by fully internal-reflection (total external reflection from the inner surface). The focusing efficiency of the capillary condenser is about 90% which is significantly higher than the common zone plate condensers whose focusing efficiency is typically around 10-20% [25]. The phase ring used in the NanoXCT is usually a gold annular ring whose thickness along the X-ray propagation direction determines the phase shift introduced to the undiffracted X-rays [16].

The Xradia's NanoXCT is designed for working at both absorption contrast and Zernike phase contrast modes. Obviously, the absorption contrast mode is suitable for measuring absorption objects and the Zernike phase contrast mode is designed for investigating phase objects. The phase ring is removed from the X-ray beam propagation path when the absorption contrast mode is used, and it is inserted between zone plate and detector when the Zernike phase contrast mode is employed. However, whenever a sample can provide sufficient absorption contrast, the phase ring had better be removed from the imaging system. As an optional set-up for the NanoXCT, two different resolution optics settings are also available: "150 nm resolution" and "50 nm resolution". The two resolution mode switch is achieved by using different zone plates. As the achievable spatial resolution  $\delta$  of the microscope is defined by the objective zone plate according to  $\delta = 1.22\Delta r / m$ , in which  $\Delta r$  is the width of the outmost ring of the zone plate used and  $m = 1, 3, 5, \dots$  is the diffraction order [25]. Employment of the thinner outmost ring zone plate would produce higher spatial resolution. Another way to improve the spatial resolution of the microscope is using higher order diffraction X-rays which have much lower intensity. The NanoXCTs we used with 1024×1024 pixel CCD detectors, under the "150 nm resolution" mode, the field of view (FoV) of the microscope is 66×66  $\mu\text{m}^2$ , the pixel size of generated images is 65×65  $\text{nm}^2$ , the depth of focus is 60  $\mu\text{m}$  and the effective reconstruction volume is 60×60×60  $\mu\text{m}^3$ . For the "50 nm resolution" mode, these parameters are 20×20  $\mu\text{m}^2$ , 21×21  $\text{nm}^2$ , 20  $\mu\text{m}$  and 15×15×15  $\mu\text{m}^3$ .

respectively. The matches of different contrast and resolution modes are commonly determined by sample characters and research requirements. However, the Zernike phase contrast mode is not recommended when doing 3D measurements for quantitative analysis since the tomographic reconstruction algorithm used by the NanoXCT is designed for calculating the pure absorption contrast projections, and the phase contrast (mode) is more sensitive to the beam stability which increases the background fluctuation seriously.

In order to obtain high-quality images from the NanoXCT, the target sample should have an easily and obviously distinguishable reference point/marker during the measurements for aligning the sample position. This reference will also be used for 3D image reconstruction. The point/marker can be a separately high (absorption) contrast spot in the RoI of the sample (see RPC3 in figure 2.10a, it is an artificial spot added in the real projection image obtained from the NanoXCT) or a sharp tiny tip of the sample RoI (see RPC2 in figures 2.10a and b), and the combination of two would be the best candidate (see RPC1 in figure 2.10a). The reference points such as RPC1 in figure 2.10a can be obtained by manually depositing/transferring micro-particles of high X-ray absorption capabilities, usually gold particles sized around 500 nm to 1  $\mu\text{m}$ , to the tips of the sample RoIs from sharp pins fully covered by (gold) micro-particles. The depositing/transferring is done by using the high-accuracy movable stage in the pre-alignment optical system (see figure 2.11). During the whole measurement, the sample RoIs should be staying in the FoV of the microscope all the time. To help reaching this in practice, the reference points, which are usually the high contrast spots at the tips of the sample RoIs such as the RPC1 in figure 2.10a, should be kept in the upper-center of the effective illumination region (EIR) of the microscope (see figure 2.10). If possible, the reference points had better be moved to the position (in the sample holder) where the x and z coordinate values are around zero in the pre-alignment optical system. In the coordinate system, the z axis is along the X-ray beam propagation direction, the y axis is perpendicular

to the z axis and vertical to the horizontal plane and the x axis is perpendicular to the z direction and parallel to horizontal plane (see figure 2.6).

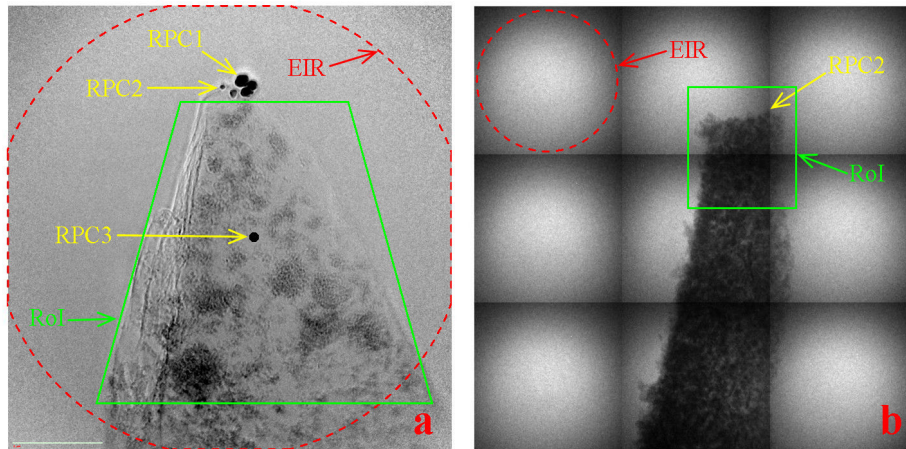


Figure 2. 10: RoIs (region of interest) and reference point candidates (RPC) of samples for measurements by the NanoXCT. a. A projection image of a coating sample measured by the NanoXCT using X-rays of a photon energy of 8.0 keV at the beamline 32ID-C, Advanced Photon Source, Argonne National Laboratory, Argonne, IL, USA. b. A 3×3 mosaic image of a silver epoxy adhesive sample measured by the NanoXCT using laboratory-based X-rays of a photon energy of 8.1 keV at the Henry Moseley x-ray imaging facility at the University of Manchester, the UK.

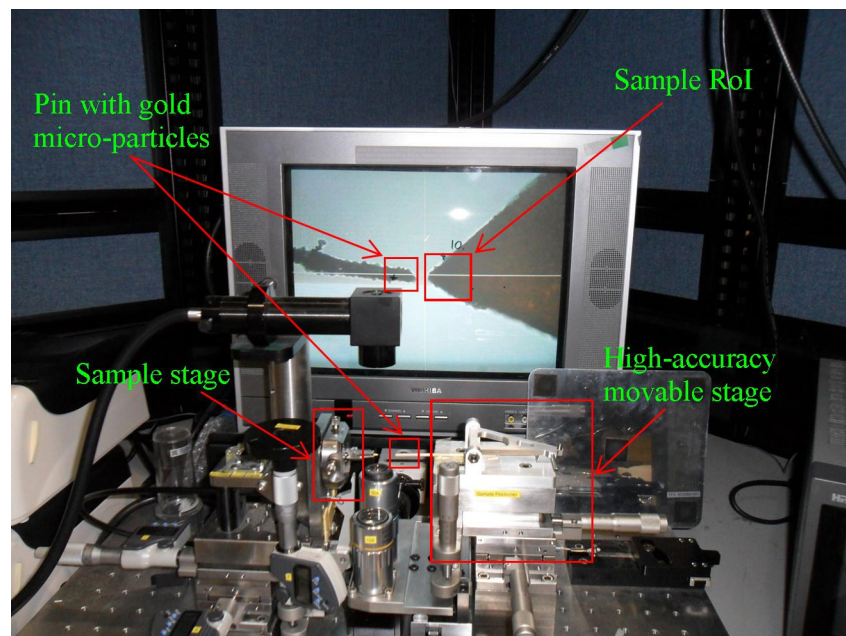


Figure 2. 11: Photographic diagram showing the gold micro-particle transfer. The gold micro-particles at the sharp pin are transferring to the tip of the sample RoI using the high-accuracy movable stage in the pre-alignment optical system.

The general steps of acquiring tomographic data and performing 3D image reconstruction using the NanoXCT system are presenting as following:

1. Locate the sample RoI in the NanoXCT:

After loading the sample in the sample stage of the X-ray microscope, input the x, y and z coordinates obtained from the pre-alignment optical system into the controlling computer. Acquire a projection, if the obtained image does not show the sample RoI captured by the pre-alignment microscope, perform a mosaic scan. It is an imaging mode that allows collection of multiple single FoV projection images at extended regions which are larger than the FoV of the microscope and then automatically stitches the acquired individual projections together to get a single image. Figure 2.10b is a 3×3 mosaic image of a silver epoxy adhesive specimen. Usually, a 5×5 mosaic image which sizes 5 times of the FoV in both x and y directions is big enough for locating the sample RoI. Once, the RoI is presenting in the image, read out its coordinates and then drive the sample stage to the location to make the RoI occupy the centre of the FoV.

2. Sample rotation axis alignment (by external telescope):

In case the X-ray microscope has an external telescope (see figure 2.12), which can be used to monitor the sample stage, a sample rotation axis alignment should be done to make the sample rotation axis as close as possible to the rotation axis of the sample stage of the instrument. This will greatly help to keep the sample RoIs in the FoV of the X-ray microscope. The alignment can be done following the steps below:

- a. Drive the sample to 0° in the instrument. Move the centre of the reference cross (with scale) of the telescope to the reference point of the sample. Assume the current sample position in the telescope as “sam1”. Rotate the sample to 180°, record the new sample position “sam2”. Then move the sample reference point to the position  $\text{sam3} = (\text{sam1} + \text{sam2})/2$  in the telescope.

- b. Move the centre of the reference cross of the telescope to the position sam3. Drive the sample to  $-90^\circ$  in the instrument, record the new sample position “sam4”. Move the sample reference point to the position  $\text{sam5} = (\text{sam3} + \text{sam4})/2$  in the telescope.
- c. Move the centre of the reference cross of the telescope to the position sam5. Drive the sample to  $90^\circ$  in the instrument, record the new sample position “sam6”. Move the sample reference point to the position  $\text{sam7} = (\text{sam5} + \text{sam6})/2$  in the telescope.
- d. Rotate the sample from  $0^\circ$  to  $180^\circ$  in the instrument to check whether the sample reference point always stay at the same place during the whole rotation. If yes, the alignment was finished and the sample has almost the same rotation axis as the sample stage of the instrument. If not, repeat the steps a-c again until the alignment finished.

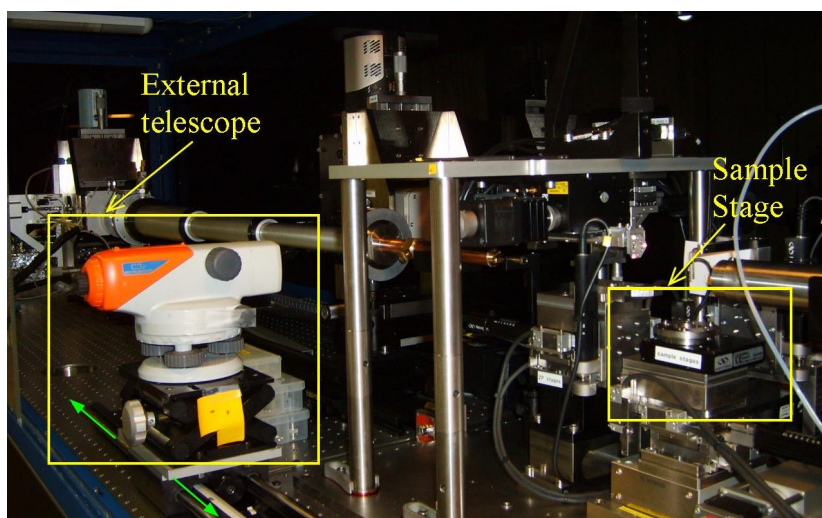


Figure 2. 12: The external telescope of the Xradia's NanoXCT at the 32-ID-C, Advanced Photon Source, Argonne National Laboratory, Argonne, IL, USA.

### 3. Get the focus plane of the sample:

Keep the RoI at the centre of the FoV, use the focal series mode of the X-ray microscope to acquire a series of images at different z positions. Select an image with the best focus from this series; drive the sample to the z position of this image. The xy plane at this z

coordinate is the focus plane of the sample, where the microscope can obtain the best quality of images from the sample.

4. Pre-tomography scans with the software stage correction:

Before the final tomographic scan, which is performed to acquire tomographic projections for 3D reconstruction, a series of pre-tomography scans need to be carried out. After each pre-tomography scan, a stage calibration is executed to guarantee that the ROI will stay in the FoV during the whole final scan. The series of pre-tomography scans are performed by doing several tomographic scans with wide step like  $5^\circ$ , and with gradually-increasing scanning angle ranges such as from  $-20^\circ$  to  $20^\circ$  first, and then from  $-40^\circ$  to  $40^\circ$ , thirdly, from  $-60^\circ$  to  $60^\circ$  and finally reach to the angle range of the final tomographic scan.

5. Collect reference projection images:

The reference projections have to be collected and had better be acquired both before and after the final tomographic scan, especially for the long time final scans. The reference projections are required to be collected without samples and the data acquisition parameter setting needs to be, usually, the same as the final scan. In some exceptional cases such as the final tomographic scan data were collected discretely, the reference projection acquisition setting needs to match the final scan. After the reference projections are collected, average them and generate a single image to work as the background of the final tomographic scan data.

6. Collect the final tomographic data:

The final tomographic scan is performed the same as pre-tomography scans, but with much finer angular step in a large scanning angular range, usually, from  $-90^\circ$  to  $90^\circ$ . There are two main considerations for the final tomographic scan: scanning angular range and the number of projections collected. Both of them need to be enough to sufficiently fill

the Fourier domain during the reconstruction from 2D projections to 3D images. 180° scan (from -90° to 90°) can satisfy the requirement for the scanning angular range. The number of projections should be roughly equal to the number of rays of the detector occupied by the largest projection of the object (see section 2.1.1) [1]. In practice, 721 projections, even 361 projections obtained from scans between -90° and 90°, with 0.25° or 0.5° internal, are normally enough to secure a qualified 3D tomographic reconstruction.

Once the final tomographic scan was done, the background needs to be subtracted from acquired projections using the reference image obtained in the above step 5. Then, align the background-subtracted 2D projections and input them into the affiliated tomographic reconstruction software with the NanoXCT to generate 3D images.

## **2.2 Ptychographic X-ray Computed Tomography**

Ptychographic X-ray computed tomography (PXCT) [26, 27] is a newly developed phase-sensitive imaging method which currently offers a spatial resolution of 100 nm in 3D [28]. It combined ptychographic X-ray imaging (also called scanning coherent X-ray diffractive imaging) [29, 30] with conventional computed tomography [1, 2]. As with conventional X-ray tomography, PXCT collects many projections of the samples from different directions, and then reconstruct these 2D projections into 3D images. However, the PXCT projections at individual orientations are reconstructed from multiple coherent X-ray diffraction patterns by X-ray ptychographic algorithms, not directly recorded by a detector. The 3D tomographic reconstructions of PXCT are performed by using a revised filtered back-projection algorithm developed for phase contrast images [27, 31].

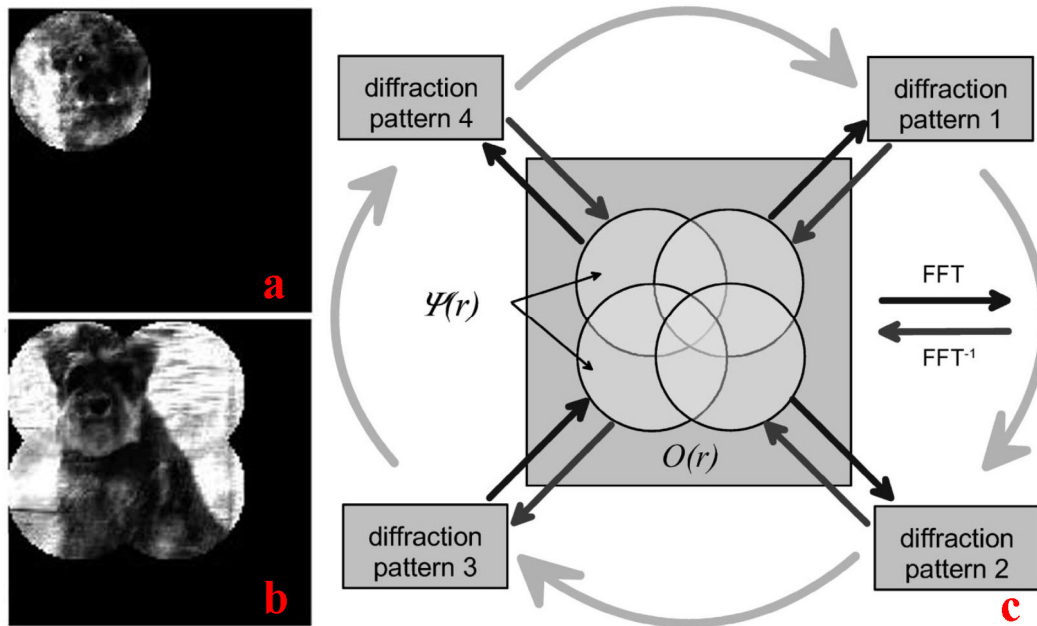


Figure 2. 13: Schematic of working principle of ptychographic imaging. a, A single illumination position. b, Multiple illumination positions with overlapped regions. There are 4 illumination positions displayed here. c, Diagram of the ptychographic phase-retrieval algorithm. The outer circular arrows indicate the position stepping within one iteration. The arrows within indicate (inverse) Fourier transforms and the desired input-output information. Panels a and b are from reference [42], panel c is from reference [29].

X-ray ptychography [29, 32, 33] is a variation of the method of conventional X-ray coherent diffractive imaging (XCDI) [34-37]. It circumvents the isolated sample requirement of the conventional XCDI and provides larger field of view. Actually, ptychographic imaging has been intensively developed in last a few years to investigate various targets using wider range coherent electromagnetic radiations, not X-rays only, which including such as visible light [38, 39] and electron beams [40, 41]. The X-ray ptychography is an approach to solve the X-ray refractive index,  $n=1-\delta+i\beta$ , of the target objects. It generates images of a specimen by phase-retrieving a number of its (Fraunhofer, ie far-field) X-ray diffraction patterns using iterative algorithms [42-45] (see figure 2.13). The diffraction patterns used for ptychographic phase retrieval are acquired at different positions of the sample with sufficient overlapping regions (see figure 2.13a and b), 60%-80% recommended [46], by scanning the sample itself. Currently, there are two robust and reliable ptychographic phase retrieval algorithms in wide

use: difference map algorithm [30, 45] from Franz Pfeiffer's group in Munich, Germany and ePIE (extended ptychographical iterative engine) [44] from John Rodenburg's group in Sheffield, UK.

Figure 2.14a displays on-site real experiment set-up of PXCT at the cSAXS beamline of the Swiss Light Source, Paul Scherrer Institut, and figure 2.14b is its schematic diagram. Of the PXCT measurements, X-rays of a single photon energy were selected by a (double-crystal Si(111)) monochromator. A pinhole, usually a few microns in diameter, inserted upstream of the sample, and as close as possible to the sample, along the X-ray propagation direction, was used to define the coherent region of the incident x-ray beam. Other X-ray optical elements such as Fresnel zone plate or Kirkpatrick-Baez (KB) mirrors can also be used for this purpose. The sample size should be smaller than the scanning range of the sample stage which is ideally the same as the achievable FoV of PXCT. At the cSAXS beamline, the currently achievable FoV is  $80 \times 80 \mu\text{m}^2$  which is determined by the high accuracy piezoelectric translation stage that connects with the sample stage and controls the XY plane movement. In order to get a specimen of good size and shape, an FIB (Focused Ion Beam) tool is suggested to be used to fabricate the samples into cylinder shape if possible. X-ray diffraction patterns in the transmission geometry (ie through the samples) were recorded by a two-dimensional detector after the patterns travelled through a 7 meter long flying tube to ensure Fraunhofer diffraction conditions. At this beamline, a PILATUS [47] photon-counting detector (pixel size  $172 \mu\text{m} \times 172 \mu\text{m}$ ) is provided for use. The same as conventional tomography, during the measurements, the sample was rotated, usually 180 degrees with 0.5 degree intervals, and many projections of the sample were collected at different directions. At each orientation angle, the sample was scanned to a number of different positions, usually following a circular radial pattern scan [48], in a plane perpendicular to the X-ray beam propagation direction to produce a field of view that can well cover the whole representative region of the sample.

Each projection was reconstructed from all diffraction patterns acquired at that orientation (by a difference map ptychographic algorithm [30]). The 3D structure images of the samples are then generated by applying the filtered back-projection tomographic reconstruction [27, 31] to the obtained phase projections.

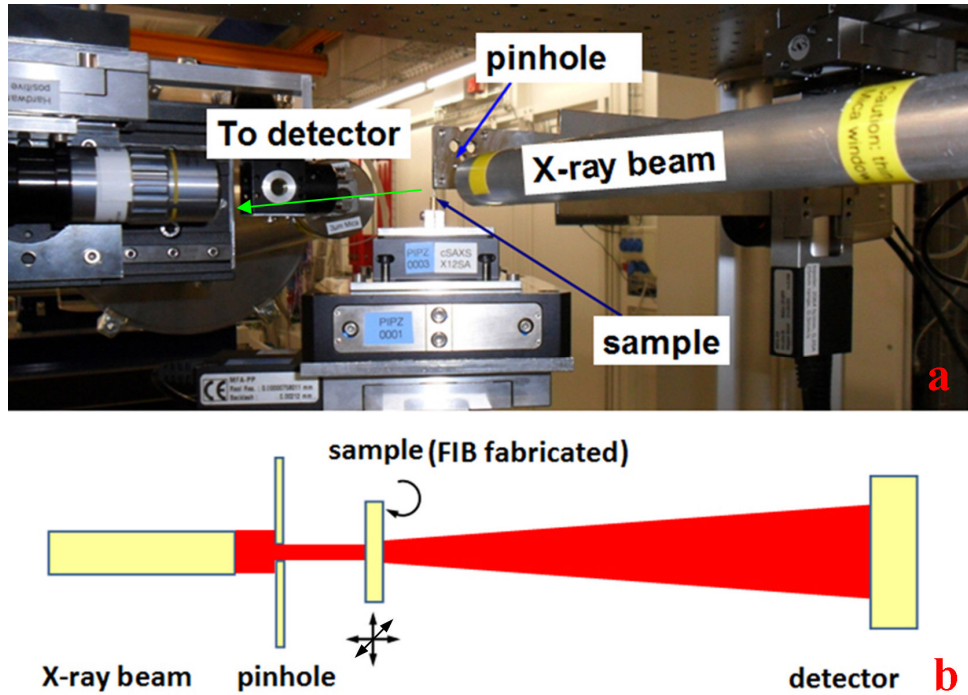


Figure 2. 14: Experimental set-up of ptychographic X-ray computed tomography. a, Real on-site set-up at the cSAXS beamline at the Swiss Light Source. X-rays travel from right to left in the photograph. b, Schematic of the experimental set-up, X-rays travel from left to right in the diagram.

Generated 3D images from the PXCT measurements provide quantitative information since they are actually 3D mapping of distribution of the real part,  $\delta$ , of the X-ray refractive index of the measured samples. Since the real part  $\delta$  of the X-ray refractive index within the object is proportional to the phase shift of the incident wave-field travelling through it (due to the modification of the object on the wave-field during its propagation). It can be expressed as

$$\delta = -\frac{\lambda}{2\pi} \cdot \frac{\phi_{\Delta r}}{\Delta r} \quad (2.10)$$

where  $\phi_{\Delta r}$  is the (reconstructed) phase shift value of the wave-field as it passed through a

voxel of side length  $\Delta r$  (along the beam propagation direction) of the object,  $\lambda$  is the wavelength of the illumination X-ray source. The tomographic reconstruction from many projections taken at different orientations of the sample with respect to the incident beam leads to the solution of the 3D distribution of the real part  $\delta$  of the refractive index. Away from the X-ray absorption edges, the electron density  $n_e$  distribution can be obtained by

$$n_e = \frac{2\pi\delta}{\lambda^2 r_e} \quad (2.11)$$

where  $r_e$  denotes the classical electron radius which equals  $2.81794 \times 10^{-15}$  m. Therefore, PXCT provides directly the 3D electron density distribution of the specimen. The relation between electron density and mass density  $\rho$  depends on the atomic species

$$\rho = \frac{n_e A}{N_A Z} \quad (2.12)$$

where  $A$  is the molar mass,  $Z$  is the total number of electrons in a molecule and  $N_A$  is Avogadro's number which equals  $6.02214 \times 10^{23}$  mol<sup>-1</sup>. With the knowledge of the chemical composition of the target part, PXCT allows an accurate measurement of the mass density distribution of the object to single voxel level. (This paragraph starts from “Generated 3D images from the PXCT ...” is based on contents from references [26] and [28].)

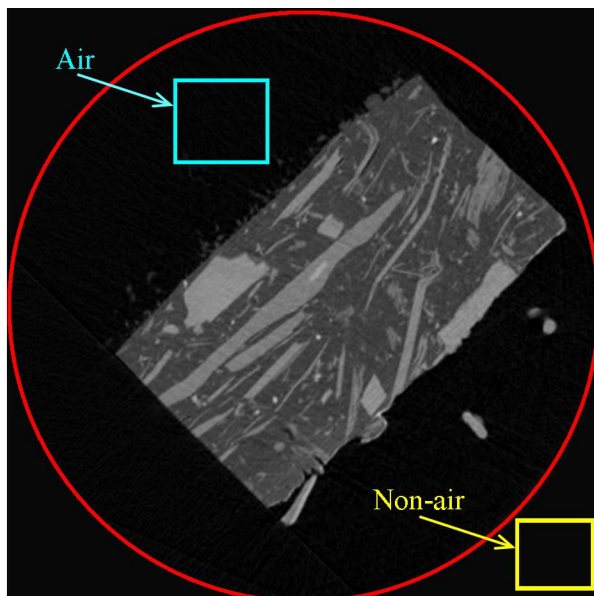


Figure 2. 15: A single tomogram slice of the aluminium epoxy barrier marine coating perpendicular to the rotation axis of the reconstructed 3D volume from PXCT. The area in the blue rectangle is a part of the region of reconstructed air surrounding the sample. The area inside of the red circle is the effective reconstruction tomogram region. The outside is the random contribution from the reconstruction algorithm, a fraction of it was labelled by a yellow rectangle.

Since the filtered back-projection tomographic reconstruction introduces a small offset  $\Delta\delta$  to the computed  $\delta$ , in order to get high-accuracy quantitative information,  $\Delta\delta$  should be removed. This offset can be determined through the average value of  $\delta$  of a region of air as labeled in figure 2.15. Then the offset can be removed by subtracting  $\Delta\delta$  from  $\delta$  of the reconstructed 3D image. The offset removed  $\delta$  values should be then used for the remaining calculations. The region outside the red circle in figure 2.15 should not be used for any scientific purpose such as offset or noise estimating because it is coming from the random contribution of filtered back-projection tomographic reconstruction algorithm and do not have correct statistics. In case the (files of)  $\delta$  values are not available directly, but only grayscale images, there is a linear relationship between the grayscale values and the  $\delta$  values which can be determined quickly once you got the image file exporting settings such as the range of  $\delta$  values in the original files.

### **2.3 X-ray Holo-tomography (Based on Free Space Propagation Phase Contrast)**

X-ray holo-tomography [49, 50] is another 3D X-ray imaging method providing phase contrast. This means the real part  $\delta$  of the X-ray refractive index of the target specimens would be solved after successful measurements, and according functions (2.11) and (2.12), the specific electron density and mass density of a region in the specimens can be obtained as well [49]. X-ray holo-tomography is a free space propagation phase contrast, or Fresnel diffraction contrast [51], based X-ray imaging approach which has been studied from the 1990s both experimentally and theoretically [51-55]. After over a decade development of the method itself, and with the progresses made in the X-ray sources and X-ray optical focusing elements, X-ray holo-tomography and its variants have possessed the capabilities to produce 3D images with sub-micron spatial resolution [56, 57].

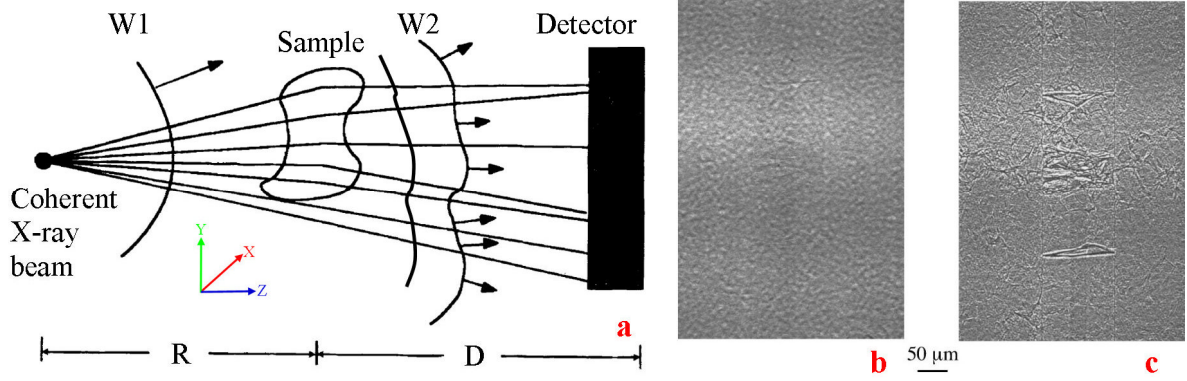


Figure 2. 16: Free space propagation phase contrast based X-ray imaging. a, Schematic illustration of configuration for the imaging method. b & c, Projection images of a monofilament Al/SiC composite after monotonic room temperature tensile testing. The images were obtained at an x-ray energy of 25 keV ( $\lambda = 0.5 \text{ \AA}$ ), at a sample-detector distance  $D$  of (b) 0.005 m and (c) 0.13 m. Panel (a) was adapted from figure 1e in reference [54]; (b) and (c) were from reference [55].

The propagation based X-ray imaging is, in many senses, probably the simplest technique of phase contrast X-ray imaging because there is no requirement of X-ray optical element in the experimental set-up [49, 51] and the constraint on spectral width is released as well [54, 58]. The basic mechanism of free space propagation phase contrast can be graphically illustrated in figure 2.16a. After a coherent X-ray beam passing through a phase object, the variations of X-ray refractive index and thickness of the object lead to a shape change of the X-ray wave-front as the variations provide different optical path lengths to the X-rays in the object [54]. Hence, a phase shift/difference is produced and a phase gradient is introduced which is transverse to mean X-ray propagation direction  $z$  (see figure 1.16a and reference [54]). The induced phase shift  $\phi_{(x,y)}$  of the wave-front, relative to X-rays propagated in vacuum, at the position after it exits the sample (in a plane perpendicular to the mean X-ray propagation direction  $z$ ) is

$$\phi_{(x,y)} = -\frac{2\pi}{\lambda} \int \delta d_z \quad (2.13)$$

Upon propagation of X-rays in free space, the phase shift increases, which causes the phase shift to be transformed into an amplitude/intensity difference. Therefore, (phase) contrast can

be generated by propagating a distance  $D$ ; and when  $D \approx 0$ , there is no phase contrast recorded by the detector (see figures 2.16b and c). During experiments, locations of the detector are chosen to make its spatial resolution sufficient enough to resolve the induced intensity differences arising from the wave-front distortions during propagation [54]. For a phase object, the Fourier transform of the intensity distribution at distance  $D$  is [49, 51]

$$\tilde{I}(f) = \delta(f) + 2 \sin(\pi\lambda Df^2) \tilde{\phi}(f) \quad (2.14)$$

if 
$$|\phi(x) - \phi(x - \lambda Df)| \ll 1 \quad (2.15).$$

Here  $\tilde{I}(f)$  and  $\tilde{\phi}(f)$  are the Fourier transform of the intensity distribution  $I(x)$  and the phase shift  $\phi(x)$ , respectively, for the spatial frequency  $f$  of the illumination, the  $\tilde{I}(f)$  and  $\tilde{\phi}(f)$  are thus linearly related at the sample-detector distance  $D$  [49, 51].  $\delta(f)$  is the Dirac distribution and it corresponds to a homogeneous background in the images [51]. When coherent X-ray sources used, the distance  $D$  falls into the Fresnel diffraction field which is a distance of the order of 1 m [51].

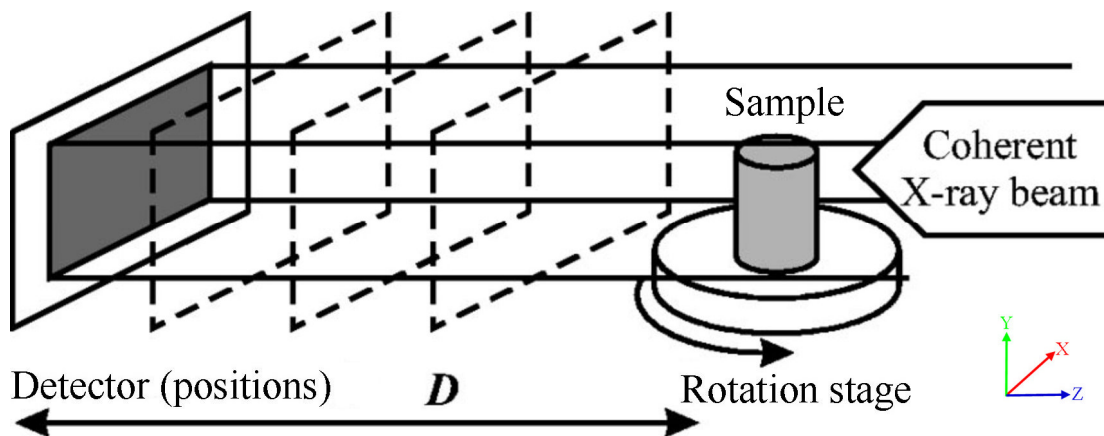


Figure 2. 17: Schematic diagram of the X-ray holo-tomography experimental setup. Images recorded at different distances from the sample are combined to retrieve numerically the phase of the wave exiting the sample. This is repeated for a large number of angular positions of the specimen. This figure was adapted from figure 1 in reference [49].

For X-ray holo-tomography, again, a series of projections of the specimen from a number of different angular orientations are obtained, and then reconstructed into 3D images by using the filtered back-projection algorithm [50]. However, in order to acquire unambiguously reliable (phase) projections of X-ray holo-tomography at individual orientations, multiple images at each orientation angle were recorded at different sample-detector distances  $D$  (see figure 2.17) within the Fresnel diffraction field, and then phase retrieved into a single projection image using a method originally developed for electron microscopy [59]. In practice, usually images at 4 different sample-detector distances are recorded for the phase retrieval [49], and the key requirement of the method is an illumination sources with high spatial coherence degree to enable the detectors to resolve the phase variations of the exit wave-front through the sample.

Another 3D imaging method similar to X-ray holo-tomography is holographic computed X-ray laminography (HCXL) [60-63]. Different from X-ray holo-tomography, during the HCXL measurements, the (flat) specimens are rotating around their shortest geometrical axes which are the surface normal directions of the objects (see figure 2.18), not rotating along the axes perpendicular to the X-ray beam propagation direction as in the standard tomographic measurements. The data acquisition, phase retrieval and tomographic reconstruction of HCXL are the same as X-ray holo-tomography. HCXL is designed for measuring laterally extended flat objects which normally bring about artefacts to the images obtained by standard tomography [60]. Since most cured dry coating samples are a few tens to hundreds microns thick films. In many cases, they can be assumed as flat objects, this method could be a suitable way for 3D coating structure investigation.

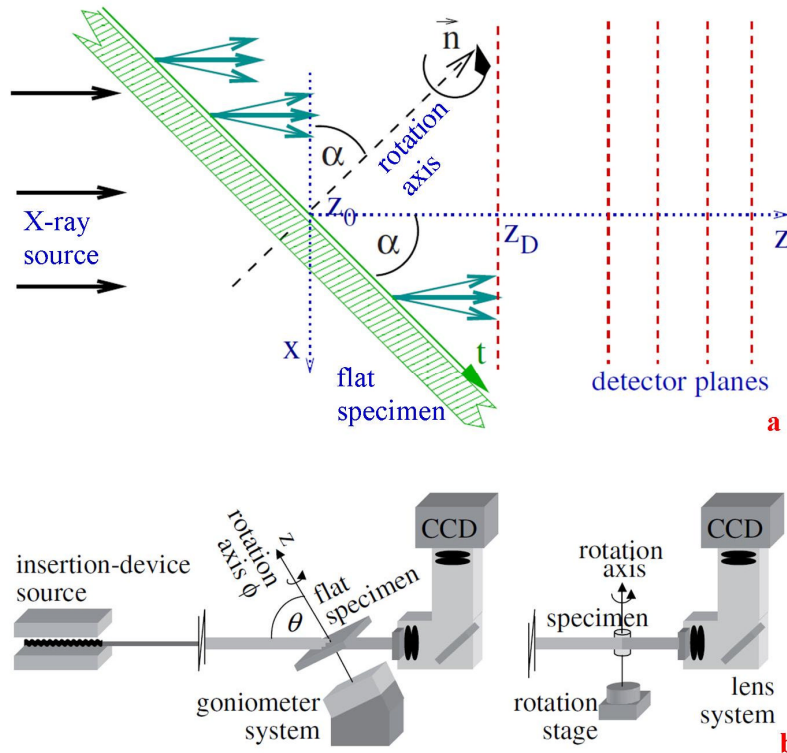


Figure 2. 18: Schematics of the holographic computed X-ray laminography (HCXL) experimental setup. a, Sketch of HCXL set-up. b, Comparison of the experimental set-ups for HCXL (left) and for standard tomography (right). Panel a is from reference [60], and panel b is from reference [62].

## 2.4 Other X-ray Imaging Techniques

There are some other approaches available for (materials) structure study by X-rays such as wave-front modulation coherent X-ray diffraction imaging [64-66], analyzer crystal [67, 68] or interferometer [69-71] based phase contrast X-ray imaging. Although these methods either did not evolve into 3D imaging solutions or did not reach to the level of 100 nm spatial resolution, they are under development and have the potential to be effective ways to investigate the coating structures.

## 2.5 Serial Block-Face Scanning Electron Microscopy (SBFSEM)

Serial block-face scanning electron microscopy (SBFSEM) is a 3D electron imaging method based on serial sectioning [72-74], which was recently developed from ultrathin section sample preparation for transmission electron microscopy (TEM) [75, 76]. It was originally

designed for 3D structure investigation of biological specimens [72, 77-79]. SBFSEM acquires continuous successively parallel images of fresh surfaces of the samples created by iteratively mechanical cuts made by a diamond knife installed in an ultramicrotome in the scanning electron microscope chamber [72] (see figure 2.19). 3D images of the samples are then generated by stacking corresponding series of images together. Different from X-ray tomographic methods mentioned above, SBFSEM is a destructive 3D imaging method since the samples are destroyed by the diamond knife cutting during measurements. The spatial resolution provided by SBFSEM can reach the electron microscopy resolution in the imaging planes (xy planes, see figure 2.19b) which depends on the electron microscope used. Along the cutting direction (z direction, see figure 2.19b), the achievable resolution is at the level of a few tens of nanometers which determined by the slice thickness of the cutting. Currently, 20 to 30nm thick slices can be reliably obtained by the diamond knife cutting. Several nanometer depth cutting is feasible, although it is really challenging.

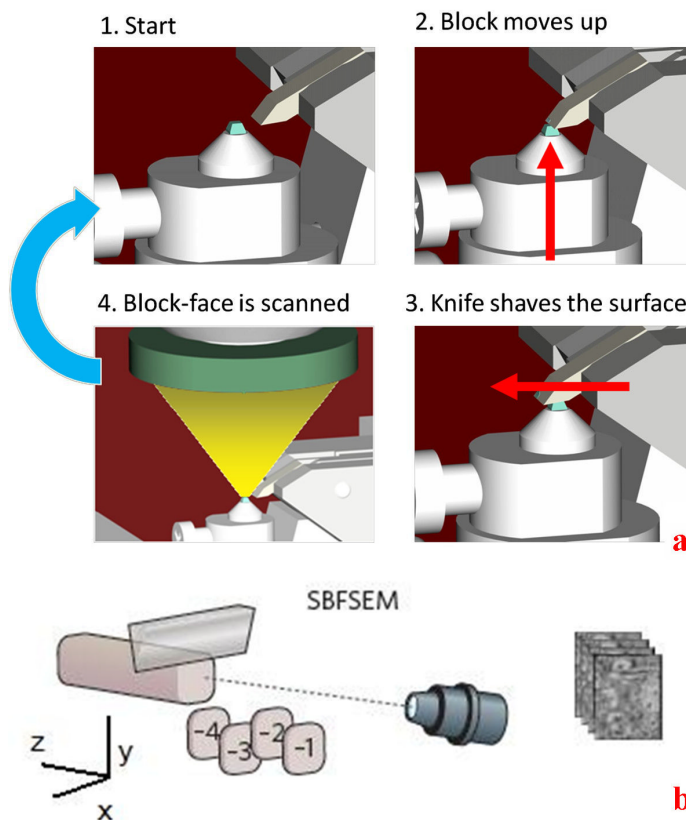


Figure 2. 19: Schematic presentation of working process of SBFSEM. a, Diagram of a simplified sequence of cutting and imaging operation of SBFSEM. b, A schematic of working principle of SBFSEM. Panel a was adapted from materials provided by Gatan Inc., and panel b is from reference [74].

Based on the work performed by Winfried Denk and Heinz Horstmann at the Max-Planck Institute, Heidelberg [72], the SBFSEM system has been manufactured and marketed as a commercial scanning electron microscopy (SEM) accessory unit by Gatan Inc., and it was named as 3View<sup>®</sup>. The 3View<sup>®</sup> unit can be assembled into, usually, a field emission gun environmental scanning electron microscope from manufacturers such as FEI or Carl Zeiss. Commercialized products of the combination of 3View<sup>®</sup> and SEM, for instance, SIGMA<sup>™</sup> 3View<sup>®</sup> and MERLIN<sup>®</sup> 3View<sup>®</sup> from Carl Zeiss, are already available in the market.

Before the repeated cutting and imaging procedure starts, the samples have to be fixed. The fixations are usually done by embedding the samples into epoxy resin blocks, and a typical recipe of the resin recommended by Gatan Inc. is shown in table 2.1 (from Agar Scientific Ltd., UK). The hard resin blocks presented in the table are preferred for diamond knife cutting. They are prepared by mixing and shaking the required amounts (by volume) of pre-warmed (at 60°C) resin and hardeners (DDSA and MNA) for a few minutes, and then adding the accurate amount of accelerator BDMA (2.5-3% by volume) to the mixture of epoxy resin and hardeners with a continue shaking for another minute or two. Here, DDSA is Dodecenyl Succinic Anhydride, MNA is Methyl Nadic Anhydride and BDMA is Benzyldimethylamine. The samples are then embedded in the fresh liquid four component resin mixture and left to harden overnight at 60°C. Longer times of 24 to 48 hours curing may improve the sectioning properties of the cured resin blocks. The curing temperature for the mixture should not be higher than 60°C. In case the samples are solid and strong enough such as cured (aluminium) epoxy coating films, they can be fixed by being glued on aluminium specimen pins (Gatan, Pleasanton, CA) directly using cyanoacrylate glue. After the fixations, the specimens themselves or specimens embedded resin blocks are then trimmed down by a microtome to create block faces size around 500 µm × 500 µm since the moving range of the diamond knife

of the 3View<sup>®</sup> unit is 1.2 mm. Once the block faces were obtained, they are ready for the SBFSEM measurements.

Table 2. 1: A typical recipe of the embedding resin giving soft, medium and hard resin blocks.

Hardness Chemicals	Soft	Medium	Hard
Agar 100 epoxy resin	20ml (24g)	20ml (24g)	20ml (24g)
Hardener, DDSA	22ml (22g)	16ml (16g)	9ml(9g)
Hardener, MNA	5ml ( 6g)	8ml ( 10g)	12ml ( 15g)
Accelerator, BDMA	1.4ml (1.5g)	1.3ml (1.5g)	1.2ml (1.4g)

Once the microtome trimmed samples are were-mounted, the cutting and imaging work can be automatically performed by the 3View<sup>®</sup> unit following the input measurement parameters such as cutting speed and depth. This turns the conventional labour intensive serial sectioning work into a much easier job. However, extra attention need to be paid to the images from the several cuttings right before starting to collect the serial images of the samples to make sure i) that the generated electron micrographs were well focused and aligned, and ii) the cuttings of the diamond knife were performed evenly and parallel on the whole region of the FoV.

## 2.6 Focused Ion Beam (FIB) Tomography

Focused ion beam (FIB) tomography is another 3D electron imaging method based on the serial sectioning technique. Instead of using physically visible diamond knife, energy sources, the focused ion beams are employed for cutting in FIB tomography. Like SBFSEM, it is a destructive imaging approach. Also like SBFSEM, the resolution of FIB tomography on the imaging planes (xy planes in figure 2.22) depends on the electron microscope used and the resolution along the cutting direction (z direction in figure 2.22) is determined by the slice

thickness and the accuracy of image alignment. Different from SBFSEM, not only BSE signals can be collected to form images in FIB tomographic measurements, but also second electron (SE) and ion-induced second electron (ISE) signals.

The first work of 3D FIB tomography was performed at the end of the 20th century [80, 81]. Later on, it has been widely used in materials structure investigations covering such as metallic multilayer [82], metal alloys (figure 2.20) [83-85], ceramics (figure 2.21) [86, 87]. FIB tomography can be performed using either single focused ion beam (FIB) or dual-beam (FIB-SEM) instruments. However, the job is generally fulfilled by FIB-SEM dual-beam system after its availability.

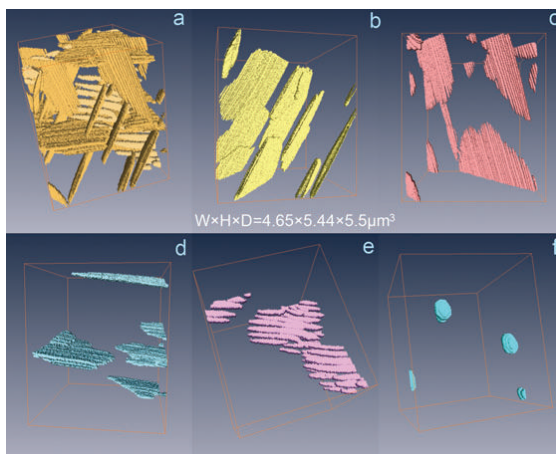


Figure 2. 20: 3D reconstruction of all the  $\text{Ni}_4\text{Ti}_3$  precipitates (a), four kinds of variants of precipitates (b–e), and TiC impurity (f). (From reference [85])

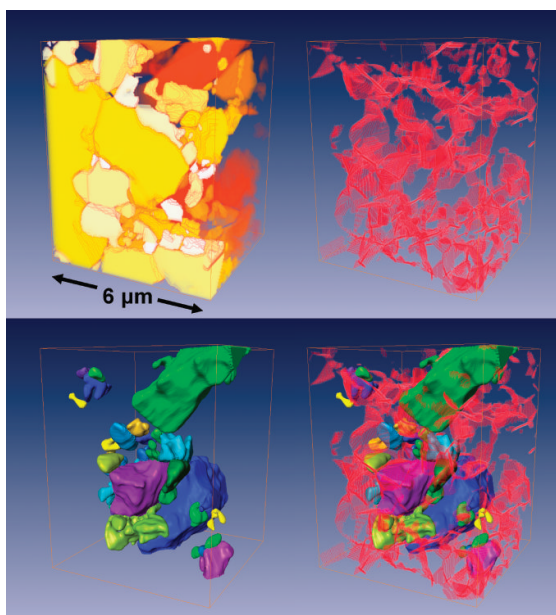


Figure 2. 21: Topological characterization of particle–particle interfaces based on 3D analysis with focused ion beam nano-tomography: All four images represent the same sample locality (volume size:  $6 \times 8 \times 6 \mu\text{m}^3$ ; voxel size:  $30 \text{ nm} \times 38 \text{ nm} \times 60 \text{ nm}$ ). Top left: Selected area from grain size fraction 3 with 150 particles. Top right: Interfaces of neighboring particles. Bottom left: Selection of 30 particles. Bottom right: Superposition of interfaces with selected particles. (From reference [87])

The FIB tomographic measurements are, just like SBFSEM, serial sectioning processes which are displayed representatively in figure 2.22 [86]. The general procedure of FIB tomography is described as following:

First, locate a region of interest (RoI) on the surface of the sample. Second, deposit a protective layer such as Pt film, typically 1  $\mu\text{m}$  thick, on the top of the RoI using FIB. This layer needs to cover the whole RoI to protect the target area from undesired ion induced (sputtering) erosion during measurements. The third step is fabricating external reference markers on the sample. This step is recommended, yet it is not compulsory for all cases, for instance, when the imaged volume of RoI contains high contrast object(s) which can be treated as internal markers. The external markers are often obtained by drilling holes, growing or using small features [88, 89] near the RoI (see figure 2.23). The markers are independent features for image alignment only, they are not components of the final out-put images [82, 88]. After this, trenches in front of, at the right and the left of the RoI need to be milled out by FIB as showing in figure 2.22. The geometry and sizes of the trenches should allow for cross-sectioned surface (xy plane in figure 2.22) imaging at an oblique angle with either the electron beam or the ion beam [82, 88]. The trench sizes must be large enough to prevent significant re-deposition of sputtered materials and ions back onto the imaging plane, and to eliminate shadowing of imaging signals which causes intensity variations [86]. Once a volume of interest (see figure 2.22) was created, the serial sectioning and imaging process can be carried out. The acquired 2D image slices are then stacked together after alignment and generate 3D images [90].

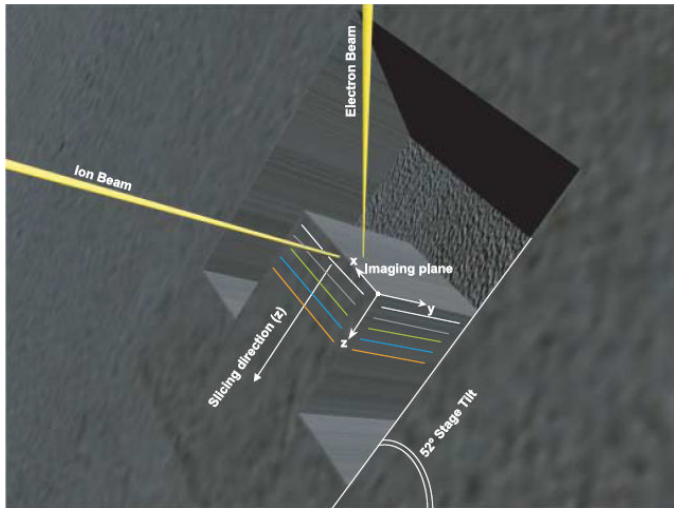


Figure 2. 22: Schematic illustration of a sample cube and geometrical relationships of the imaging plane with electron and ion beams in FIB tomography experiment. (From reference [86]).

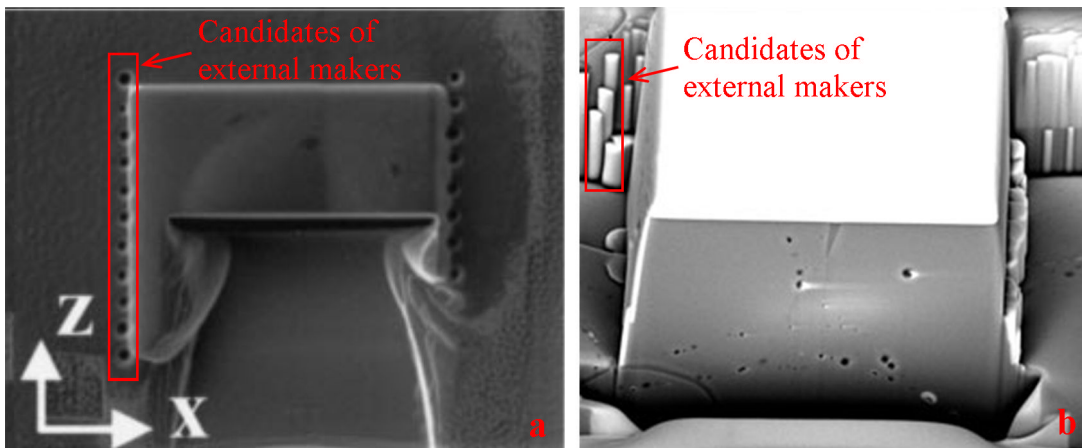


Figure 2. 23: External markers for FIB tomography. a, Candidates of external markers obtained by drilling holes in the sample using FIB. b, (Fabricated) small features can be used as external markers. (Panel a was adapted from figure 2d in the reference [88], panel b was adapted from figure 10c in the reference [89].)

These two serial sectioning 3D electron imaging methods, FIB tomography and SBFSEM measurements both can be done automatically. Although both techniques are destructive, the FIB cutting avoids direct physically mechanical contact with the samples which happened during the diamond knife cutting in SBFSEM measurements. This helps to alleviate the mechanical destructions of features of the samples, to reduce the possibilities of causing sample drift and distorting sample morphology compared with SBFSEM measurements. The image alignment of FIB tomography can be done by referring the external markers, the alignment of SBFSEM slices is depending on the high accuracy of mechanical components of

the system and is done by comparing successive slice cuts. The external marker alignment would provide higher accuracy and generate better and more reliable 3D images since the external markers are fixed and preserved in the samples during measurements and they are working as the position references for the images. However, SBFSEM measurements are performed in environmental SEM which can help to reduce charging effects of the samples. This is an advantage for non-conductive sample investigations such as biological samples comparing with FIB tomography which is performed in high vacuum SEM.

## References

- [1] Kak, A. C. & Slaney M. Principles of Computerized Tomographic Imaging (IEEE Press, New York, 1988).
- [2] Glenn, W. V., Jr., Johnston, R. J., Morton, P. E. & Dwyer, S. J. Image generation and display techniques for CT scan data-Thin transverse and reconstructed coronal and sagittal planes. *Invest. Radiol.* **10**, 403-416 (1975).
- [3] Uchic, M.D., Holzer, L., Inkson B.J., Principe, E.L. & Munroe, P. Three-Dimensional microstructural characterization using focused ion beam tomography. *MRS Bulletin.* **32**, 408-416 (2007).
- [4] Denk, W. & Horstmann, H. Serial block-face scanning electron microscopy to reconstruct three-dimensional tissue nanostructure. *PLoS Biol.* **2**, e329 (2004).
- [5] Cormack, A. M. Representation of a function by its line integrals, with some radiological applications. *Journal of Applied Physics.* **34**, 2722-2727 (1963).
- [6] Hounsfield, G.N. Historical notes on computerized axial tomography. *Journal of the Canadian Association of Radiologists.* **27**, 135-142 (1976).
- [7] Chao, W. *et al.* Soft X-ray microscopy at a spatial resolution better than 15 nm. *Nature.* **435**, 1210-1213 (2005).

- [8] Rehbein, S., Heim, S., Guttman, P., Werner, S. & Schneider, G., Ultrahigh-Resolution Soft-X-Ray Microscopy with Zone Plates in High Orders of Diffraction. *Phys. Rev. Lett.* **103**, 110801 (2009).
- [9] Tang, M.-T. *et al.* Hard X-ray Microscopy with Sub-30 nm Spatial Resolution at NSRRC. *Proceeding of 8th International Conference on X-ray Microscopy, IPAP conference series*, **7**, 15-17 (2006).
- [10] Chen, T. *et al.* Full-field microimaging with 8 keV X-rays achieves a spatial resolutions better than 20 nm. *Optics Express*. **19**, 19919-19924 (2011).
- [11] Vila-Comamala, J. *et al.* Characterization of high-resolution diffractive X-ray optics by ptychographic coherent diffractive imaging. *Optics Express*. **19**, 21333-21344 (2011).
- [12] Zschech, E., Yun, W. & Schneider, G. High-resolution X-ray imaging—a powerful nondestructive technique for applications in semiconductor industry. *Applied Physics A*. **92**, 423-429 (2008).
- [13] Larabell, C.A. & Le Gros, M.A. X-ray Tomography Generates 3-D Reconstructions of the Yeast, *Saccharomyces cerevisiae*, at 60-nm Resolution. *Molecular Biology of the Cell*. **15**, 957-962 (2004).
- [14] De Rosier, D. J. & Klug, A. Reconstruction of three dimensional structures from electron micrographs. *Nature*. **217**, 130-134 (1968).
- [15] Midgley, P.A. & Dunin-Borkowski, R.E. Electron tomography and holography in materials science. *Nature Mat.* **8**, 271-280 (2009).
- [16] Neuhäusler, U. *et al.* X-ray microscopy in Zernike phase contrast mode at 4keV photon energy with 60nm resolution. *Journal of Physics D: Applied Physics*. **36**, A79-A82 (2003).
- [17] Hsieh, J. *Computed Tomography: Principles, Design, Artifacts, and Recent Advances* (SPIE Press, Washington, 2003).

- [18] Zernike, F. Das Phasenkontrastverfahren bei der mikroskopischen Beobachtung. *Z. Techn. Physik.* **16**, 454-457 (1935).
- [19] Zernike, F. Phase Contrast, A New Method for the Microscopic Observation of Transparent Objects. *Physica IX.* **7**, 686-698 (1942) & **10**, 974-986 (1942).
- [20] Zernike, F. How I Discovered Phase Contrast. *Science.* **121**, 345-349 (1955).
- [21] Schmahl, G., Rudolph, D. & Schneider, G. *et al.* Phase Contrast X-ray Microscopy Studies. *Optik.* **97**, 181-182 (1994).
- [22] Schneider, G. Cryo X-ray microscopy with high spatial resolution in amplitude and phase contrast. *Ultramicroscopy.* **75**, 85-104 (1998).
- [23] Lüning, K. *et al.* A High Resolution Full Field Transmission X-ray Microscope at SSRL. *Synchrotron Radiation Instrumentation: Ninth International Conference.* 1333-1336 (2007)
- [24] NanoXCT Laboratory Tool User Manual, Xradia Inc.
- [25] Tang, M.-T. *et al.* Hard X-ray microscopy with sub 30 nm spatial resolution. *Synchrotron Radiation Instrument: Ninth International Conference.* 1274-1277 (2007).
- [26] Dierolf, M. *et al.* Ptychographic X-ray computed tomography at the nanoscale. *Nature.* **467**, 436-439 (2010).
- [27] Guizar-Sicairos, M. *et al.* Phase tomography from x-ray coherent diffractive imaging projections. *Opt. Express* **19**, 21345-21357 (2011).
- [28] Diaz A. *et al.* Quantitative x-ray phase nanotomography. *Phys. Rev. B* **85**, 020104(R) (2012).
- [29] Rodenburg, J. M. *et al.* Hard-X-Ray lensless imaging of extended objects. *Phys. Rev. Lett.* **98**, 034801 (2007).
- [30] Thibault, P. *et al.* High-resolution scanning X-ray diffraction microscopy. *Science.* **321**, 379 -382 (2008).

- [31] Pfeiffer, F., Kottler, C., Bunk, O. & David, C. Hard x-ray phase tomography with low-brilliance sources. *Phys. Rev. Lett.* **98**, 108105 (2007).
- [32] Hoppe, W. Beugung im Inhomogenen Primärstrahlwellenfeld. III. Amplituden- und Phasenbestimmung bei unperiodischen Objekten. *Acta Cryst. A* **25**, 508-514 (1969).
- (Hoppe, W. Diffraction in inhomogeneous primary wave fields. 3. Amplitude and phase determination for nonperiodic objects. *Acta Crystallogr. A* **25**, 508-514 (1969).)
- [33] Hoppe, W. Trace structure analysis, ptychography, phase tomography. *Ultramicroscopy* **10**, 187-198 (1982).
- [34] Miao, J., Charalambous, P., Kirz, J. & Sayre, D. Extending the methodology of X-ray crystallography to allow imaging of micrometre-sized non-crystalline specimens. *Nature* **400**, 342-344 (1999).
- [35] Shapiro, D. *et al.* Biological imaging by soft x-ray diffraction microscopy. *Proc. Natl. Acad. Sci. USA* **102**, 15343-15246 (2005).
- [36] Pfeifer, M.A., Williams, G.J., Vartanyants, I.A., Harder, R. & Robinson, I.K. Three-dimensional mapping of a deformation field inside a nanocrystal. *Nature* **442**, 63-66 (2006).
- [37] Chapman, H.N. *et al.* High-resolution ab initio three-dimensional x-ray diffraction microscopy. *J. Opt. Soc. Am. A* **23**, 1179-1200 (2006).
- [38] Rodenburg, J. M., Hurst, A. C. & Cullis, A. G. Transmission microscopy without lenses for objects of unlimited size. *Ultramicroscopy* **107**, 227-231 (2007).
- [39] Maiden, A.M., Rodenburg, J.M. & Humphry, M.J. Optical ptychography: a practical implementation with useful resolution. *Opt. Lett.* **35**, 2585-2587 (2010).
- [40] Humphry, M.J., Kraus, B., Hurst, A.C., Maiden, A.M. & Rodenburg, J.M. Ptychographic electron microscopy using high-angle dark-field scattering for sub-nanometre resolution imaging. *Nat. Commun.* **3**, 1-7 (2012).

- [41] Hue, F., Rodenburg, J.M., Maiden, A.M. & Midgley, P.A. Extended ptychography in the transmission electron microscope: Possibilities and limitations. *Ultramicroscopy* **111**, 1117-1123 (2011).
- [42] Faulkner, H. M. L. & Rodenburg, J. M. Movable aperture lensless transmission microscopy: a novel phase-retrieval algorithm. *Phys. Rev. Lett.* **93**, 023903 (2004).
- [43] Rodenburg, J. M. & Faulkner, H. M. L. A phase retrieval algorithm for shifting illumination. *Appl. Phys. Lett.* **85**, 4795-4797 (2004).
- [44] Maiden, A. M. & Rodenburg, J. M. An improved ptychographical phase retrieval algorithm for diffractive imaging. *Ultramicroscopy* **109**, 1256-1262 (2009).
- [45] Thibault, P., Dierolf, M., Bunk, O., Menzel, A. & Pfeiffer, F. Probe retrieval in ptychographic coherent diffractive imaging. *Ultramicroscopy* **109**, 338-343 (2009).
- [46] Bunk, O. *et al.* Influence of the overlap parameter on the convergence of the ptychographical iterative engine. *Ultramicroscopy* **108**, 481-487 (2008).
- [47] Henrich, B. *et al.* PILATUS: A single photon counting pixel detector for X-ray applications. *Nucl. Instrum. Meth. A* **607**, 247-249 (2009).
- [48] Dierolf, M. *et al.* Ptychographic coherent diffractive imaging of weakly scattering specimens. *N. J. Phys.* **12**, 035017 (2010).
- [49] Cloetens, P. *et al.* Holotomography: Quantitative phase tomography with micrometer resolution using hard synchrotron radiation x rays. *Appl. Phys. Lett.* **75**, 2912-2914 (1999).
- [50] Cloetens, P., Mache, R., Schlenker, M. & Lerbs-Mache, S. Quantitative phase tomography of Arabidopsis seeds reveals intercellular void network. *Proc. Natl Acad. Sci. USA* **103**, 14626-14630 (2006).
- [51] Cloetens, P., Barrett, R., Baruchel, J., Guigay, J. & Schlenker, M. Phase objects in synchrotron radiation hard x-ray imaging. *J. Phys. D: Appl. Phys.* **29**, 133-146 (1996).

- [52] Snigirev, A., Snigireva, I., Kohn, V., Kuznetsov, S. & Schelokov, I. On the possibilities of x-ray phase contrast microimaging by coherent high-energy synchrotron radiation. *Rev. Sci. Instrum.* **66**, 5486-5492 (1995).
- [53] Snigirev, A., Snigireva, I., Kohn, V.G. & Kuznetsov, S.M. On the requirements to the instrumentation for the new generation of the synchrotron radiation sources. Beryllium windows. *Nucl. Instrum. Meth. A.* **370**, 634-640 (1996).
- [54] Wilkins, S.W., Gureyev, T.E., Gao D., Pogany, A. & Stevenson, A.W. Phase-contrast imaging using polychromatic hard X-rays. *Nature* **384**, 335-338 (1996).
- [55] Cloetens, P. *et al.* Observation of microstructure and damage in materials by phase sensitive radiography and tomography. *J. Appl. Phys.* **81**, 5878-5886 (1997).
- [56] Mokso, R., Cloetens, P., Maire, E., Ludwig, W. & Buffière, J.-Y. Nanoscale zoom tomography with hard x rays using Kirkpatrick-Baez optics. *Appl. Phys. Lett.* **90**, 144104 (2007).
- [57] Requena, G. *et al.* Sub-micrometer synchrotron tomography of multiphase metals using Kirkpatrick-Baez optics. *Scripta Mater.* **61**, 760-763 (2009).
- [58] Bech, Martin. X-ray imaging with a grating interferometer. PhD Dissertation, University of Copenhagen, Copenhagen, Denmark. 2009.
- [59] Coene, W., Janssen, G., Op de Beeck, M. & Van Dyck, D. Phase retrieval through focus variation for ultra-resolution in field-emission transmission electron microscopy. *Phys. Rev. Lett.* **69**, 3743-3746 (1992).
- [60] Helfen, L., Baumbach, T., Cloetens, P. & Baruchel, J. Phase-contrast and holographic computed laminography. *Appl. Phys. Lett.* **94**, 104103 (2009).
- [61] Helfen, L. *et al.* High-resolution three-dimensional imaging of flat objects by synchrotron-radiation computed laminography. *Appl. Phys. Lett.* **86**, 071915 (2005).

- [62] Helfen, L. *et al.* Synchrotron-radiation computed laminography for high-resolution three-dimensional imaging of flat devices. *Phys. Stat. Sol. (a)* **204**, 2760-2765 (2007).
- [63] Xu, F., Helfen, L., Baumbach, T. & Suhonen, H. Comparison of image quality in computed laminography and tomography. *Opt. Exp.* **20**, 794-806 (2012).
- [64] Chen, B. *et al.* Coherent x-ray diffraction imaging of paint pigment particles by scanning a phase plate modulator. *New J. Phys.* **13**, 103022 (2011).
- [65] Zhang, F., Pedrini, G. & Osten, W. Phase retrieval of arbitrary complex-valued fields through aperture-plane modulation. *Phys. Rev. A* **75**, 043805 (2007).
- [66] Johnson, I. *et al.* Coherent diffractive imaging using phase front modifications. *Phys. Rev. Lett.* **100**, 155503 (2008).
- [67] Ingal, V. N. & Beliaevskaya, E. A. X-ray plane-wave topography observation of the phase contrast from a non-crystalline object. *J. Phys. D: Appl. Phys.* **28**, 2314-2317 (1995).
- [68] Davis, T.J., Gao, D., Gureyev, T.E., Stevenson, A.W. & Wilkins, S.W. Phase-contrast imaging of weakly absorbing materials using hard X-rays. *Nature* **373**, 595-598 (1995).
- [69] Bonse, U. & Hart, M. An X-ray interferometer. *Appl. Phys. Lett.* **6**, 155-156 (1965).
- [70] Momose, A., Takeda, T., Itai, Y. & Hirano, K. Phase-contrast X-ray computed tomography for observing biological soft tissues. *Nature Medicine*, **2**, 473-475 (1996).
- [71] Weitkamp, T. *et al.* X-ray phase imaging with a grating interferometer. *Opt. Exp.* **13**, 6296-6304 (2005).
- [72] Denk, W. & Horstmann, H. Serial block-face scanning electron microscopy to reconstruct three-dimensional tissue nanostructure. *PLoS Biol.* **2**, e329 (2004).
- [73] Levinthal, C. & Ware, R. Three dimensional reconstruction from serial sections. *Nature* **236**, 207-210 (1972).
- [74] Arenkiel, B. R. & Ehlers, M. D. Molecular genetics and imaging technologies for circuitbased neuroanatomy. *Nature* **461**, 900-907 (2009).

- [75] O'Brien, H. C. & McKinley, G. M. New microtome and sectioning method for electron microscopy. *Science* **98**, 455-456 (1943).
- [76] Fernández-Morán, H. Electron microscope observations on the structure of the myelinated nerve fiber sheath. *Exp. Cell Res.* **1**, 143-149 (1950).
- [77] Rouquette, J. *et al.* Revealing the high-resolution three-dimensional network of chromatin and interchromatin space: A novel electron-microscopic approach to reconstructing nuclear architecture. *Chromosome Res.* **17**, 801-810 (2009).
- [78] Müller-Reichert, T., Mancuso, J., Lich, B. & McDonald, K. Three-dimensional reconstruction methods for *Caenorhabditis elegans* ultrastructure. *Methods Cell Biol.* **96**, 331-361 (2010).
- [79] Briggman, K. L., Helmstaedter, M. & Denk, W. Wiring specificity in the directionselectivity circuit of the retina. *Nature* **471**, 183-188 (2011).
- [80] Torniyasu, B., Fukuju, I., Komatsubara, H., Owari, M. & Nihei, Y. High spatial resolution 3D analysis of materials using gallium focused ion beam secondary ion mass spectrometry (FIB SIMS). *Nucl. Instrum. Meth. B.* **136-138**, 1028-1033 (1998).
- [81] Dunn, D. N. & Hull, R. Reconstruction of three-dimensional chemistry and geometry using focused ion beam microscopy. *Appl. Phys. Lett.* **75**, 3414-3416 (1999).
- [82] Steer, T. J., Möbus, G., Kraft, O., Wagner, T. & Inkson, B. J. 3-D focused ion beam mapping of nanoindentation zones in a Cu-Ti multilayered coating. *Thin Solid Films.* **413**, 147-154 (2002).
- [83] Inkson, B. J., Mulvihill, M. & Möbus, G. 3D determination of grain shape in a FeAl-based nanocomposite by 3D FIB tomography. *Scripta Materialia.* **45**, 753-758 (2001).
- [84] Uchic, M. D., Groeber, M. A., Dimiduk, D. M. & Simmons, J. P. 3D microstructural characterization of nickel superalloys via serial-sectioning using a dual beam FIB-SEM. *Scripta Materialia.* **55**, 23-28 (2006).

- [85] Cao, S., Tirry, W., Van Den Broek, W. & Schryvers, D. Optimization of a FIB/SEM slice-and-view study of the 3D distribution of Ni<sub>4</sub>Ti<sub>3</sub> precipitates in Ni–Ti. *J. Microsc.* **233**, 61-68 (2009).
- [86] Holzer, L., Indutnyi, F., Gasser, P., Münch, B. & Wegmann, M. Three-dimensional analysis of porous BaTiO<sub>3</sub> ceramics using FIB nanotomography. *J. Microsc.* **216**, 84-95 (2004).
- [87] Holzer, L., Muench, B., Wegmann, M. & Gasser, P. FIB-Nanotomography of Particulate Systems Part I & II. *J. Am. Ceram. Soc.* **89**, 2577-2595 (2006).
- [88] Inkson, B. J., Steer, T., Möbus, G. & Wager, T. Subsurface nanoindentation deformation of Cu-Al multilayers mapped in 3D by focused ion beam microscopy. *J. Microsc.* **201**, 256-269 (2001).
- [89] De Winter, D. A. M. *et al.* Tomography of insulating biological and geological materials using focused ion beam (FIB) sectioning and low-kV BSE imaging. *J. Microsc.* **233**, 372-383 (2009).
- [90] Uchic, M. D., Holzer, L., Inkson, B. J., Principe, E. L. & Munroe, P. Three-Dimensional Microstructural Characterization Using Focused Ion Beam Tomography. *MRS Bulletin.* **32**, 408-416 (2007).

## **Chapter 3**

# **Investigation of Three-Dimensional Spatial Structures of the Silver Epoxy Adhesive by Transmission X-ray Microscopy**

In this chapter, three-dimensional (3D) spatial structure images from X-ray nano-tomography of the silver epoxy adhesive sample are presented. The images showed shapes, sizes and spatial distribution of the silver particles embedded in the material and revealed the 3D conductive network formed by the particles in the coating film which is responsible for its thermal and electrical properties.

### **3.1 Introduction**

Silver particle filled epoxy is a common thermally and electrically conducting adhesive material in widespread use which has been extensively studied [1-6]. These coatings have been increasingly applied as adhesives for interconnections of electrical conductors in the microelectronics industry over four decades. The most demanding application of the silver epoxy adhesives is the attachment of silicon chips to substrates or heat sinks because they have high thermal conductivity as well as electrical conductivity, and they are good in mechanical integrity [7]. In fact, it is their good thermal conduction rather than electrical conduction which is utilized in these cases [8] as the speed of modern integrated circuits is

largely determined by the efficiency of heat removal from the active semiconductor structures. In addition, the reliability of the chips rapidly declines when they work at increased operating temperatures as they have a practical maximum operating temperature [7].

The stable highly thermal and electrical conductivities of these adhesives are provided by plate silver particles embedded inside them. Once the concentration of the silver particles exceeds a critical value in the material, conductive paths are formed [9]. Right at the critical concentration, a “percolation transition” takes place in which a conductive “path” begins to form within the insulating matrix, epoxy resin here. Upon further increase of the silver particle concentration, a three dimensional (3D) network of conductive paths can be formed, and the conductivity of the cured adhesive layer remains practically constant [9]. Additionally, the use of physically strong and adhering epoxy resin improves the mechanical integrity of the composite [10].

Percolation theory [11, 12] is able to describe the conductive properties of the silver epoxy adhesive coating and how it should change with particle concentration. However, there is little information available on the 3D structures which needed to understand the physical origin of the conductive performances. In this work, we measured a commercial silver epoxy adhesive by conventional X-ray tomography [13-14] using transmission X-ray microscopy (TXM) to reveal the physical 3D network of conductive paths in the material. The two main components of the target samples are flake-shaped pure silver particles and pure epoxy resin. The latter is the matrix material and the silver particles, typically sized around a few microns, are typically making up 80% of the sample’s weight.

### **3.2 Experiments**

The X-ray tomographic measurements were done by using Xradia’s NanoXCT. The target samples were cured dry silver epoxy coating films. Before measurement, the samples were

peeled off their substrates to become free-standing films. Then, the films were cut to tiny triangle- or pin-shaped samples (see contents in section 2.1.3 and figure 3.1) by hand using scalpels. The cut samples were then mounted in the sample holders designed for TXM measurements. Since the silver particles in the samples would provide high absorption contrast and they sized at micron level, so there is no need for external markers such as gold micro-particles to be added for referencing. The silver particles at the top of the sample tips were used as reference markers.

The 3D X-ray tomographic experiments of silver epoxy adhesive coating samples were done with laboratory-source based Xradia's NanoXCT at the Henry Moseley X-ray Imaging Facility at the University of Manchester, Manchester, UK. The measurement using the NanoXCT was performed under absorption contrast (only) mode using 8.05 keV ( $\lambda \approx 1.54 \text{ \AA}$ ) X-rays. The field of view (FoV) of  $66 \times 66 \text{ \mu m}^2$  was provided.

For the NanoXCT measurements, the incident beam was focused by a capillary condenser onto the sample. The X-ray beam transmitted by the sample was refocused by a Fresnel zone plate, and then projected onto the CCD detector to form a projection image.

### **3.3 Results and Discussion**

The following section presents the experiment results of a silver epoxy adhesive specimen from the measurements made at the University of Manchester. The NanoXCT was operated under absorption contrast mode with 150 nm resolution. Figure 3.1 is a series of projections of a free standing film sample. In figure 3.1, the left projection is acquired at  $-90^\circ$ , the middle one is at  $0^\circ$  and the right one is at  $90^\circ$ . The sizes of the projections are  $66 \times 66 \text{ \mu m}^2$ .

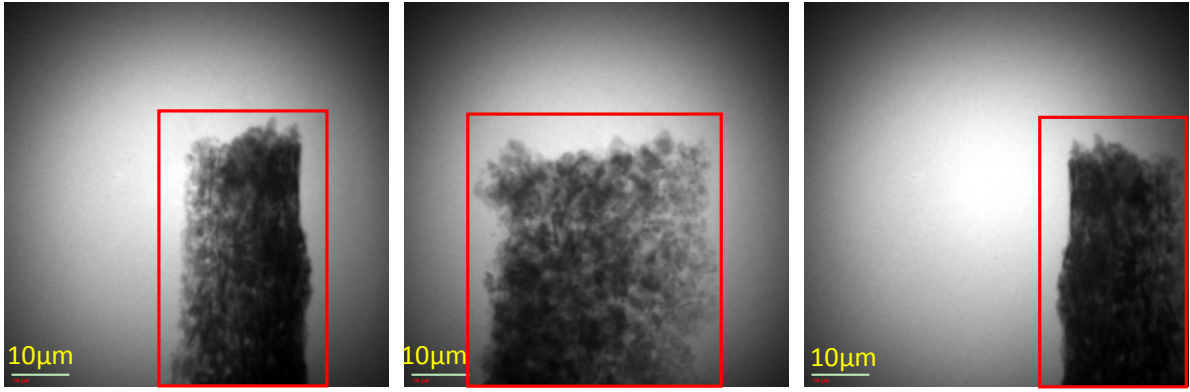


Figure 3. 1: A series of projections of a silver epoxy adhesive sample. Left, A projection at  $-90^\circ$ . Middle, A projection at  $0^\circ$ . Right, A projection at  $90^\circ$ .

Since the measurements were done under absorption contrast mode, the epoxy appears almost transparent under illumination at 8.05 KeV X-rays (as confirmed by the results of the aluminium epoxy marine coating sample that was presented in chapter 6). This means the epoxy has only minor contributions to the projection images. Here, we can be sure that the blacker parts, framed by the red rectangles in figure 3.1, (ignoring the non-uniform background features in the 4 corner areas), are the silver particles because they have much higher X-ray absorption capabilities than the epoxy resin.

After the tomographic reconstruction, a 3D image of the sample was generated from a series of 2D projections. Figure 3.2 is the rendering of the reconstructed 3D spatial structure image of the sample. The right image corresponds to rotating the left one by about  $270^\circ$  clockwise. In figure 3.2, we can clearly see many (white) particles whose sizes are around 4 microns. They are the silver particles in the sample. From these 3D images, we can see that the shapes of the particles are not pellet-like, but plate-like which is in good agreement with the information provided by the manufacturer.

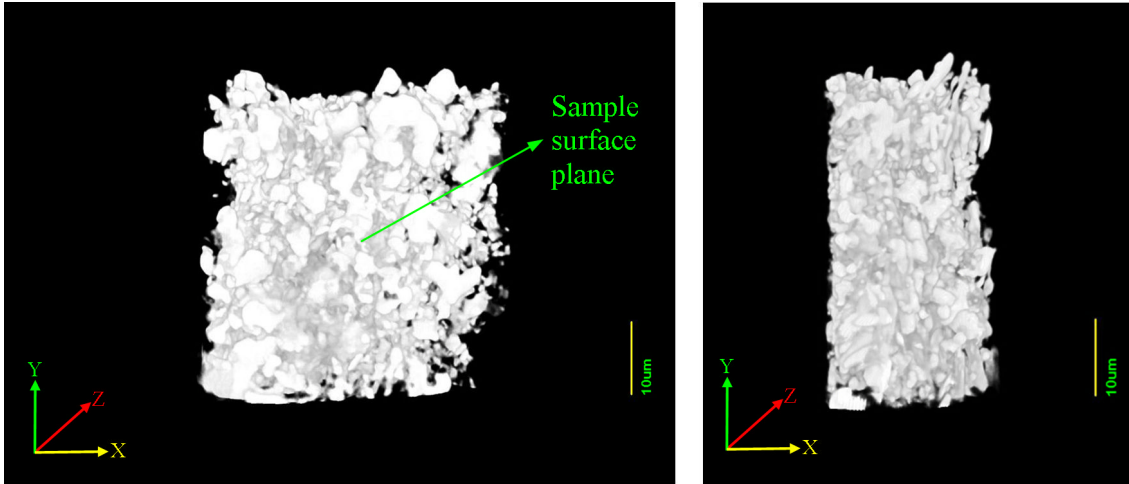


Figure 3. 2: Two views of the rendering of the tomographic 3D image of the silver epoxy adhesive sample from the TXM measurements of figure 3.1. The right image is obtained by rotating the left one by about  $270^\circ$  clockwise.

The images in figure 3.3 are the cross-sections of the 3D image of the sample in the  $zx$  plane, perpendicular to the rotation axis  $y$  (see axis labels in figure 3.2). As the sample was standing vertically to the horizontal plane ( $zx$  plane) and its surface plane was also perpendicular to the horizontal plane as shown in the left image of figure 3.2. The cross-section images in figure 3.3 reveal how the sample structure evolves from its (external) film surface to its application surface (interface between the coating film and the substrate) at various heights of the sample. However, we still cannot definitively identify which side is which. Ideally, both sides should be flat and straight like the lower side, and they should be parallel to each other as the yellow broken lines indicate in figure 3.3. The ideal shapes of the sample cross-sections should be like rectangles, not wedges as shown in these cross-section images. This was should be caused by the hand-cutting during the sample preparation which normally produces a random shape.

We can see that the silver particles are cross-contacted and that their inter-connections tend to be oriented towards the surface normal. However, along the direction parallel to the surfaces, the connections between the particles are frequently interrupted. In the vicinity of the two

surfaces, the silver plates tend to arrange themselves nearly parallel to the surface plane (see the lower sides of figure 3.3). In the commercial products, this general structural arrangement would be expected to enhance the desired properties. The bulk of the coating films would have higher thermal conductivity as the heat can pass the coating films directly along interconnected silver particle contacts lying vertically to both surfaces. Additionally, the near-parallel arrangement of the silver particles around the surfaces enlarges their contacting area to both external interfaces which are the semiconductor device and the heat sink. This would improve the heat transfer capabilities of the products because the silver particles have larger contact area at both sides.

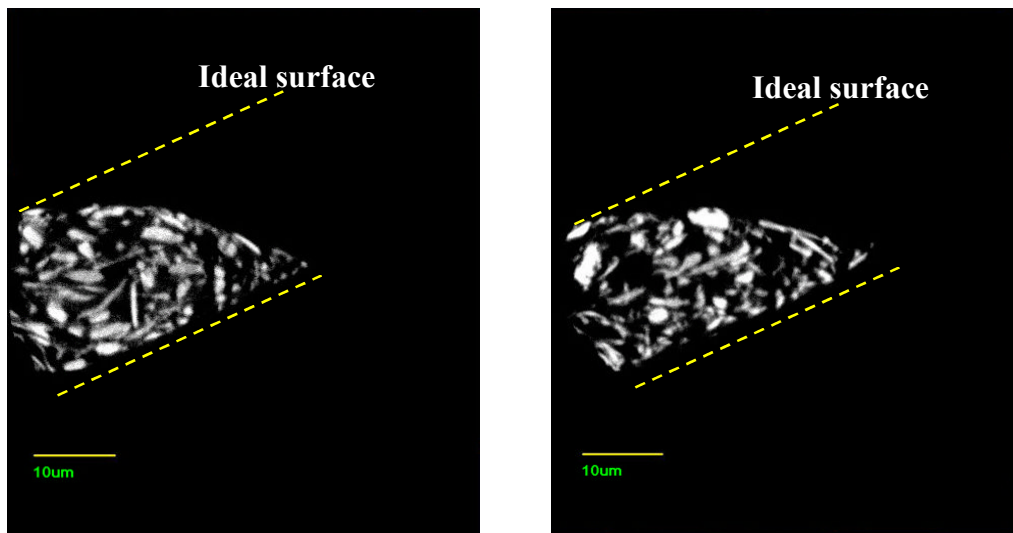


Figure 3. 3: Tomographic cross-sections of the 3D image of the silver epoxy adhesive sample in the zx plane (perpendicular to the tomography rotation axis).

### 3.4 Conclusions and Future Work

The 3D spatial structure of the silver epoxy adhesive sample was revealed by the transmission X-ray microscopy (TXM) measurements. TXM was verified to be a useful tool to investigate the structures of this absorption(-contrast) sample. The 3D conductive path network of the silver particles within the sample was physically visualized. The thermal and electrical conductivities of this two-phase composite material are apparently enhanced by two

factors: perpendicular grain orientation in the bulk and by parallel orientation next to the external surfaces. Further quantitative analysis of the 3D structure images could be performed in the future. Detailed finite-element simulations of the thermal and electrical conductivities of the sample based on its real 3D structure is also planned in the future.

## References

- [1] Lu, D., Tong, Q. K. & Wong, C. P. Conductivity Mechanisms of Isotropic Conductive Adhesives (ICA's). *IEEE Trans. Electron. Packag. Manufact.* **22**, 223-227 (1999).
- [2] Kim, K. D. & Chung, D. D. L. Effect of Heating on the Electrical Resistivity of Conductive Adhesive and Soldered Joints. *J. Electron. Mater.* **31**, 933-939 (2002).
- [3] Jiang, H., Moon, K.-S., Lu, J. & Wong C. P. Conductivity Enhancement of Nano Silver-Filled Conductive Adhesives by Particle Surface Functionalization. *J. Electron. Mater.* **34**, 1432-1439 (2005).
- [4] Tan, F., Qiao, X., Chen, J. & Wang, H. Effects of coupling agents on the properties of epoxy-based electrically conductive adhesives. *Int. J. Adhesion & Adhesives* **26**, 406-413 (2006).
- [5] Guan, Y., Chen, X., Li, F. & Gao, H. Study on the curing process and shearing tests of die attachment by Ag-epoxy electrically conductive adhesive. *Int. J. Adhesion & Adhesives* **30**, 80-88 (2010).
- [6] Johnsen, G. K., Knaapila, M., Martinsen, Ø.G. & Helgesen, G. Conductivity enhancement of silver filled polymer composites through electric field alignment, *Compos. Sci. Technol.* in press (2012).
- [7] Bjorneklett, A., Halbo, L. & Kristiansen, H. Thermal conductivity of epoxy adhesives filled with silver particles. *Int. J. Adhesion & Adhesives* **12**, 99-104 (1992).
- [8] Kang, S. K. & Purushothaman, S. Development of Conducting Adhesive Materials for Microelectronic Applications. *J. Electron. Mater.* **28**, 1314-1318 (1999).

- [9] Psarras, G. C. Conduction Processes in Percolative Epoxy Resin Silver Particles Composites. *Science of Advanced Materials* **1**, 101-106 (2009).
- [10] Leong, C.-K. & Chung, D. D. L. Improving the Electrical and Mechanical Behavior of Electrically Conductive Paint by Partial Replacement of Silver by Carbon Black. *J. Electron. Mater.* **35**, 118-122 (2006).
- [11] Essam, J. W. Percolation theory. *Rep. Prog. Phys.* **43**, 833-912 (1980).
- [12] Grimmett, G. *Percolation* (2nd edition) (Springer, Berlin, 1999).
- [13] Kak, A. C. & Slaney M. *Principles of Computerized Tomographic Imaging* (IEEE Press, New York, 1988).
- [14] Hsieh, J. *Computed Tomography: Principles, Design, Artifacts, and Recent Advances* (SPIE Press, Washington, 2003).

## **Chapter 4**

### **Wave-front Modulation Coherent X-ray Diffraction Imaging of the Iron Oxide Alkyd Paint**

This chapter is based on a paper was published in the New Journal of Physics in 2011, volume 13, page 103022, titled as “Coherent x-ray diffraction imaging of paint pigment particles by scanning a phase plate modulator” with the co-authors: Fucai Zhang, Felisa Berenguer, Richard J. Bean, Cameron M. Kewish, Joan Vila-Comamala, Yong S. Chu, John M. Rodenburg and Ian K. Robinson. The figures and text were prepared by myself in correspondence with all these authors. I was involved in the wave-front modulation coherent X-ray diffraction experiments at the cSAXS beamline at the Swiss Light Source, Paul Scherrer Institut. The phase retrieval of the wave-front modulation coherent X-ray diffraction imaging data was then performed by Fucai Zhang. The transmission X-ray microscope measurement was done by myself with the help of the beamline scientist at the beamline 32-ID-C of the Advanced Photon Source, Argonne National Laboratory.

In this chapter, we have implemented a coherent X-ray diffraction imaging technique which scans a phase plate to modulate wave-fronts of the X-ray beam transmitted by samples. The method was applied to measure a decorative alkyd paint containing iron oxide red pigment particles. By employing an iterative algorithm for wave-front modulation phase retrieval, we

obtained an image of the paint sample which shows distribution of the pigment particles and it is consistent with result obtained from a transmission X-ray microscope (TXM). The technique was experimentally proven to be a feasible coherent X-ray imaging method with about 120 nm spatial resolution and was shown to work well with industrially relevant specimens.

#### **4.1 Introduction**

With the use of modern synchrotron X-ray sources, coherent X-ray diffraction imaging has been successfully applied to materials and biological science [1-7] since its first demonstration by J. Miao and his colleagues [8]. The technique has been well-developing both experimentally [7, 9, 10] and algorithmically [11-14] in order to circumvent its original limitations such as the isolated sample requirements under coherent X-ray illumination and the difficulties associated with obtaining a unique image solution by reconstructing a single diffraction pattern of a sample using phase retrieval algorithms.

Here, we present a wave-front modulation coherent X-ray diffraction imaging system [15, 16] which uses a newly-developed algorithm for phase retrieval. The method can be applied to extended samples without tight support constraints and provides a unique solution to the phase retrieval process without stagnation. To verify its feasibility, experiment had been performed on an industrial alkyd paint sample. This type of paint is one of the most important varieties of coating in the world [17], and its chemical construction and physical performances have been widely studied for a long time [17-21].

The measured alkyd paint specimen consists of 2 main components, alkyd resin and iron oxide particles, which act as film former/binder and pigment of the paint, respectively. The sample is a decorative coating with high ultraviolet (UV) resistant capabilities which are generated from the iron oxide particles whose maximum size is 500 nm, according to

information provided by the manufacturer. The UV resistance is crucial to the service life of outdoor coatings since, in numerous cases, UV radiation induces the majority of chemical and physical breakdown of the substrates and paint coatings themselves [22]. These iron oxide particles are effective absorbers of UV radiation, providing essential protection to the substrates and the alkyd resin and, consequently, ensuring that the cured coating films have long service life and high colour stability. These performances of the paint are dominated by the distribution of iron oxide particles in the alkyd resin. In this paper, we present a practical method for measuring this property which is the subject of on-going investigations.

## **4.2 Experiment and Methods**

Figure 4.1 schematically illustrates experimental set-up of this imaging method. A phase plate with a known, random pattern is inserted in the X-ray path between the sample and the detector, functioning as a wave-front modulator.

There are 3 planes perpendicularly intersecting the primary X-ray optical axis which are of relevance in this coherent X-ray imaging method: the sample plane, the phase plate/modulator plane and the detector plane (these planes are labeled in figure 4.1 as S, P and D, respectively). During the experiment, the phase plate is scanned linearly or circularly in the plane P. At each phase plate position, a diffraction pattern of the same illuminated region of the sample is acquired [15, 16]. An image of the sample is obtained from these diffraction patterns without prior knowledge of the structure of the illuminating X-ray probe. However, the phase distribution function of the phase plate and the parameters of the experiment set-up geometry are measured carefully and given as input to a phase retrieval algorithm. The algorithm uses an iterative calculation which cycles back and forth between the phase plate and the detector planes.

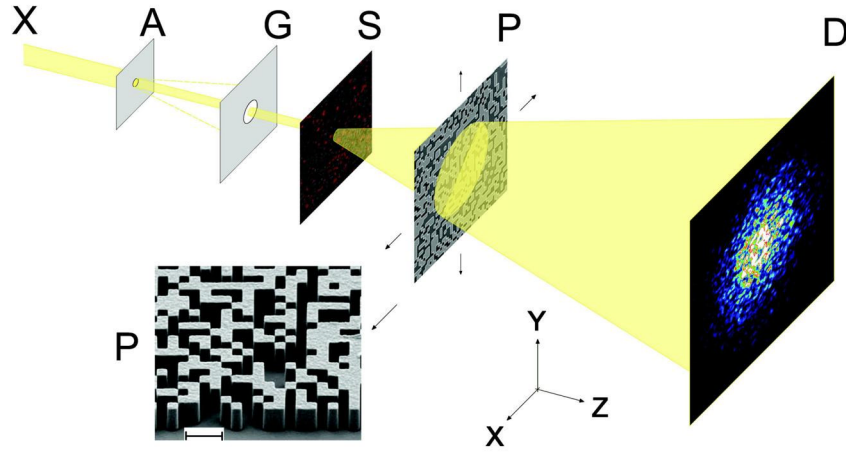


Figure 4. 1: Schematic of the experimental set-up. The X-ray beam (X) travels from left to right. A coherent part of the beam is selected by a pinhole aperture (A), and scattering is removed by a guard aperture (G). The sample (S) diffracts the coherent beam, and the wave-fronts are then modulated by a phase plate modulator (P). The detector (D) measures the diffraction patterns in the far-field of the sample. The inset P is a scanning electron micrograph of the nanofabricated phase plate, on which the scale bar represents 1 micron.

The iterative procedure starts from an original random estimate  $\psi_n$  ( $n$  is the iteration number, and  $n = 0$  here) of the X-ray wave-front before the phase plate and then repetitively runs with the following steps:

- (1) Modulate the estimated  $\psi_n$  with the phase distribution function of the plate, and generate a modulated wave-front  $\psi'_n$ ;
- (2) Propagate the  $\psi'_n$  to the detector using a Fourier transform to obtain an estimated diffraction pattern  $\Psi_n^d$ . Here, the Fourier transform is used because the far field recording geometry is employed in our experiment. For a near field recording geometry, the Fresnel propagator can be used instead;
- (3) Replace magnitude of  $\Psi_n^d$  by square root of the measured intensity of the diffraction pattern to obtain an updated diffraction pattern of wave-front  $\Psi_n^{d'}$ ;

(4) Back propagate  $\Psi_n''$  to the phase plate plane using an inverse Fourier transform;

(5) Remove the phase distribution function of the plate to obtain an updated estimate  $\psi_{n+1}$  of the wave-front before the phase plate;

(6) Repeat steps 1–5 at the next phase plate position. If the last plate position were reached, then use the first one again, and the iterative process cycles through the recorded diffraction patterns.

The convergence of the iterative process is monitored by the normalized root-mean-square error [23]. When there is no further improvement of the reconstruction quality, the iteration ends and an exit wave of the object has been generated on the phase plate. Finally, the image of the object is acquired by further back propagating the wave-front to the sample plane using an angular spectrum algorithm [24].

The experiment was carried out at the cSAXS beamline at Swiss Light Source (SLS) on a piece of cured iron oxide alkyd paint film which was several millimeters wide and about 25 microns thick. The sample had experienced 3 min mechanical agitation before it was applied onto a polypropylene (PP) substrate. The cured dry sample was then peeled off the substrate as a free-standing film. An X-ray beam from an undulator insertion device was used for the experiment. A double-crystal Si(111) monochromator was used to select X-rays of energy 6.2 keV ( $\lambda \approx 2.0 \text{ \AA}$ ) from the beam. A 10  $\mu\text{m}$  diameter pinhole aperture (denoted by A in figure 4.1) was installed 183 mm upstream of the sample to select a coherent part of incident beam. A guard aperture (marked as G in figure 4.1) which is 100  $\mu\text{m}$  in diameter followed the pinhole. It was installed 23 mm upstream of the sample to block scattered X-rays from the aperture. A random-patterned phase plate was positioned 24 mm downstream of the sample. The plate [25], shown in the inset P of figure 4.1, comprised a randomly filled grid of

$300 \times 300 \text{ nm}^2$  “pixels” designed to shift the phases of wave-fronts by 0 (empty pixels) or  $\pi$  radians (1.1  $\mu\text{m}$ -thick Au pixels) under the 6.2 keV X-ray illumination. The phase plate was mounted on a piezoelectric translation stage. The distance between the phase plate and the X-ray detector (a CCD camera from Princeton Instruments, 16 bits cooled, 1:1 optical taper coupling, columnar CsI scintillator, effective pixel size  $20 \times 20 \mu\text{m}^2$ ) was 7 m to ensure far field diffraction conditions. During measurements, the phase plate was scanned transversely to the beam by the piezoelectric translation stage linearly or circularly in 600 nm steps, and 5 diffraction patterns were acquired at different phase plate positions. Each diffraction pattern consisted of the sum of 10 accumulated 2 s exposures. The same scan with identical positions of the phase plate was then recorded without a sample in the X-ray path to obtain structure of the X-ray illumination beam which is treated to be a background illumination function. This allowed the contributions from the beamline and the sample to be separated.

Full-field X-ray imaging measurements were performed on the same iron oxide alkyd paint sample by a transmission X-ray microscope (TXM) at beamline 32 ID-C of the Advanced Photon Source (APS) at the Argonne National Laboratory (ANL) in order to verify reliability of the coherent X-ray imaging method. The TXM was operated under Zernike phase contrast mode using 8.0 keV ( $\lambda \approx 1.5 \text{ \AA}$ ) X-ray source. The incident beam was focused by a capillary condenser onto the sample. The transmitted X-ray beam by the sample was refocused by a Fresnel zone plate and went through a Zernike phase ring, then projected onto a CCD detector to form a projection image.

### **4.3 Results and Discussion**

Figures 4.2a and 4.2b present amplitude images of the X-ray illumination and the sample, respectively, reconstructed using the iterative method described above. Figure 4.2b was derived by dividing image of the illumination (figure 4.2a) from the image of the sample

under illumination. Figure 4.2c is a two-dimensional (2D) projection of a different region of the same sample from the TXM at beamline 32 ID-C of the APS. The TXM projection is an absorption contrast dominated image. Compared with figure 4.2a, many black dots can be clearly seen in figure 4.2b. Similar black dots are obviously observed in figure 4.2c as well. We identify these dots as iron oxide particles. The size of these particles is around 300 nm which is in good agreement with the size of iron oxide red pigment particles provided by the manufacturer. In figure 4.2b, the iron oxide particles are neither homogeneously distributed, nor seriously agglomerated in the alkyd resin. A similar distribution of the iron oxide particles can also be observed in figure 4.2c. This may cause the cured coating film to have relatively lower UV resistance at some regions and stops it producing optimal UV resistance.

A recognizable pattern of the illumination beam can be seen in the sample amplitude image (figure 4.2b). This can be attributed to incomplete subtraction of the reconstruction of the illumination beam from that of the sample (with illumination), possibly related to instrument instability between the two measurements.

Introduction of the wave-front modulator is essential for the success of the method, although the choice of phase plate pattern can be somewhat arbitrary, if it could provide sufficient modulation to the X-ray wave-fronts. For instance, a uniformly redundant array (URA) pattern plate would work well in the system. The installed phase plate is claimed to be random-patterned because the pixels in the grid are randomly “filled” with gold or left empty. This type of plate is expected to perform efficiently with all kinds of samples, and is not specifically customized to imaging paint coatings. Employment of the random-patterned phase plate minimizes correlations among the recorded diffraction patterns, and maximizes the retrievable information from single acquisition, because the plate redistributes every object point of the transmitted beam by the specimen to the whole sensing region of detector. Consequently, the influence of noise and the required dynamic range of the detector are

dramatically reduced, which releases us from using a central beam stop and its resulting in massive information loss. Furthermore, it helps to overcome stagnation of the phase retrieval process because the random phase plate effectually breaks possible symmetries in the object field during measurements. As a result, the algorithm converges rapidly and offers the routine a unique solution.

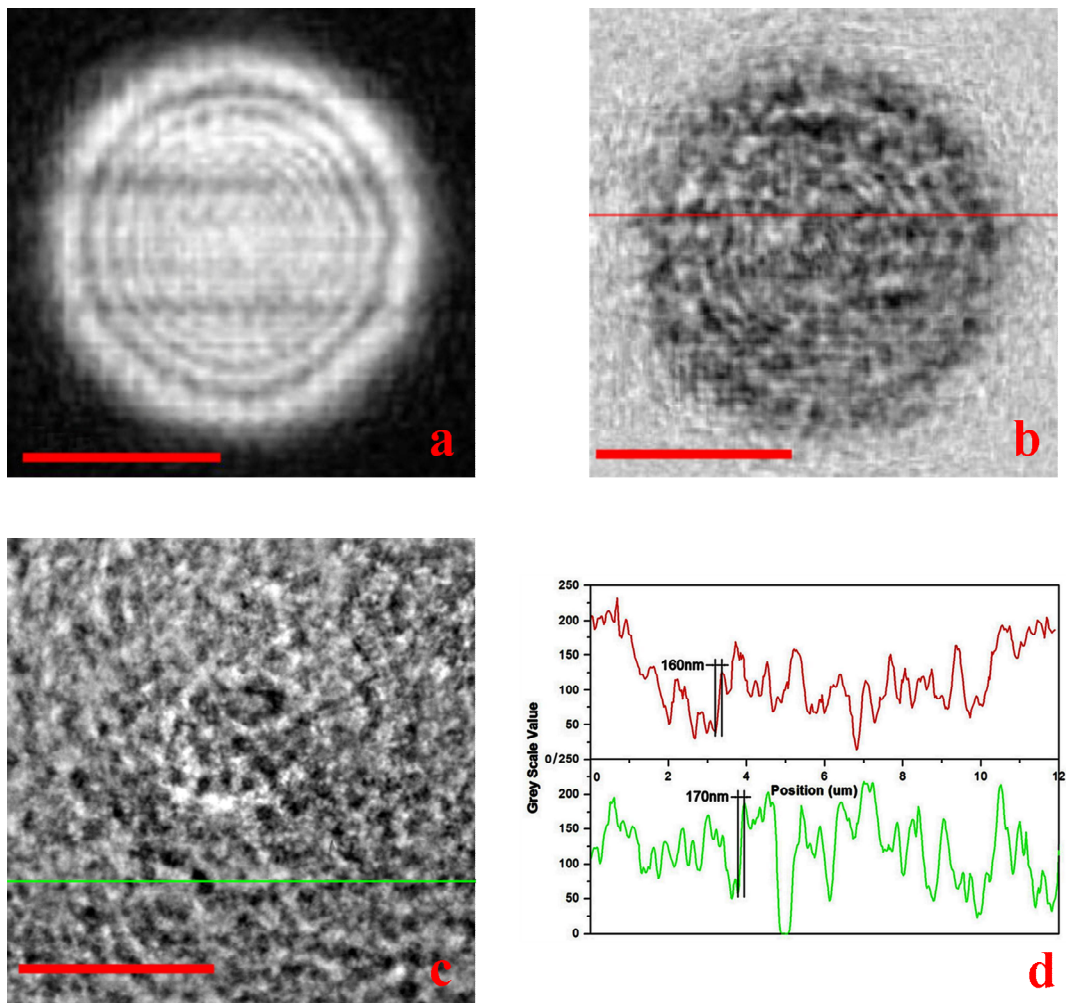


Figure 4. 2: a, Amplitude image of the illuminating X-ray source (only) reconstructed by the coherent X-ray imaging method; b, Reconstructed amplitude image of the paint sample; c, 2D TXM projection of a different region of the same paint sample; d, Plots of the images along the lines in figures 4.2b and 4.2c: the upper red curve is the amplitude plot along the red line in figure 4.2b, the lower green curve is the plot along the green line in figure 4.2c. The scale bars in figures 4.2a, 4.2b and 4.2c represent 5 microns.

In the imaging system, the resolution of the reconstructed images can be evaluated by the lateral width of the variation of signal from 10% to 90% at boundaries of features in images [16]. By this criterion, the approximate resolution of the reconstructed amplitude image from our method and the 2D projection from the TXM are both around 120 nm (see figure 4.2d). The achievable resolution of the TXM at the 32-ID-C APS is 38 nm for the configuration used for this work [26]. For our method, the resolution is dependent upon the detection solid angle and the scattering strength of the sample, which for the present geometry was verified can achieve a similar resolution, in practice, to the TXM we used.

Theoretically, the same as conventional coherent diffractive imaging (CDI), resolution of this wave-front modulation method depends on the solid angle of the detector that is filled with statistically significant intensities which can be reliably phased with the reconstruction algorithm. That is, just having a big detector does not guarantee high resolution unless there is enough scattering (from the samples) to fill it up. So, in principle, when measuring the same sample, the wave-front modulation method can reach the same resolution as the conventional CDI can.

The main factor makes the resolution of the wave-front modulation method we presented here lower than the conventional CDI is the instability of the system which comes from X-ray sources, device and sample aspects. This is also the common factor makes the scanning CDI methods such as ptychography normally have lower resolution than the conventional CDI. The instability of X-ray sources causes intensity and coherence fluctuation of the illumination on the samples. The instability of mechanical components connected to the wave-front modulators (or samples) produces “inaccurate” movements and causes the input values of the modulator (or sample) positions to the algorithm “unprecise”. The possible radiation damage to the samples during the (overlapping ptychographic) scans would also introduce errors to the phase retrieval process. All the factors above practically limit the resolution of the wave-

front modulation method which is, so far, lower than the conventional CDI. Once all these practical limits were solved, the wave-front modulation method should reach similar resolution to the conventional CDI and the recognisable pattern of the illumination beam in the sample amplitude image, figure 4.2b, should fade away as well.

Specifically, for our experimental set-up here, since the phase distribution function of the plate was used to modulate wave-front functions, and the phase modulator is in the near field of the sample which is illuminated by a parallel beam, so the phase distribution function of the modulator has direct effect on the reconstruction quality and the external knowledge of the phase modulator is another factor limits the resolution of the method. In the reported case, the highest resolution of the reconstructed images can reach is the highest accuracy we know the phase distribution function of the used modulator, equally, we need to know at least the phase distribution of the modulator to the same resolution as the desired reconstruction images because, in current case, the wave-front propagation between the sample and modulator is modeled as Fresnel diffraction. However, this is not a fatal limitation of the resolution of the method as we can characterize the phase modulator using scanning electron microscopy (SEM) which routinely acquires images with spatial resolution of about 2 nm. Therefore we can know the phase distribution function of the modulator to much higher resolution than current X-ray microscopies can reach. Yet, if a convergent beam were used to illuminate the sample, it is not necessary to know the phase modulator at the same resolution as the desired reconstruction because, in this case, the phase modulator can be treated in the far field of the sample. The wave-front propagation between the sample and modulator can be modeled as Fourier transform. The resolution at the sample/object plane, namely, the resolution of the reconstructed images, is determined by the angle extent of the wave field received by and pass through the modulator, which is the same relation as between the object and detector in conventional CDI. Because of the same reason, if the measured samples had

strong scattering capabilities which can scatter the exit wave-fronts from themselves to big enough angle extent to be received by the modulators, the resolution of the method, theoretically, can achieve the same resolution as the conventional CDI as well.

We are no longer requiring a beam stop when the phase modulator was used because the intensity diffracted by each point of the sample is re-spread to a larger area of the detector by the modulator. This means that we do not lose the information that felt behind the beam stop anymore (the small angle information). There is also an additional advantage, because the modulator spreads all object points to the whole detector area, that we are now getting some information from the higher orders of diffraction of the sample which was not accessible before. This is why using the random modulator, actually, can improve the resolution of the method. Also, the modulator improves the signal-to-noise ratio when spreading the diffracted intensity within the detector area. So, for the same sample, in practice, the resolution of the wave-front modulation method should not be lower than the conventional CDI.

Further evidence is that the images of the same specimen from both the transmission X-ray microscope (TXM) and our method have similar resolution as we addressed. In practice, the achievable resolution depends on the particular experiment. Furthermore, compared with TXMs using Fresnel zone plates, the resolution of the demonstrated wave-front modulation coherent X-ray imaging system is not fundamentally limited by the X-ray optical lens.

#### **4.4 Conclusions and Future Work**

In this chapter, we demonstrated a practical coherent X-ray imaging technique which achieved 120 nm spatial resolution using phase retrieval algorithm by introducing wave-front modulation in to solve the phase problem. It has been demonstrated that this method works well with industrial specimen. In principle, the utilization of the phase plate modulator provides us a method of producing very high resolution images without suffering from the

resolution limit imposed by the X-ray optics, such as the Fresnel zone plates, used in current TXMs. Relative to other coherent diffractive imaging techniques, our method also reduces the requirement for a high dynamic range of the detector. The associated iterative algorithm overcomes stagnation issues which occur in phase retrieval from single diffraction patterns (e.g., the “twin” images), and this method also allows us to measure extended samples.

In future, we intend to achieve larger field of view and higher spatial resolution. Developing it into a single-shot X-ray imaging system for extended samples is an important part of our future work. In the single-shot imaging system [27], the multiple phase modulator positions are not required anymore and the unique image solution is provided by the reconstruction done from just only one single diffraction pattern.

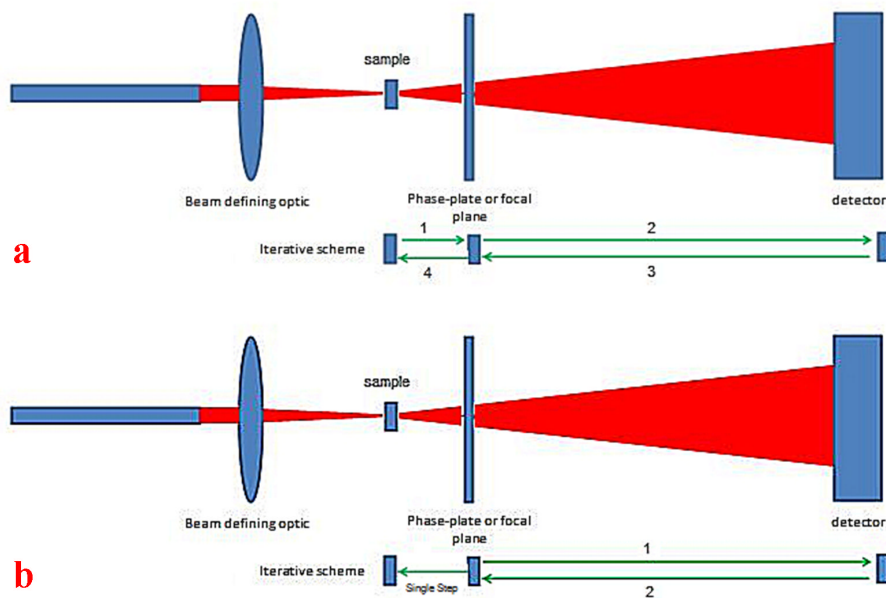


Figure 4. 3: Comparison between the algorithms used for single-shot imaging and the wave-front modulation method described here. a, single-shot imaging method. b, wave-front modulation method reported here.

In order to realize the single-shot imaging in the X-ray regime, we may need to know the phase distribution function of the modulator more accurately. The modulator itself probably

needs to be better fabricated than the current level too. Figure 4.3 shows a simplified comparison between the algorithms used for single-shot imaging method and the wave-front modulation coherent X-ray imaging method described here. Different from it, there are three planes involved in the iteration process of the algorithm for the single-shot imaging method instead of two in the reported one here, and Fresnel function and inverse Fresnel function were used to propagate the wave-fronts between the sample and the phase plate planes. The single-shot X-ray imaging system for extended samples has great potential applications in the 4th generation light sources, such as X-ray free electron lasers which have very high potentiality to damage the samples.

## References

- [1] Williams, G. J., Pfeifer, M. A., Vartanyants, I. A. & Robinson, I. K. Three- Dimensional Imaging of Microstructure in Au Nanocrystals. *Phys. Rev. Lett.* **90**, 175501 (2003).
- [2] Shapiro, D. *et al.* Biological imaging by soft x-ray diffraction microscopy. *Proc. Natl. Acad. Sci. U.S.A.* **102**, 15343-15346 (2005).
- [3] Chapman, H. N. *et al.* Femtosecond diffractive imaging with a soft-X-ray free-electron laser. *Nature Phys.* **2**, 839-843 (2006).
- [4] Abbey, B. Quantitative coherent diffractive imaging of an integrated circuit at a spatial resolution of 20 nm. *Appl. Phys. Lett.* **93**, 214101 (2008).
- [5] Berenguer de la Cuesta, F. *et al.* Coherent X-ray diffraction from collagenous soft tissues. *Proc. Natl. Acad. Sci. U.S.A.* **106**, 15297-15301 (2009).
- [6] Nishino, Y., Takahashi, Y., Imamoto, N., Ishikawa, T. & Maeshima, K. Three-Dimensional Visualization of a Human Chromosome Using Coherent X-Ray Diffraction. *Phys. Rev. Lett.* **102**, 018101 (2009).
- [7] Dierolf, M. *et al.* Ptychographic X-ray computed tomography at the nanoscale. *Nature* **467**, 436-439 (2010).

- [8] Miao, J., Charalambous, P., Kirz, J. & Sayre, D. Extending the methodology of X-ray crystallography to allow imaging of micrometre-sized non-crystalline specimens. *Nature* **400**, 342-344 (1999).
- [9] Rodenburg, J. M. *et al.* Hard-X-Ray Lensless Imaging of Extended Objects. *Phys. Rev. Lett.* **98**, 034801 (2007).
- [10] Abbey, B. *et al.* Keyhole coherent diffractive imaging. *Nature Phys.* **4**, 394-398 (2008).
- [11] Fienup, J. R. Phase retrieval algorithms: a comparison. *Appl. Opt.* **21**, 2758-2769 (1982).
- [12] Fienup, J. R. & Wackerman, C. C. Phase-retrieval stagnation problems and solutions. *J. Opt. Soc. Am. A* **3**, 1897-1907 (1986).
- [13] Faulkner, H. M. L. & Rodenburg, J. M. Movable Aperture Lensless Transmission Microscopy: A Novel Phase Retrieval Algorithm. *Phys. Rev. Lett.* **93**, 023903 (2004).
- [14] Thibault, P., Dierolf, M., Bunk, O., Menzel, A. & Pfeiffer, F. Probe retrieval in ptychographic coherent diffractive imaging. *Ultramicroscopy* **109**, 338-343 (2009).
- [15] Zhang, F., Pedrini, G. & Osten, W. Phase retrieval of arbitrary complex-valued fields through aperture-plane modulation. *Phys. Rev. A* **75**, 043805 (2007).
- [16] Johnson, I. *et al.* Coherent Diffractive Imaging Using Phase Front Modifications. *Phys. Rev. Lett.* **100**, 155503 (2008).
- [17] Reddy, V. A., Sampathkumaran, P. S. & Gedam, P. H. Effect of oil length of alkyd on the physico-chemical properties of its coatings. *Prog. Org. Coat.* **14**, 87-97 (1986).
- [18] Burns, D. T. & Doolan, K. P. A comparison of pyrolysis-gas chromatography- mass spectrometry and Fourier transform infrared spectroscopy for the analysis of a series of modified alkyd paint resins. *Anal. Chim. Acta.* **422**, 217-230 (2000).
- [19] Shareef, K. M. A. & Yaseen, M. Thixotropic properties of yellow iron oxide-alkyd paints: their dependence on pigment-resin-solvent interactions. *Prog. Org. Coat.* **13**, 347-365 (1985).

- [20] Popa, M. V. *et al.* The pigment influence on the anticorrosive performance of some alkyd films. *Mater. Chem. Phys.* **100**, 296-303 (2006).
- [21] Kumar, A., Vemula, P.K., Ajayan, P.M. & John, G. Silver-nanoparticle-embedded antimicrobial paints based on vegetable oil. *Nature Mater.* **7**, 236-241 (2008).
- [22] Pospíšil, J. & Nešpurek, S. Photostabilization of coatings. Mechanisms and performance. *Progr. Polym. Sci.* **25**, 1261-1335 (2000).
- [23] Fienup, J. R. Invariant error metrics for image reconstruction. *Appl. Opt.* **36**, 8352-8357 (1997).
- [24] Goodman, J. W. *Introduction to Fourier Optics* (2nd Edition) (McGraw-Hill Inc., New York, London, 1996, pp55-58).
- [25] Gorelick, S. *et al.* Direct e-beam writing of high aspect ratio nanostructures in PMMA: A tool for diffractive X-ray optics fabrication. *Microelectron. Eng.* **87**, 1052-1056 (2010).
- [26] Chu, Y. S. *et al.* Hard-x-ray microscopy with Fresnel zone plates reaches 40 nm Rayleigh resolution. *Appl. Phys. Lett.* **92**, 103119 (2008).
- [27] Zhang, F. & Rodenburg, J. M. Phase retrieval based on wave-front relay and modulation. *Phys. Rev. B* **82**, 121104(R) (2010).

## **Chapter 5**

### **Investigation of Three-Dimensional Spatial Structure of Iron Oxide Alkyd Paint**

In this chapter, three-dimensional (3D) spatial structure of iron oxide alkyd paint was investigated by conventional X-ray tomography using transmission X-ray microscopy (TXM), X-ray holo-tomography based on free space propagation phase contrast, ptychographic X-ray computed tomography and serial block-face scanning electron microscopy (SBFSEM). The 3D structure images obtained clearly revealed spatial distribution of the iron oxide particles in the cured coating films and presented aggregation level of the particles in the matrix resin. The sizes of clusters of the iron oxide particles were primarily analyzed, and the relations between spatial distribution of iron oxide particles and agitation processes during applications of the coating materials were discussed. The advantages and disadvantages of different 3D imaging techniques were also compared and stated.

#### **5.1 Introduction**

With intensive study [1-3], alkyd resin based paint has become one of the most important varieties of coating since the synthesis of alkyd resin in the 1930s [4]. Commonly, the term

“alkyd” is limited to polyesters modified with oils or fatty acids. A typical alkyd resin is prepared by heating for example linseed oil, phthalic acid anhydride and glycerol to obtain a fatty-acid containing polyester [5]. An Example of an alkyd resin used as a film former in alkyd resin based coating is presented in figure 5.1 [5].

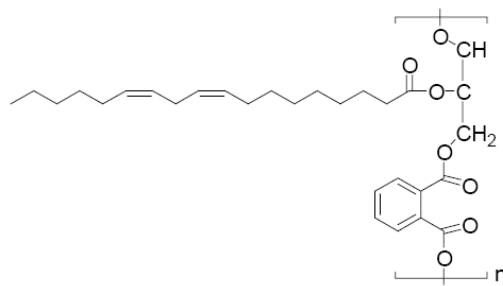


Figure 5. 1: An example of an alkyd resin used as a film former in the alkyd paint. The fatty acid chain shown is linoleic acid. This figure is from reference [5].

The target alkyd resin based coating is the same as the iron oxide alkyd paint studied in chapter 4. This is a decorative coating with strong ultraviolet (UV) resistant capabilities which is determined by the spatial distribution of the iron oxide particles in the cured coating films. The extent of the iron oxide particle dispersion in the matrix resin is critical for obtaining coating with efficient UV resistant performance, long service life and precise colour. Furthermore, since both the carbon footprint and the cost of a decorative paint are dominated by the amount of pigments used due to the energy required to produce pigments which are usually also the most expensive ingredients in coating materials. Getting pigments, including iron oxide particles, better dispersed means minimizing the amount of pigment used, which is the best way to reduce the carbon footprint and the cost of coatings.

3D imaging methods were employed to measure the alkyd paint samples to reveal the spatial distribution of iron oxide particles in the cured coating films which cannot be solved by 2D imaging. The results will help to understand the relationship between 3D spatial distribution of these particles and the ways of coating application, mainly different agitation processes treated here. To achieve this, cured iron oxide alkyd coating specimens experienced different agitation procedures, 1 minute mixing by hand (abbreviated to “1 minute mixing” in the

following), 3 minute mixing in a shaking machine (as done on the job-site practice, and abbreviated to “3 minute mixing” in the following) and 1 hour shaking in a can with beads (abbreviated to “1 hour mixing” in the following), were investigated. The first treatment is a very gentle mixing and the third one is a heavily severe mixing. The measurements were done by X-ray holo-tomography [6, 7], ptychographic X-ray computed tomography (PXCT) [8, 9], conventional X-ray tomography using transmission X-ray microscopy (TXM) [10, 11] and serial block-face scanning electron microscopy (SBFSEM) [12, 13].

## **5.2 3D Spatial Structure Investigation by X-ray Holo-tomography**

### **5.2.1 Experiments and Methods**

Two samples of iron oxide alkyd paint applied on polypropylene (PP) plate were measured by X-ray holo-tomography at the ESRF imaging beamline ID22-NI, where allows resolutions of below 100 nm to be reached [14, 15]. One of the samples experienced 3 minute mixing as done on the job-site, and the other one was treated by 1 hour mixing. The cured coating films were peeled off the substrate, and then cut to pin-shaped samples (see figure 2.10) of the required size by hand using scalpels. The sample surfaces were placed perpendicular to the mean beam propagation direction. 17 keV coherent X-ray source was selected for the measurements. The multilayer coated Kirkpatrick-Baez (KB) mirrors were used to focus the X-rays into a convergent beam with a focusing spot of 100 nm. The samples were placed behind the focus plane of the divergent X-ray beam (see figure 5.2).

The measurement of each specimen consists in a series of four tomographic scans at different sample-detector distances [14, 15]. The transmission images, actually Fresnel diffraction patterns, of the samples were recorded by an X-ray detector consisting of a scintillator, a charge-coupled device (CCD) based camera ( $2048 \times 2048$  pixels with the pixel size of  $24 \mu\text{m} \times 24 \mu\text{m}$ ). The detector system is set at a fixed distance,  $Z_s + Z_d$  in figure 5.2, of 1.2 m

downstream of the focus of the X-rays. Instead of changing position of the detector [6, 7], the samples were moved during measurements to reach four different sample-detector distances. Here, namely, different focus-sample distances  $Z_s$  at 29.2, 30.2, 34.2 and 44.2 mm, resulting in an image pixel size of  $40 \text{ nm} \times 40 \text{ nm}$ . For each distance, 2499 images over a  $180^\circ$  rotation were recorded. The complete measurement of each sample cost about 20 hours of beamtime. Before applying 3D reconstruction, the four images at each orientation recorded at different sample-detector distances  $Z_d$  were first cut to the same size with the same illumination area of the sample, and then phase retrieved to obtain single projections of the sample. The filtered back-projection algorithm was then applied to the phase projections to generate 3D images.

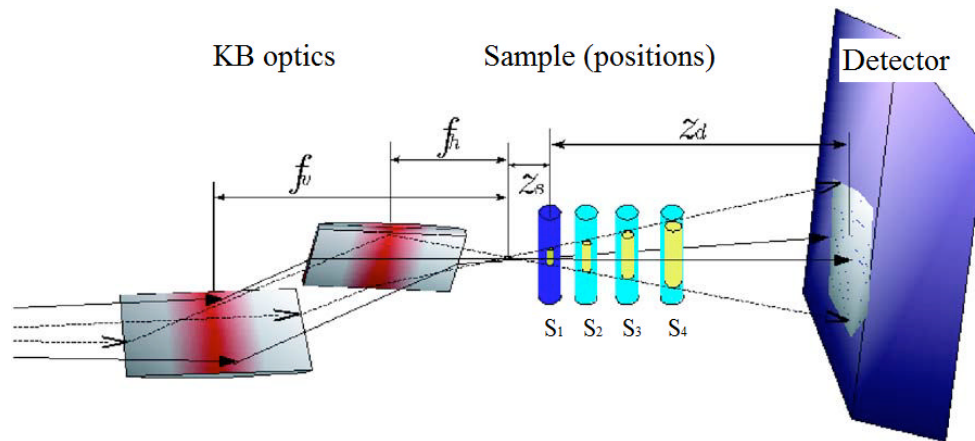


Figure 5. 2: Schematic experimental set-up of X-ray holo-tomography at the ESRF beamline ID22-NI. This figure is was adapted from figure 1 in the reference [14].

### 5.2.2 Results

Figure 5.3 presents tomogram slices perpendicular to the rotation axis of the reconstructed 3D volumes ( $82 \mu\text{m}$  high cylinders with  $82 \mu\text{m}$  diameter) of the two iron oxide alkyd paint samples from X-ray holo-tomographic measurements. Figure 5.3a, b and c are selected from the 3D volume of the 3 minute mixing sample, figure 5.3d, e and f are from the 1 hour mixing sample. According to the sample mounting geometry, the two arrowed long edges of the imaged samples in each panel of figure 5.3 are the coating surfaces and inter-faces.

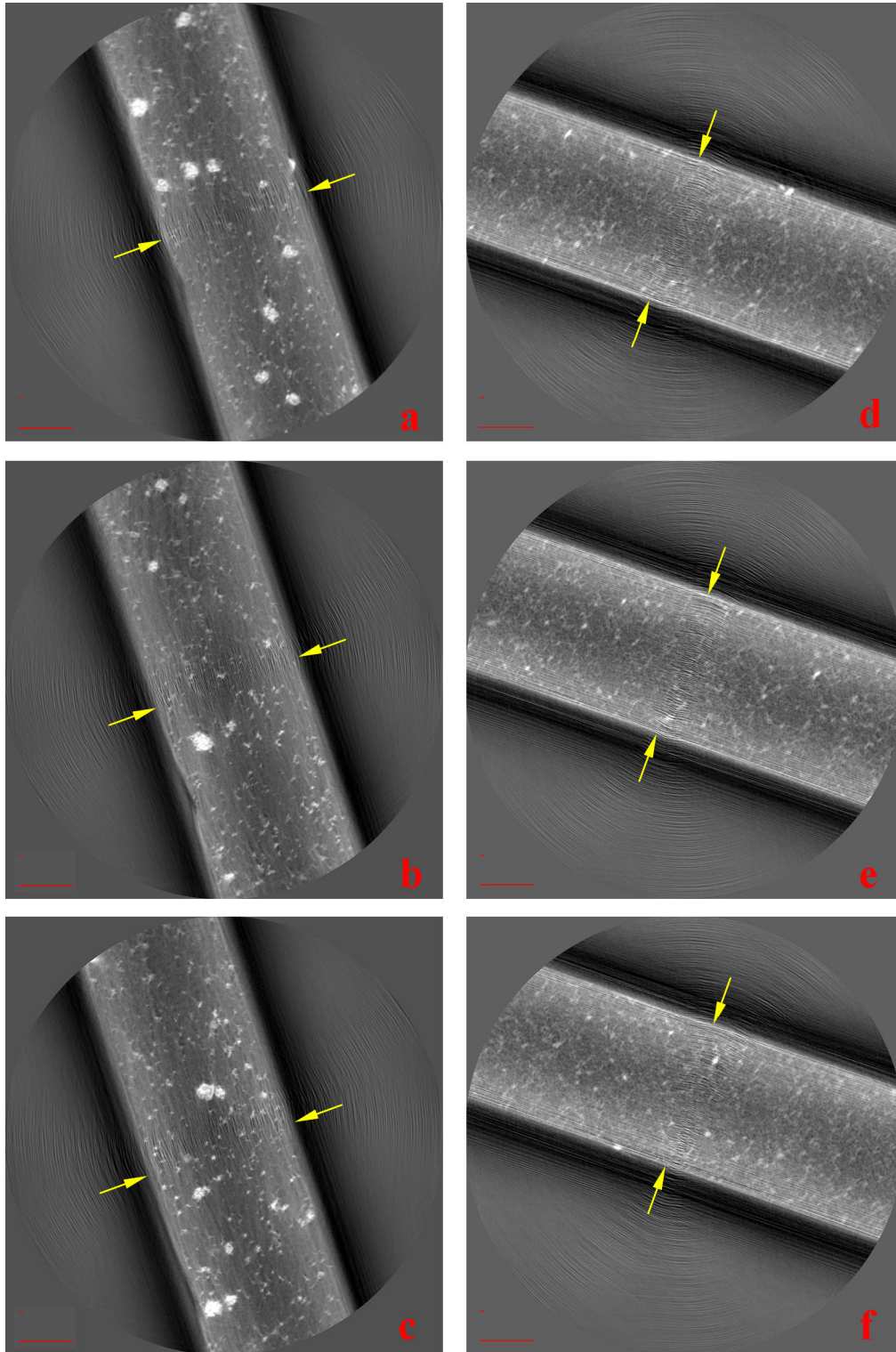


Figure 5. 3: Tomogram slices, with 21.6  $\mu\text{m}$  (540 slices) spacing, perpendicular to the rotation axis through the reconstructed 3D volumes of the iron oxide alkyd paint samples applied on PP plate from X-ray holo-tomographic measurements. a, b &c, Results for the 3 minute mixing sample; d, e & f, Results for the 1 hour mixing sample. The main scale bars in the panel images are 5 microns, and the minor scale bars (like red dots) are 500 nanometres.

Since these tomogram slices are actually electron density maps, and there are only two main components in the measured specimens, the bright regions in figure 5.3 are iron oxide particles and the remaining areas between the two (surface) edges are alkyd resin. Figure 5.3 clearly shows that the 3 minute mixing sample has quite a few clusters of the iron oxide particles, whereas, the particles in the 1 hour mixing sample has rather homogenous spatial distribution. The majority of the iron oxide particle clusters in the 3 minute mixing sample are approximately 2.5 microns big and the sizes of them range between 1.4 and 3.5 microns. Most distinguishable isolated iron oxide particles in both imaged samples are between 300 nm and 400 nm. This is in well agreement with both the information provided by the manufacturer that the maximum size of the iron oxide particles is 500 nm. This is also in agreement with the results achieved in chapter 4.

### **5.3 3D Spatial Structure Investigation by PXCT**

#### **5.3.1 Experiments and Methods**

The measurements of different regions of two samples, which are the same as studied by the X-ray holo-tomography, were performed at the cSAXS beamline (X12SA) of the Swiss Light Source, Paul Scherrer Institut, Switzerland, using X-rays of photon energy 6.2 keV. A 3  $\mu\text{m}$  pinhole was inserted 8 mm upstream of the sample along the X-ray propagation direction to define the coherent region of the incident beam. FIB fabricated cubic-shaped samples (see figure 5.4) were measured. X-ray diffraction patterns of the samples in transmission geometry were recorded by a PILATUS photon-counting detector (pixel size 172  $\mu\text{m}$   $\times$  172  $\mu\text{m}$ ) after they travelled through a 7 meters long flying tube. The full sample-detector distance was 7.2 meters. During the measurements, the samples were rotated through 180°. The specimen experienced 1 hour mixing was measured with 0.5° interval during rotation, obtained projections at 360 different orientations using about 18 hours. Because of the limitation of

beamtime, the sample treated by 3 minute mixing was measured with  $2.0^\circ$  interval, namely, only 90 projections of this sample were acquired. At each orientation angle, the samples were scanned to a number of different positions following a circular radial pattern with a  $1.4 \mu\text{m}$  radial step [16] in a plane perpendicular to the X-ray beam propagation direction to produce a field of view that can well cover the whole sample. The projections at individual orientations were then reconstructed by the difference map algorithm [17] from all diffraction patterns acquired at each orientation, then post-processed and reconstructed into 3D images according to the procedure described in reference [9].

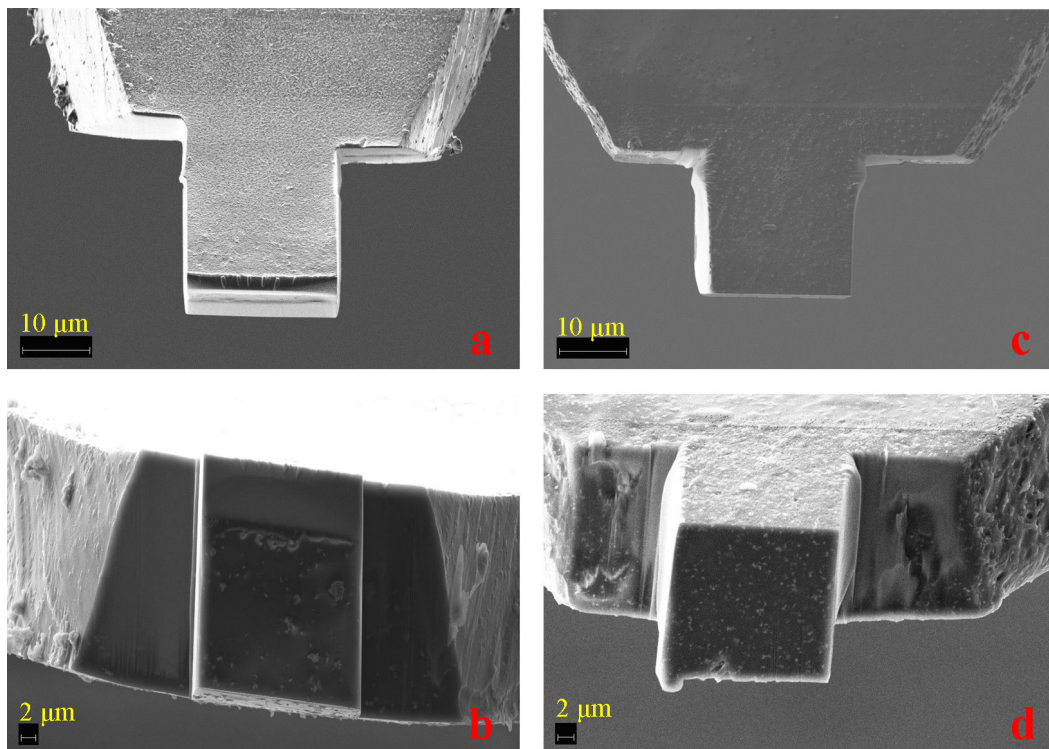


Figure 5. 4: FIB fabricated iron oxide alkyd paint samples (applied on PP plate). a & b, SEM images of the 3 minute mixing sample; c & d, SEM images of the 1 hour mixing sample.

### 5.3.2 Results

Figure 5.5a & b are the tomogram slices and rendering of the reconstructed 3D structure of the 3 minute mixing sample, and c & d are the corresponding results for the 1 hour mixing sample. The same as the images obtained from X-ray holo-tomographic measurements, in the

parts of reconstructed samples: bright regions are iron oxide particles, and darker areas are alkyd resin. From figure 5.5a & b, we can clearly see that there are iron oxide particle clusters in 3 minute mixing sample. Conversely, there is almost no aggregation in the 1 hour mixing sample. This agrees with the results from X-ray holo-tomography. The sizes of clusters in the cured 3 minute mixing coating film are ranging from about 1.5  $\mu\text{m}$  to 3.8  $\mu\text{m}$ .

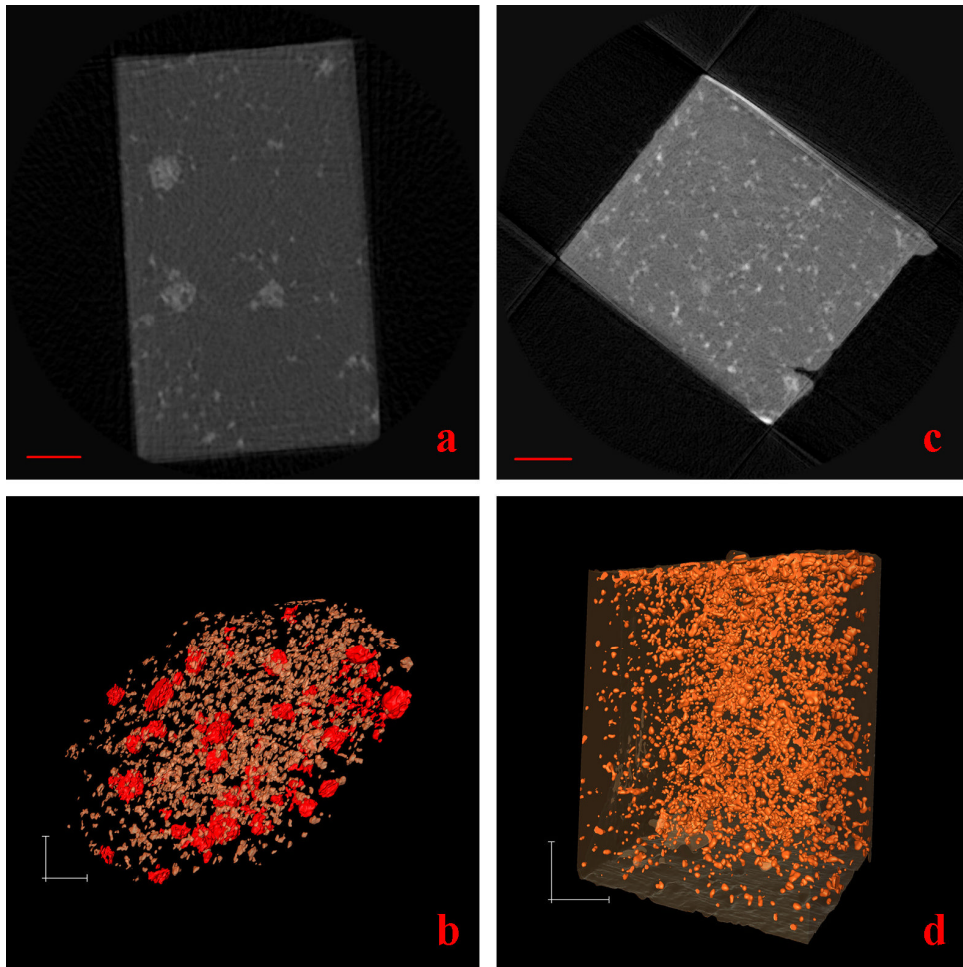


Figure 5. 5: Tomogram slices and rendering of the reconstructed 3D volumes of the iron oxide alkyd paints applied on PP plate from PXCT measurements. a & b, Results for the 3 minute mixing sample. The red parts in panel b are significant clusters of the iron oxide particles; c & d, Results for the 1 hour mixing sample. The scale bars are 5 microns.

In addition, we can easily observe that the obtained image of the 3 minute mixing sample has lower resolution than the image of the 1 hour mixing sample whose 3D reconstruction was

benefit from much more projections collected. This experimentally shows that 90 projections cannot provide enough information for a high-quality 3D tomographic reconstruction.

## **5.4 3D Spatial Structure Investigation by TXM**

### **5.4.1 Experiments**

A transmission X-ray microscope, Xradia's NanoXCT, was used to perform the conventional X-ray tomographic measurements of the alkyd paints. Two groups of samples were measured, one group were applied on polyethylene (PE) foil, the other group were applied on PP plate. There are three samples in each group: they are room-temperature cured coating films which had experienced 1 minute mixing, 3 minute mixing and 1 hour mixing, respectively. Again, the coating films were peeled off the substrate first, and then cut into tiny triangle- or pin-shaped samples (see figure 2.10 and following figure 5.6 & 5.7) by hand using scalpels. Gold micro-particles were then deposited on the tip of the group of samples applied on PP plate. The samples were then transferred to the microscope for X-ray tomographic measurements.

These X-ray tomographic experiments were done at the beamline 32ID-C, Advanced Photon Source (APS), Argonne National Laboratory (ANL), Argonne, USA. The Xradia's NanoXCT, which provides  $24 \times 24 \mu\text{m}^2$  field of view, was operated with 8.30 keV ( $\lambda \approx 1.49 \text{ \AA}$ ) X-ray illumination. The group of samples applied on PE foil were measured under Zernike phase contrast mode without depositing external reference markers – gold micro-particles. The other group applied on PP plate were measured under absorption contrast mode by using the externally deposited gold micro-particles as reference markers (see figure 2.10 and 2.11 and the contents in section 2.1.3). During about 4 hour experiment time for each sample, they were rotated  $180^\circ$  with  $0.25^\circ$  interval, 721 projections were collected and then used for 3D tomographic reconstructions.

### 5.4.2 Results

TXM measurements of the two groups of iron oxide alkyd paint samples that were applied on PE foil and PP plate, respectively, provided comparative and relevant results: figure 5.6 and figure 5.7. The panels a, b & c in figures 5.6 and 5.7 are projections of the samples at  $-40^\circ$ ,  $50^\circ$  and  $-40^\circ$ . The sizes of the projections are  $24 \times 24 \mu\text{m}^2$ . Since the results are absorption contrast (dominated) images, the black parts in the projections are iron oxide particles, the bright parts of the imaged specimens are alkyd resin, and the remaining areas are background. Panels d, e & f in both figures are the rendering of iron oxide particles in the reconstructed 3D images of the samples.

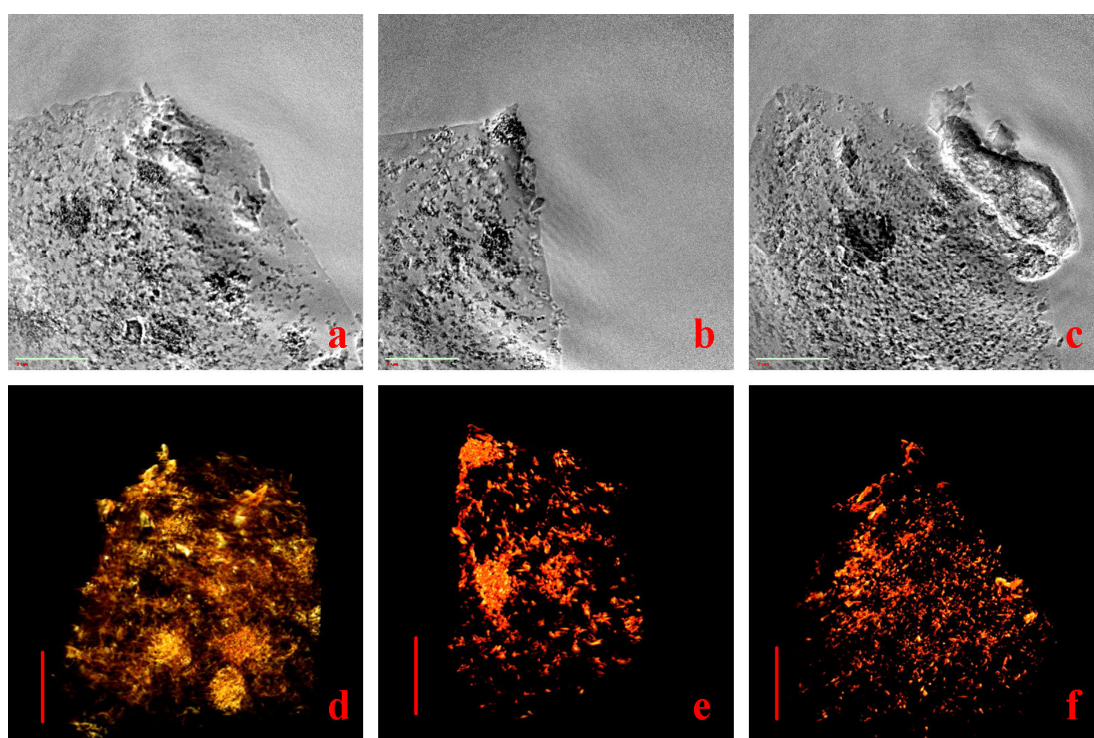


Figure 5. 6: TXM measurement results of the 1 minute mixing, 3 minute mixing and 1 hour mixing samples applied on PE foil. a, b & c, Projections of the samples at  $-40^\circ$ ,  $50^\circ$  and  $-40^\circ$ ; d, e & f, Rendering of iron oxide particles in the reconstructed 3D images. The scale bars are 5 microns.

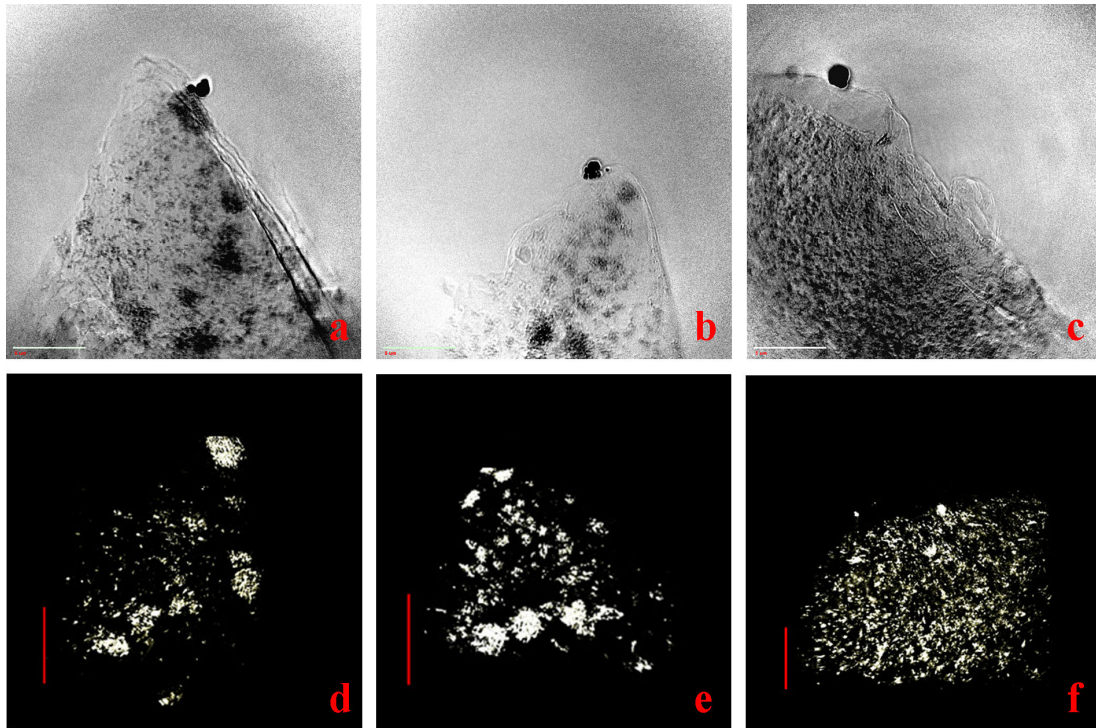


Figure 5. 7: TXM measurement results of the 1 minute mixing, 3 minute mixing and 1 hour mixing samples applied on PP plate. a, b & c, Projections of the samples at  $-40^\circ$ ,  $50^\circ$  and  $-40^\circ$ ; d, e & f, Rendering of iron oxide particles in the reconstructed 3D images. The scale bars are 5 microns.

We can find out that the 1 minute mixing and 3 minute mixing samples from both groups contain clusters of iron oxide particles at the first glance of generated images, and the 1 hour mixing samples do not have any noticeable aggregation. The results from these two groups of samples agree with each other and, again, verified the results from other X-ray measurements. The clusters in the 1 minute mixing samples from both groups size approximately between  $1.5\ \mu\text{m}$  and  $3.2\ \mu\text{m}$ . In parallel, from these measurements, the clusters in the 3 minute mixing samples have slightly smaller sizes that range from about  $1.4\ \mu\text{m}$  to  $2.7\ \mu\text{m}$ . This proves that the time of agitation for the coating materials before they have been applied on the substrates influences the spatial distribution of pigment particles in the cured coating films, and increasing the agitation time would improve uniformity of the spatial distribution of the pigment particles.

## 5.5 3D Spatial Structure Investigation by SBFSEM

### 5.5.1 Experiments

For comparison with X-ray imaging methods, a 3 minute mixing iron oxide alkyd paint sample applied on PP plate was measured by SBFSEM. Since the cured sample is a thin film, about 25  $\mu\text{m}$  thick, instead of reserving it in the epoxy resin, the film was fixed by gluing it directly on an aluminium specimen plate using cyanoacrylate glue. Once the glue cured, the specimen with the supporting aluminium plate was trimmed down by a microtome together to create a block face sizes around 500  $\mu\text{m}$   $\times$  500  $\mu\text{m}$  on the tip of the specimen.

The trimmed sample was measured by the SBFSEM system: 3View<sup>®</sup> from Gatan Inc. It was installed in a field emission gun (FEG) environmental SEM from FEI Company. The system was operated at 2.5 kV with 70 Pa chamber pressure in a water vapour environment. The back scattering electron (BSE) signals from the sample were acquired by the detector with output image pixel size 15 nm  $\times$  15 nm. The sectioning thickness was 15 nm per slice. The sample surface, attached with aluminium plate via the glue, was placed perpendicular to the moving direction of the diamond knife. It means that the cross-sections of the coating film from surface to the coating-substrate interface were imaged during measurement. Altogether 1000 slice images (15  $\mu\text{m}$  thick) with a field of view 30.7  $\mu\text{m}$   $\times$  30.7  $\mu\text{m}$  were obtained after about 8 hours serial sectioning and imaging process.

### 5.5.2 Results

Figure 5.8 demonstrates the result of SBFSEM measurement of the 3 minute mixing sample applied on PP plate. Compared with images produced by the above X-ray measurements, this electron imaging approach achieves much higher resolution which makes even the isolated single particles can be clearly distinguished from surrounding matrix materials. Once more,

aggregation of the iron oxide particles in the materials was revealed, which is in good agreement with all the X-ray measurements. The clusters have similar size distribution as the previous results and lies in 1.4 to 3.3 microns, and most of them are between 2 and 3 microns.

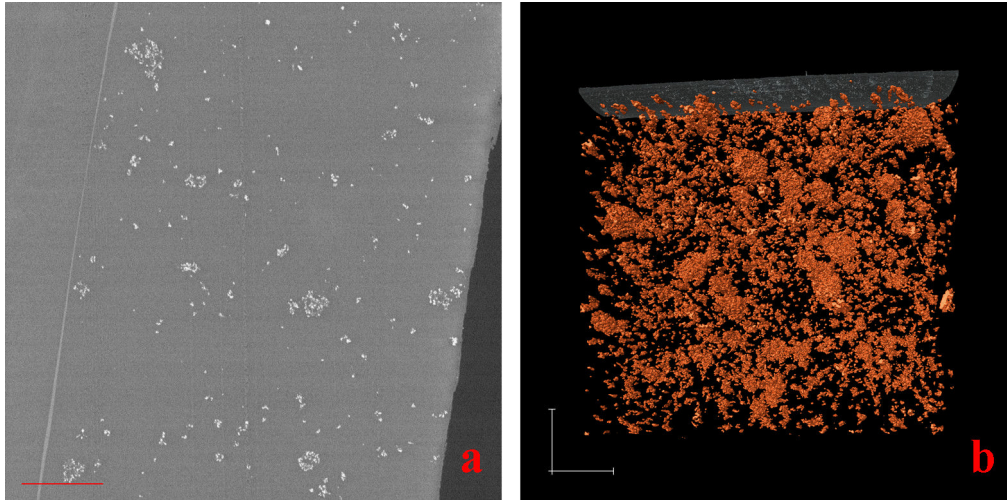


Figure 5. 8: Results of the 3 minute mixing iron oxide alkyd paint sample applied on PP plate from SBFSEM measurements. a, An SBFSEM section slice; b, Rendering of the acquired 3D volume of the sample, the transparent white layer on the top is the cyanoacrylate glue contacted with the sample surface, the orange parts are iron oxide particles. The scale bars are 5 microns.

## 5.6 Discussions

From figure 5.3, especially panels d, e and f of it, we can see that the X-ray holo-tomography measurement cannot well resolve the individual iron oxide particles from matrix resin, even collecting 2499 projections over 180° rotation for 3D reconstruction, while other techniques can resolve the particles in the matrix resin. This disadvantage of resolution probably is caused by the multiple sample-detector distance requirements of the measurement. Since the samples were moved to 4 different positions, rotated at each position, and were moved out and in the beam to collect background images, any mechanical errors from either the movement track or the rotation stage would reduce the resolution of the final results. Additionally, the recorded images were cut to the same size before they have been phase retrieved into projections, the potential inaccurate cutting could bring errors into the reconstruction and lower the quality of generated images.

With a routine 360 or 720 projection scan, both PXCT and TXM offer capabilities to distinguish iron oxide particles from alkyd resin. The reconstruction of cubic-shaped sample from PXCT measurement has apparent artefacts near four rectangle corners (see figure 5.5c), which are the four edges parallel to the rotation axis in the real sample. This should be caused by the sharp rectangle shape of the corners which produces extra X-ray scatterings from the edges and under-sampled phase changes near these regions. The later can also degrade the quality of reconstructed images. This could be alleviated by blunting the edges of specimens or even be eliminated by fabricating the samples into cylinder shape.

Instead of using 18 to 20 hours to measure one sample as in PXCT or X-ray holo-tomography experiments, TXM uses only about 4 hours to acquire adequate data for 3D reconstruction. However, the background subtracted projections (panels a, b & c in figures 5.6 and 5.7) from this method have considerable noise which would result in image quality and resolution degradation. It happened probably because the background/reference projections of TXM measurements were collected before or after the tomographic scan. This means the background subtracted from the whole serial of projections was the beam profile before or after the (long time) tomographic scan. Then the fluctuation of beam intensity would bring noise into the projections used for reconstruction via background subtraction. The influence of generated noise could be serious when the stability of X-ray source is poor and the target features are not strong X-ray absorption objects.

Compared with X-ray imaging techniques, SBFSEM provides much higher resolution. However, it is a destructive method because the diamond knife had direct physical contact with the imaging surfaces, which could potentially lead to deformation of shapes and movement of positions of features in the samples, such as the iron oxide particles here. Consequently, the 3D spatial structure of specimens could be artificially modified.

The results for the iron oxide alkyd paints from various methods verified and confirmed each other, which makes the sample quantity of the study more sufficient and the results more reliable and convincing. The increment of agitation time (before applying coating materials on substrates) was found here to improve the spatial distribution of iron oxide particles in matrix resin. The slightly better distribution status gained by the 3 minute mixing sample against the 1 minute mixing's may be simply just due to the 3 minute machine shaking as done on the job-site made the pigment particles dispersed better in the matrix resin than after 1 minute hand mixing. However, it is possible that the rather homogenous distribution of the iron oxide particles achieved in the 1 hour mixing sample could mainly derive from resistance of matrix material against the particles. Since during intensive machine agitation, the solvents of coating materials gradually volatilized, and after 1 hour treatment, the mixture would become more sticky and its viscosity could increase substantially. Then the resistance from the matrix resin against the iron oxide particles could significantly impede movement of the particles in the coating materials and prevent the aggregation phenomenon. From practical point of view, extending the agitation time to such as 10 minutes on job-site before applying the coating should be a useful recommendation as a trade-off between application time and dispersion of pigment particles. The formed clusters in measured samples seem to be no bigger than 4 microns and the majority of them are between 1.5 and 3 microns. The reasons why this happened are not clear, except for coating application methods, it should relate to properties of both iron oxide particles and alkyd resin.

## **5.7 Conclusions and Future Work**

The 3D spatial structure of the iron oxide alkyd paints was revealed by various imaging approaches including X-ray holo-tomography, ptychographic X-ray computed tomography (PXCT), transmission X-ray microscopy (TXM) and serial block-face scanning electron microscopy (SBFSEM). These methods verified each other and all of them were proven to be

efficient ways to investigate the structure of this classical pigment (particles)-matrix (resin) coating system. SBFSEM provides higher resolution than all X-ray imaging methods can achieve, and well resolves the individual particles from surrounding matrix resin. It is a qualified access to reveal 3D structure of the samples containing ultra-tiny features such as iron oxide particles here. The three X-ray techniques demonstrate similar capabilities of visualizing this neither typical phase(-contrast) specimen nor typical absorption(-contrast) specimen. However, TXM is a much faster method compared with the other two, and it is suitable for performing quicker 3D structure investigation. The two phase-sensitive X-ray imaging techniques, X-ray holo-tomography and PXCT, do not demonstrate advantages against TXM for studying this specific type of coating since it is not a typical phase object.

Clusters of the iron oxide particles were observed in both samples applied like on job-site, treated by 3 minute machine shaking, and samples experienced 1 minute hand mixing. The sizes of majority of clusters are ranging between 1.5 and 3 microns. The results of 1 hour mixing sample from X-ray imaging present that homogenous spatial distribution of pigment particles can be achieved, at least, by extending the agitation time to as long as 1 hour here before applying the coating materials on substrates. At the same time, increasing the agitation time leads to a lower clustering level of iron oxide particles in cured coating films.

Further quantitative analysis of volumes, volume concentrations, shapes and correlations of iron oxide particle clusters such as spatial distances among each cluster should be performed in future. The light scattering properties of the cured coating film could be calculated or simulated based on the 3D spatial structures acquired. More specific and detailed experiments on measuring pigment particle spatial distribution of the samples experienced different agitation time can be carried out to establish more reliable and clear relation between these two.

## References

- [1] Reddy, V.A., Sampathkumaran, P.S. & Gedam, P.H. Effect of oil length of alkyd on the physical-chemical of its coatings. *Prog. Org. Coat.* **14**, 87-97 (1986).
- [2] Gündüz, G., Kisakürek, D., & Kayadan, S. Flame retardant alkyd paint. *Polym. Degrad. Stabil.* **64**, 501-504 (1999).
- [3] Chico, B. *et al.* Anticorrosive behaviour of alkyd paints formulated with ion-exchange pigments. *Prog. Org. Coat.* **61**, 283-290 (2008).
- [4] Hofland, A. Alkyd resins: From down and out to alive and kicking. *Prog. Org. Coat.* **73**, 274-282 (2012).
- [5] van Gorkum, R. Manganese Complexes as Drying Catalysts for Alkyd Paints, 2005; Doctoral thesis, Leiden University, Leiden, Netherlands.
- [6] Cloetens, P. *et al.* Holotomography: Quantitative phase tomography with micrometer resolution using hard synchrotron radiation x rays. *Appl. Phys. Lett.* **75**, 2912-2914 (1999).
- [7] Cloetens, P., Mache, R., Schlenker, M. & Lerbs-Mache, S. Quantitative phase tomography of Arabidopsis seeds reveals intercellular void network. *Proc. Natl Acad. Sci. USA* **103**, 14626-14630 (2006).
- [8] Dierolf, M. *et al.* Ptychographic X-ray computed tomography at the nanoscale. *Nature* **467**, 436-439 (2010).
- [9] Guizar-Sicairos, M. *et al.* Phase tomography from x-ray coherent diffractive imaging projections. *Opt. Express* **19**, 21345-21357 (2011).
- [10] Glenn, W. V., Jr., Johnston, R. J., Morton, P. E. & Dwyer, S. J. Image generation and display techniques for CT scan data-Thin transverse and reconstructed coronal and sagittal planes. *Invest. Radiol.* **10**, 403-416 (1975).
- [11] Kak, A. C. & Slaney M., *Principles of Computerized Tomographic Imaging* (Society of Industrial and Applied Mathematics, Philadelphia, PA, 2001).

- [12] Denk, W. & Horstmann, H. Serial block-face scanning electron microscopy to reconstruct three-dimensional tissue nanostructure. *PLoS Biol.* **2**, e329 (2004).
- [13] Müller-Reichert, T., Mancuso, J., Lich, B. & McDonald, K. Three-dimensional reconstruction methods for *caenorhabditis elegans* ultrastructure. *Methods Cell Biol.* **96**, 331-361 (2010).
- [14] Mokso, R., Cloetens, P., Maire, E., Ludwig, W. & Buffière, J. Nanoscale zoom tomography with hard x rays using Kirkpatrick-Baez optics. *Appl. Phys. Lett.* **90**, 144104 (2007).
- [15] Bleuet, P. *et al.* A hard x-ray nanoprobe for scanning and projection nanotomography. *Rev. Sci. Instrum.* **80**, 056101 (2009).
- [16] Dierolf, M. *et al.* Ptychographic coherent diffractive imaging of weakly scattering specimens. *N. J. Phys.* **12**, 035017 (2010).
- [17] Thibault, P. *et al.* High-resolution scanning X-ray diffraction microscopy. *Science.* **321**, 379-382 (2008).

## **Chapter 6**

### **Three-Dimensional Structure and Percolation Properties of a Barrier Marine Coating**

This chapter is based on a paper submitted to Nature Communications titled as “Three-Dimensional Structure and Percolation Properties of a Barrier Marine Coating” with the co-authors: Manuel Guizar-Sicairos, Gang Xiong, Laura Shemilt, Ana Diaz, John Nutter, Nicolas Burdet, Suguo Huo, Joel Mancuso, Alexander Monteith, Frank Vergeer, Andrew Burgess and Ian Robinson. The figures and text in the paper were prepared by myself in correspondence with all these authors. Ptychographic X-ray computed tomographic reconstruction was performed by Manuel Guizar-Sicairos. 3D image segmentation, presentation and quantitative analysis were done by myself using Avizo. I also provided the data for finite element simulation and carried out the simulation with Gang Xiong and John Nutter.

In this chapter, we revealed three-dimensional (3D) structures of an aluminium epoxy barrier marine coating by both scanning coherent X-ray diffraction imaging technique and scanning

electron microscopy method. The shapes and spatial arrangement of the aluminium flakes were demonstrated, and the sizes and orientations of the flakes were quantitatively analysed. Using the obtained real 3D spatial structures, the finite element simulation of the percolation properties of the coating was performed.

## **6.1 Introduction**

Artificially structured coatings are widely employed to minimize materials deterioration and corrosion [1, 2], the annual direct cost of which is over 3% of the gross domestic product (GDP) for industrial countries [3]. Barrier coatings, an essential branch of the corrosion-resistant coating family, are deliberately structured to operate in extremely aggressive environments such as seawater [4-6]. Among these coatings, the aluminium flake pigmented coating demonstrates outstanding anticorrosive performance [4]. However, three-dimensional (3D) structures of coatings [7, 8], which dominate their performance, have not been investigated in detail. Here we present, at nano-scale, a quantitative analysis of 3D spatial structures of an aluminium epoxy barrier marine coating obtained by serial block-face scanning electron microscopy (SBFSEM) [9] and ptychographic X-ray computed tomography (PXCT) [10, 11]. We then demonstrate how percolation impedes ion diffusion in the materials using finite element simulations based on the actual 3D structures instead of using modelling structures [12]. We find the aluminium flakes align within  $15^\circ$  of the coating surface in the material, causing the perpendicular diffusion resistance of the coating to be substantially higher than the pure epoxy. Combining high-resolution measurement and simulation in three-dimensions, our work provides a way of investigating, analysing and understanding the structures and properties of coatings, which can reduce their product research and development time. We expect such an approach can be of wider use in nano-scale materials and biological sciences.

Aluminium epoxy coatings are widely applied to protect steel structures such as ocean-going vessels because of their excellent anticorrosive performance, as determined by the coating barrier properties [5]. The shape and spatial distribution of the aluminium flakes, usually several microns wide and a few hundred nanometres thick, added to the materials significantly improve the barrier properties of the coating by decreasing the transport rate of corrosive substances such as ions, water (vapour) and oxygen through coating films [4, 5, 13]. Additionally, the aluminium can react with the hydroxide ions produced at the cathode in the corrosion cell, reducing the pH at the coating-steel interface and decreasing the rate of cathodic disbondment [14]. Meanwhile, the epoxy resin gives the coating film abrasion resistance and functions as a corrosion inhibitor for the aluminium flakes [15]. However, the 3D nano-structure of the coatings has not been accessed in detail before.

## **6.2 Experiments**

Here we studied an anticorrosive aluminium epoxy barrier marine coating, which is mainly composed of aluminium flakes, talc fragments, iron oxide particles and epoxy resin (matrix material). Both aluminium flakes and talc fragments work as barriers when they align parallel to the coating surface. In commercial products, talc fragments substitute for aluminium flakes to reduce risk of electrical sparking and costs. The iron oxide particles are added to produce the desired colour and to improve solvent and chemical resistance of the products [16]. SBFSEM and PXCT were employed for the purpose, after we found that full-field transmission X-ray microscopy using both laboratory and synchrotron sources could not reveal the contrast between the various internal structures of the material (see figure 6.1).

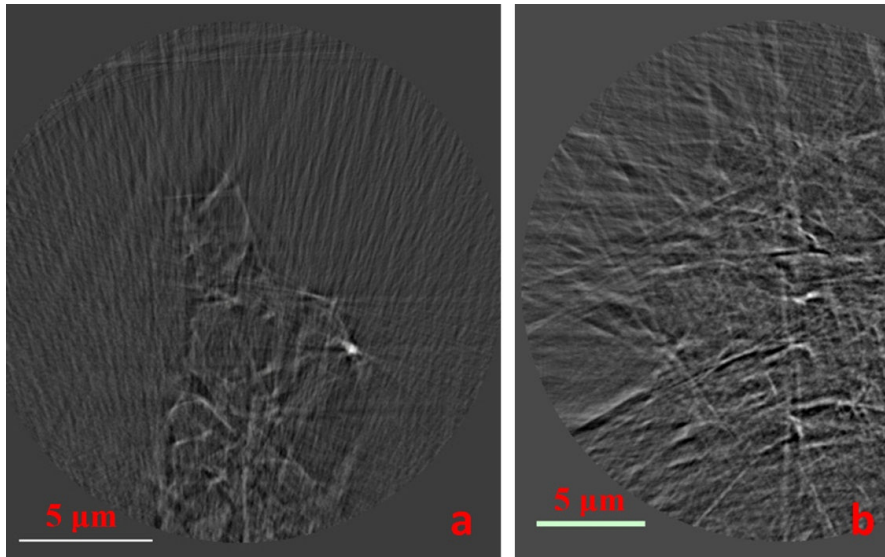


Figure 6. 1: Results of the aluminium epoxy barrier marine coating from transmission X-ray microscopy (TXM). a & b, A single tomogram slice perpendicular to the rotation axis from the degassed and non-degassed coating samples, respectively. The samples were measured by the full-field TXM using X-rays of a photon energy of 8.0 keV at the beamline 32ID-C, Advanced Photon Source, Argonne National Laboratory, Argonne, IL, USA.

SBFSEM was used to image a sample which was degassed in vacuum, a procedure that could lead to potential improvements of coating technology, and then cured at 100°C for an hour. SBFSEM is a serial sectioning imaging method [9, 17, 18] originally developed for 3D spatial structure investigation of biological specimens [19-21], from ultrathin section sample preparation for transmission electron microscopy (TEM) [22]. It acquires a continuous series of parallel images of fresh surfaces created by mechanical cuts made by a diamond knife installed in an ultramicrotome [9]. Three-dimensional (3D) images of samples are then generated by stacking the corresponding series of images together.

For the SBFSEM measurements, the degassed aluminium epoxy barrier marine coating film was mounted on an aluminium specimen pin (Gatan, Inc.) using cyanoacrylate glue. The coating surface was placed perpendicular to the axis of the pin. The sample was then trimmed down by a microtome to create a block face sizes approximately  $500\ \mu\text{m} \times 500\ \mu\text{m}$ . After that, it was measured by the SBFSEM system, installed in an environmental SEM and operated at

2.5 kV with 0.4 Torr chamber pressure in a water vapour environment. The BSE signals from the sample were acquired with 10  $\mu$ s dwell time per pixel of size 30 nm  $\times$  30 nm, at a working distance of 5.8 mm. The sectioning thickness was 30nm per slice with a cutting speed 22s per slice. Altogether 200 slice images (6  $\mu$ m thick) with a field of view 30.7  $\mu$ m  $\times$  30.7  $\mu$ m were obtained.

A degassed and a non-degassed sample of the same material were imaged by PXCT which combines scanning coherent X-ray diffractive imaging [23, 24] with computed tomography [25, 26]. Both samples were first cut to size using a focused ion beam (FIB) tool. A tomographic projection at each rotation angle of was reconstructed from multiple X-ray diffraction patterns using a difference-map phase-retrieval algorithm [24]. PXCT produces quantitative 3D images of customised field of view with a representation of the average electron density per voxel [10, 27]. It avoids mechanical sample destruction and possible cutting artefacts which, in certain cases, can be detrimental to nano- and micro-scale sciences.

PXCT experiments were performed at the cSAXS beamline (X12SA) of the Swiss Light Source, Paul Scherrer Institut, using X-rays of photon energy 6.2 keV. FIB fabricated cubic-shaped coating samples were measured. X-ray diffraction patterns in the transmission geometry were recorded by a PILATUS photon-counting detector (pixel size 172  $\mu$ m  $\times$  172  $\mu$ m), placed 7.2 meters downstream of the samples. During the measurements, the samples were rotated 180° with 0.5° intervals, obtaining projections of the samples at 360 orientations. At each orientation angle, the samples were scanned along circular shells with a 1.4  $\mu$ m radial step in a plane perpendicular to the X-ray beam to cover a field of view extending beyond the sample edges. The projections were reconstructed by the difference map algorithm [24], then post-processed, aligned, combined and reconstructed to form a 3D volume according to the procedure described in reference [11].

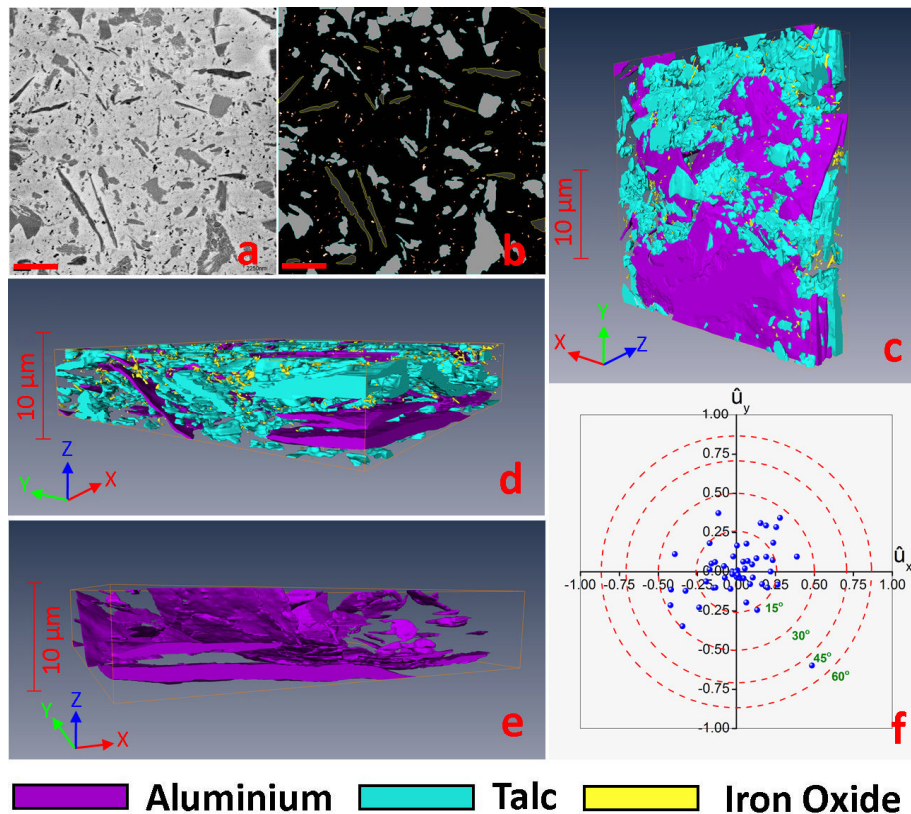


Figure 6. 2: Results for the degassed aluminium epoxy marine coating imaged by SBFSEM. a, An SBFSEM single slice; b, Segmented result from figure 1a; c & d, Rendering of 3D spatial structure image of the coating; e, A 3D image of just the aluminium flakes in the coating. f, Quantitative orientation analysis of the aluminium flakes in the coating material. Deviation projections of individual flakes are plotted stereographically around the surface direction (centre). Dash circles denote net 15°, 30°, 45° and 60° deviations from parallel alignment to the surface. The scale bars in a and b are 5 microns.

### 6.3 Results and Discussion

Figure 6.2a is a contrast-reversed back scattering electron (BSE) image of the degassed aluminium epoxy barrier marine coating from the SBFSEM measurement. Flake-shaped dark objects, grey objects and small black dots in it were identified as aluminium flakes, talc fragments and iron oxide particles, respectively, as segmented by commercial software “Avizo” and shown in figure 6.2b as dark-grey objects, light-grey objects and bright small spots. The remaining parts of figures 6.2a and 6.2b were attributed to epoxy resin. This segmentation was validated by the quantitative values of electron density obtained with PXCT, as discussed below. The 3D spatial arrangement of aluminium flakes within the

material is illustrated in figure 6.2e, in which we can see a parallel arrangement of the aluminium flakes that cannot be observed in 2D slice images.

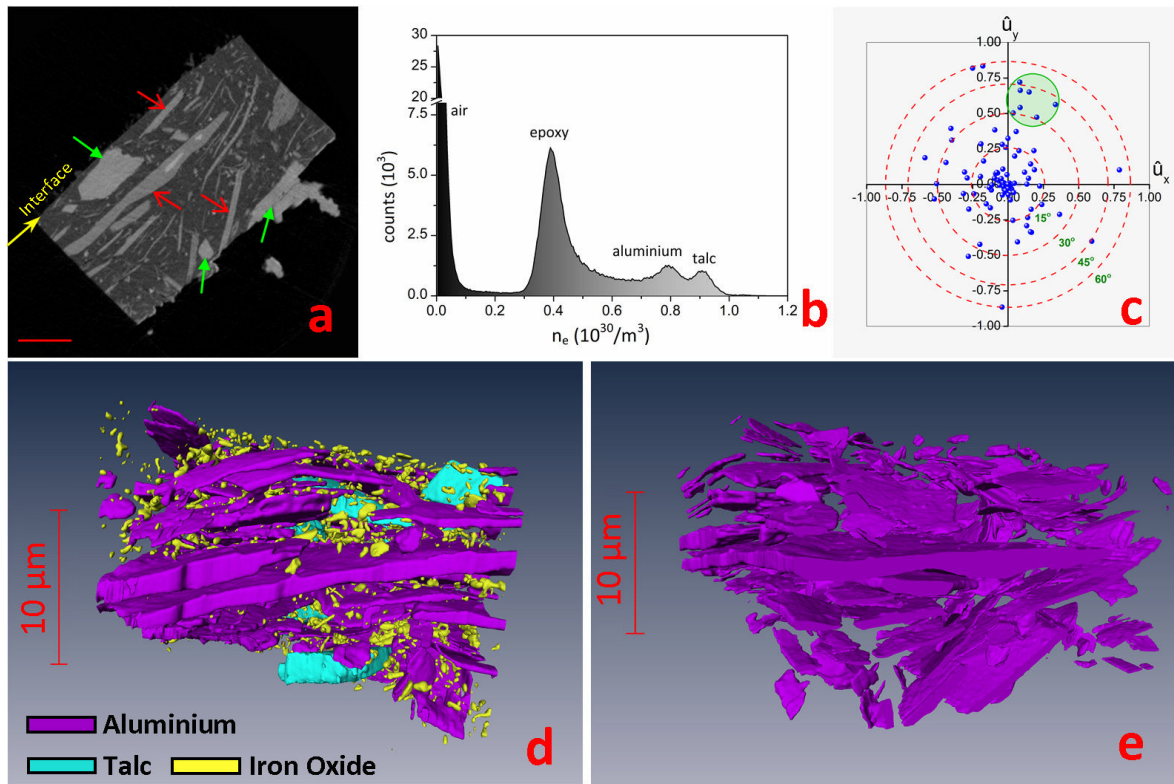


Figure 6. 3: Results for the degassed coating imaged by PXCT. a, A single tomogram slice perpendicular to the rotation axis. Arrows point to some of the identified aluminium flakes in red and talc fragments in green. The scale bar is 5 microns. b, Histogram of electron density distribution of the tomogram slice in figure 6.3a. c, Quantitative orientation analysis of the aluminium flakes, plotted in the same way as figure 6.2f. d, Rendering of 3D spatial structure image of the sample. e, 3D spatial arrangement image of just the aluminium flakes in the material.

Figure 6.3a presents a single reconstructed tomogram slice of a different piece of the same degassed sample obtained by the PXCT measurement. Here, the electron density is determined accurately enough for the components to be easily identified by the respective peaks of the density histogram, shown in figure 6.3b. The long, slim grey objects with electron density  $0.793 \times 10^{30}/\text{m}^3$  are identified as aluminium flakes, the slightly brighter grey objects with electron density  $0.905 \times 10^{30}/\text{m}^3$  are talc fragments, the small dots are iron oxide

particles, the other grey parts are epoxy resin and the black regions are surrounding air. Upon conversion [27], the aluminium and talc mass densities are measured to be  $2.73 \times 10^3 \text{ kg/m}^3$  and  $3.00 \times 10^3 \text{ kg/m}^3$ , compared with  $2.70 \times 10^3 \text{ kg/m}^3$  and  $2.78 \times 10^3 \text{ kg/m}^3$  from standard tables. The high contrast and boundary well-defined features generated in the tomogram slices enable their direct 3D segmentation into spatial volume regions. Figures 6.3d and 6.3e are 3D renderings after segmentation, analogous to figures 6.2d and 6.2e, again presenting the parallel alignment of the aluminium flakes distinctly. PXCT demonstrates here its combined advantages of ptychography, a phase-sensitive imaging technique, and X-ray computed tomography.

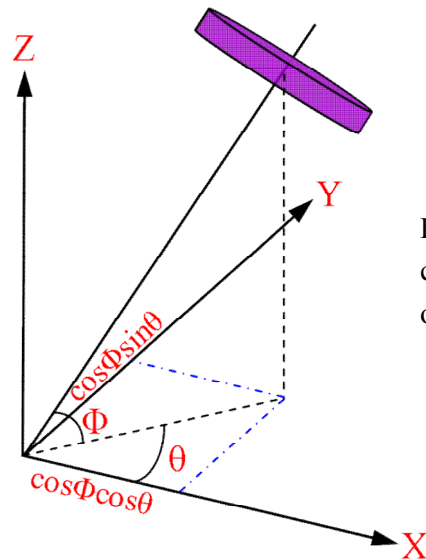


Figure 6. 4: Geometry of 3D coordination system (used in orientation quantitative analysis).

According to the sample mounting geometry described in “Experiments” part, the xy plane in figures 6.2c, d and e is parallel to the sample surface. The coating-steel interface in figure 6.3a, which is labelled and made parallel to the xy plane, is assumed to be parallel to the sample surface. The surface normal direction of each aluminium flake is defined as the orientation of its major principal inertia axis which is along the shortest geometrical axis of the object. It is given as the eigenvector of the largest eigenvalue of the inertia matrix describing the voxel distribution in each identified flake. The angle between the coating

surface normal direction and the xy plane is named as  $\Phi$  (see figure 6.4) and given in degrees. The resulting  $\Phi$  falls between  $0^\circ$  and  $90^\circ$ . Therefore, the orientation deviation of aluminium flakes from surface parallel alignment is  $(90^\circ - \Phi)$ . The angle between the projection of the surface normal direction on the xy plane and the x axis is named as  $\theta$  (see figure 6.4, given in degrees). It falls between  $-180^\circ$  and  $180^\circ$ . Both  $\Phi$  and  $\theta$  values are computed based on the segmented 3D images (see a subset of the values in tables 6.1 and 6.2).

The x and y components of the unit vector of the projection of surface normal direction on the xy plane,  $\hat{u}_x$  and  $\hat{u}_y$ , respectively, are plotted stereographically around the surface direction ( $\Phi = 90^\circ$ , in the centre). Here,  $\hat{u}_x = \cos\Phi\cos\theta$ ,  $\hat{u}_y = \cos\Phi\sin\theta$ . This means an aluminium flake has an orientation deviation  $(90^\circ - \Phi)$  from the surface parallel direction will be projected on a circle of radius equals  $\sin(90^\circ - \Phi) = \cos\Phi$  with the centre at the surface direction ( $\Phi = 90^\circ$ ,  $\hat{u}_x = 0$  and  $\hat{u}_y = 0$ ) in the plotting map (figures 6.2f and 6.3c).

After the quantitative orientation analysis, we found that the aluminium flakes arrange nearly parallel to the coating sample surfaces, mostly within  $15^\circ$  deviation, as shown in the orientation stereograms in figures 6.2f and 6.3c. A group of misoriented flakes, having around  $40^\circ$  deviation, is highlighted by a green circle in figure 6.3c. These flakes form a physical cluster lying next to each other in the material, as can be observed in the top-right of figure 6.3a or the lower-right part of figure 6.3e.

In addition, the lengths and volumes of individual objects in the materials can be obtained from morphometric analysis after the 3D image segmentation. Thus, the size of each object and the pigment volume concentration (PVC), one of the most crucial formulating parameters of coating products, of the applied and in-service coatings can be revealed. These parameters of the aluminium flakes are tabulated and presented in tables 6.1 and 6.2.

Table 6. 1: The volumes, lengths, orientation angles  $\Phi$  and  $\theta$  of the 30 largest identified aluminium flakes in the degassed coating sample measured by SBFSEM.

Volume ( $\mu\text{m}^3$ )	Length ( $\mu\text{m}$ )	Orientation Angle $\Phi$ ( $^\circ$ )	Orientation Angle $\theta$ ( $^\circ$ )
101.50	21.726	77.667	26.412
16.121	13.792	75.583	133.24
8.1003	10.772	80.110	175.40
5.1303	9.6756	69.496	57.120
4.9868	9.3547	84.990	155.50
1.9286	8.8095	89.498	31.783
4.9194	8.3548	86.751	-47.971
2.7123	6.7518	88.569	-154.84
1.5623	5.6664	84.214	42.980
1.3670	5.6107	79.670	-145.00
3.7242	5.3066	86.396	-42.527
4.2662	5.1946	64.325	-164.72
2.0583	4.8340	61.742	-153.14
1.7465	4.4687	78.230	-162.46
0.95934	4.4598	85.256	-152.12
0.42998	3.9900	88.437	176.45
0.78991	3.9591	63.697	50.870
1.1314	3.9215	89.365	49.797
0.47277	3.7500	66.412	13.818
0.51602	3.7383	75.791	17.568
0.73534	3.5863	69.729	63.381
1.0956	3.5490	83.638	24.793
1.0481	3.5357	39.719	-50.980
1.0595	3.3482	81.127	33.525
0.63248	3.3232	88.053	-85.270
1.0408	3.1676	77.328	0.20928
0.44520	3.1586	83.196	-41.767
0.40724	3.1006	73.906	-17.418
0.54691	3.0725	73.859	-61.143
0.95502	3.0320	65.791	164.09

Table 6. 2: The volumes, lengths, orientation angles  $\Phi$  and  $\theta$  of the 30 largest identified aluminium flakes in the degassed coating sample measured by PXCT.

Volume ( $\mu\text{m}^3$ )	Length ( $\mu\text{m}$ )	Orientation Angle $\Phi$ ( $^\circ$ )	Orientation Angle $\theta$ ( $^\circ$ )
220.72	24.816	83.789	132.55
60.308	14.915	86.074	95.633
25.128	14.053	87.452	-126.11
36.320	13.347	87.557	-51.974
6.7046	11.806	59.704	85.786
0.088684	9.6620	90.000	10.064
15.245	8.8182	31.451	102.01
8.6395	8.6697	73.800	-30.670
11.486	8.5687	76.142	-46.942
5.2899	8.1575	86.754	-105.86
2.6169	7.6256	89.873	-156.96
7.2961	7.5576	69.982	123.73
9.4540	7.4712	77.693	28.896
5.3567	7.3497	67.834	81.070
11.769	7.2369	72.496	52.333
4.9297	6.5755	77.571	41.831
7.6449	5.9777	75.484	-164.50
4.9661	5.3991	82.341	0.98285
4.1692	5.2455	73.040	171.23
3.6090	4.9527	89.201	40.187
1.8946	4.9320	55.680	135.65
2.0809	4.8966	83.362	138.98
2.1960	4.8756	89.454	-166.37
3.5022	4.7089	67.872	-63.770
1.1955	4.6012	44.310	-34.006
1.2935	4.5378	78.188	76.415
1.0631	4.4887	62.172	-115.22
1.6056	4.3584	81.312	16.548
0.31028	4.2144	90.000	70.979
3.2317	4.1646	88.480	161.48

Among these measurements, the length of an object is defined as its maximum Feret diameter measured over 31 orientations, namely, at 31 couples of  $\Phi$  and  $\theta$  angles described above.

Here, the  $\Phi$  and  $\theta$  are (orientation) angles used for measurement, not the orientation angles of the objects themselves. The  $\theta$  contains 10 values:  $0^\circ$ ,  $18^\circ$ ,  $36^\circ$ ,  $54^\circ$ ,  $72^\circ$ ,  $90^\circ$ ,  $108^\circ$ ,  $126^\circ$ ,  $144^\circ$  and  $162^\circ$ , every  $18^\circ$  in the  $[0^\circ, 180^\circ]$  interval.

An interesting discovery in the non-degassed aluminium epoxy marine coating is that the aluminium flakes tend to follow the edges of nearby air pores, as seen in figure 6.5. This correlation in structure has not been observed before and it is different from the common expectation that the aluminium flakes should be parallel to the external coating surface. This may be due to a surface alignment effect at the edges of air pores which is similar to that at the external coating surface, which is caused by solvent evaporation during the drying process [16]. This co-localised structure may be responsible for the strong barrier function against corrosive substances in the pores, which are presumably the penetration point for external agents and which provide space for accumulation of corrosive substances. However, this structure has the potential hazard that, once the aluminium flakes become eroded, the anticorrosive performance/protective capability of the coating would suddenly diminish because of decomposition of the barriers.

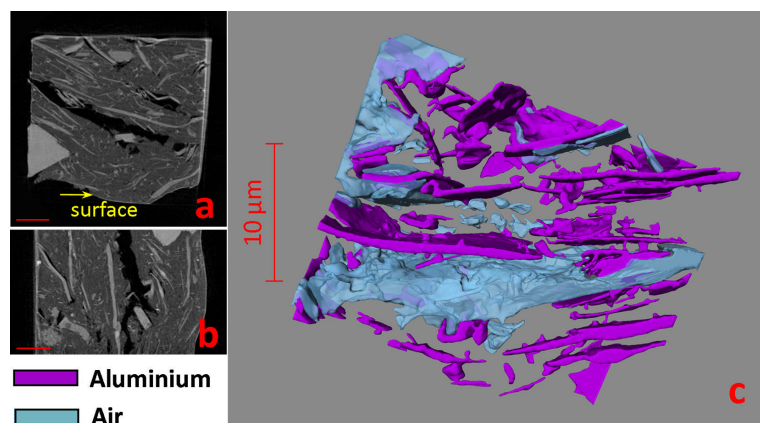


Figure 6. 5: Results for the non-degassed aluminium epoxy marine coating from PXCT measurement. a & b, Tomogram slices perpendicular and parallel to the rotation axis through the reconstructed 3D volume, respectively. c, Rendering of 3D spatial arrangement of aluminium flakes and air pores in the sample. The scale bars in a and b are 5 microns.

Simulations of the percolation properties of the coating were performed using COMSOL “MultiPhysics” software package, based on the actual, segmented 3D spatial structures. We determined the ion diffusion process in the coating films, which is regarded as the rate-determining process governing the cathodic delamination of coatings from steel and its corrosion [5]. The simulations were done by calculating electric conductivity  $\sigma$  in the materials following Ohm's law ‘ $J = -\sigma \nabla V$ ’ which has the same mathematical form as Fick's first law ‘ $J = -D \nabla C$ ’ that can describe diffusion in 3D systems when the concentration of the diffusing species can be assumed to remain constant.  $J$  is the current density or (ion) diffusion flux,  $\nabla V$  is the potential gradient (locally the potential difference,  $V$ , divided by the conductor length),  $D$  is the diffusion coefficient and  $\nabla C$  is the concentration gradient. The ion diffusion and electric conduction are also relevant because both ions and electrons are charged particles and the potential difference is a driving force for ion transport during the electrochemical process of steel corrosion. The electric conductivities were calculated along the directions perpendicular and parallel to the coating surface directions to determine the material's diffusion coefficient anisotropy  $R = \sigma_{\text{perpendicular}} / \sigma_{\text{parallel}}$ .

Figures 6.6a, c and d present the simulation results as streamlines of flow, which are the paths followed by ions from one side to the other of the coating films during diffusion. The ions flow along surfaces of objects and go around the obstructions in the structures, which clearly reveals the barrier properties of aluminium flakes against ions. This validates, with direct evidence, the pictorial matrix models of barrier coatings found in the literature [28]. The current density map (figure 6.6b) illustrates the ions have much higher concentrations at the edges of flakes which could potentially become the points that corrosion starts. It may be worth applying extra protective treatment to the edges of the aluminium flakes.

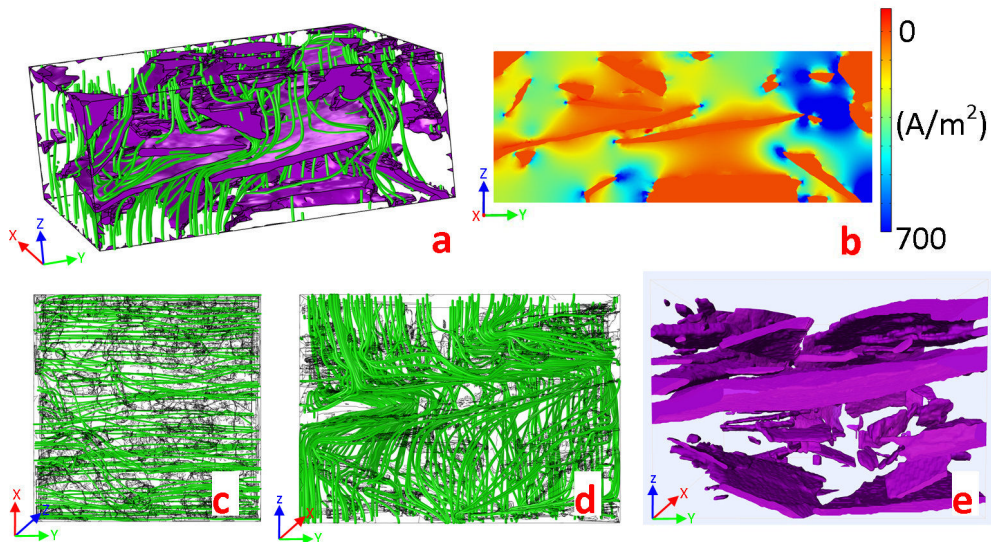


Figure 6. 6: Finite element simulation results based on the actual 3D spatial structures of the coating measured in this study. a, Simulated flow along the direction perpendicular to the coating surface presented as streamlines within the real structure obtained from the SBFSEM measurement. b, A slice cut of the current density map generated from simulation in panel a. c & d, Simulated flow along the directions parallel and perpendicular to the coating surface of the structure obtained by PXCT. e, Rendering of the 3D volume of the coating structure used for simulations in panels c and d.

The simulation based on the SBFSEM structure (figure 6.6a), 6 microns thick, shows the diffusion coefficient anisotropy to be  $R=0.516$ . The 10 microns thick structure obtained from PXCT (figure 6.6e) gave  $R=0.358$ . The smaller anisotropy ratio acquired in the latter case could be caused by a single big aluminium flake in the structure (see figure 6.6e) which occupies the majority area of the cross-section and blocks the transport routes of ions more drastically. Therefore, trying to avoid breaking aluminium flakes either during manufacture or application process would contribute to improving the final performance of the coating films. Considering the not-quite parallel alignment of the aluminium flakes to the coating surface, we could expect that pure epoxy would give higher ion diffusion coefficient and smaller anisotropy ratio value against the surface perpendicular direction. This illustrates that the diffusion rate of ions across the aluminium flakes pigmented coating is heavily reduced compared with pure epoxy.

## 6.4 Conclusions

The morphological analysis of 3D spatial structures and the simulations performed on the aluminium epoxy barrier marine coating reveal the relations between the structure of the coating and its properties. The results from SBFSEM and PXCT validated each other and both methods were proved to be effective ways to measure 3D spatial structures of complex industrial specimens. PXCT is found to be especially powerful as it shows the ability to distinguish the four components in the material quantitatively by electron density. By taking measured 3D structures into detailed simulations, we have demonstrated an approach for validating mechanistic assumptions and potentially provide a practical method to engineer the efficacy of anti-corrosion coatings by modelling electrochemical process in materials based on the actual structures. This could be used to evaluate the performance of materials, and shorten the product research and development lifetime, compared with carrying out endurance studies of original specimens, which can take years. We found that the degassed specimens have more compact structure comparing with the non-degassed one prepared by conventional coating technology, which means the former would provide better anti-corrosion properties. The degassing treatment could be used to enhance coating performance and thus to further reduce the risk of steel construction failures such as oil tanker break-ups.

## References

- [1] Walter, G. W. A critical review of the protection of metals by paints. *Corros. Sci.* **26**, 27-38 (1986).
- [2] Shreir, L. L., Jarman, R.A. & Burstein, G.T. (Eds.) *Corrosion* (3rd ed.): Chap. 14 (Butterworth-Heinemann Ltd., Oxford-London, 1994).

- [3] Schmitt, G. *et al.* Global Needs for Knowledge Dissemination, Research, and Development in Materials Deterioration and Corrosion Control. Whitepaper of the World Corrosion Organization (2009).
- [4] Biegańska, B., Zubielewicz, M. & Smieszek, E. Influence of barrier pigments on the performance of protective organic coatings. *Prog. Org. Coat.* **16**, 219-229 (1988).
- [5] Thomas, N. L. The barrier properties of paint coatings. *Prog. Org. Coat.* **19**, 101-121 (1991).
- [6] Moggridge, G. D., Lape, N. K., Yang C. & Cussler, E. L. Barrier films using flakes and reactive additives. *Prog. Org. Coat.* **46**, 231-240 (2003).
- [7] Jaeggi, C., Mooser, R., Frauchiger, V. & Wyss, P. 3D characterization of open porous vacuum plasma sprayed titanium coatings by means of high resolution micro computer tomography. *Mater. Lett.* **63**, 2643-2645 (2009).
- [8] Koller, D.M., Hanneschläger, G., Leitner, M. & Khinast, J.G. Non-destructive analysis of tablet coatings with optical coherence tomography. *Eur. J. Pharm. Sci.* **44**, 142-148 (2011).
- [9] Denk, W. & Horstmann, H. Serial block-face scanning electron microscopy to reconstruct three-dimensional tissue nanostructure. *PLoS Biol.* **2**, e329 (2004).
- [10] Dierolf, M. *et al.* Ptychographic X-ray computed tomography at the nanoscale. *Nature* **467**, 436-439 (2010).
- [11] Guizar-Sicairos, M. *et al.* Phase tomography from x-ray coherent diffractive imaging projections. *Opt. Express* **19**, 21345-21357 (2011).
- [12] Alam, P., Byholm, T., Kniivilä, J., Sinervo, L. & Toivakka, M. Calculating the permeability of model paper coating structures comprising incongruent particle shapes and sizes. *Micropor. Mesopor. Mat.* **117**, 685-688 (2009).
- [13] Yang, C., Smyrl, W. H. & Cussler, E. L. Flake alignment in composite coatings. *J. Membrane Sci.* **231**, 1-12 (2004).

- [14] Leidheiser, H., JR., Wang, W. & Igetoft, L. The mechanism for the cathodic delamination of organic coatings from a metal surface. *Prog. Org. Coat.* **11**, 19-40 (1983).
- [15] Müller, B. & Fischer, S. Epoxy ester resins as corrosion inhibitors for aluminium and zinc pigments. *Corros. Sci.* **48**, 2406–2416 (2006).
- [16] Lambourne, R. & Strivens, T. A. *Paint and Surface Coatings-Theory and Practice* (2nd ed.): 91-165 (Woodhead Publishing Ltd., Cambridge, England, 1999).
- [17] Levinthal, C. & Ware, R. Three dimensional reconstruction from serial sections. *Nature* **236**, 207-210 (1972).
- [18] Arenkiel, B. R. & Ehlers, M. D. Molecular genetics and imaging technologies for circuit-based neuroanatomy. *Nature* **461**, 900-907 (2009).
- [19] Rouquette, J. *et al.* Revealing the high-resolution three-dimensional network of chromatin and interchromatin space: A novel electron-microscopic approach to reconstructing nuclear architecture. *Chromosome Res.* **17**, 801-810 (2009).
- [20] Müller-Reichert, T., Mancuso, J., Lich, B. & McDonald, K. Three-dimensional reconstruction methods for caenorhabditis elegans ultrastructure. *Methods Cell Biol.* **96**, 331-361 (2010).
- [21] Briggman, K. L., Helmstaedter, M. & Denk, W. Wiring specificity in the direction-selectivity circuit of the retina. *Nature* **471**, 183-188 (2011).
- [22] O'Brien, H. C. & McKinley, G. M. New microtome and sectioning method for electron microscopy. *Science* **98**, 455-456 (1943).
- [23] Rodenburg, J. M. *et al.* Hard-X-Ray lensless imaging of extended objects. *Phys. Rev. Lett.* **98**, 034801 (2007).
- [24] Thibault, P. *et al.* High-resolution scanning X-ray diffraction microscopy. *Science* **321**, 379 -382 (2008).

[25] Glenn, W. V., Jr., Johnston, R. J., Morton, P. E. & Dwyer, S. J. Image generation and display techniques for CT scan data-Thin transverse and reconstructed coronal and sagittal planes. *Invest. Radiol.* **10**, 403-416 (1975).

[26] Kak, A. C. & Slaney M., *Principles of Computerized Tomographic Imaging* (Society of Industrial and Applied Mathematics, Philadelphia, PA, 2001).

[27] Diaz A. *et al.* Quantitative x-ray phase nanotomography. *Phys. Rev. B* **85**, 020104(R) (2012).

[28] Zaarei, D., Sarabi, A. A., Sharif, F. & Kassiriha, S. M. Structure, properties and corrosion resistivity of polymeric nanocomposite coatings based on layered silicates. *J. Coat. Technol. Res.* **5**, 241-249 (2008).

#### **Author contributions of the submitted paper**

I.R., B.C., F.V. and A.B. conceived the project. J.M. and A. M. carried out the SBFSEM measurements. B.C. analysed the SBFSEM result. B.C., S.H., F.V. and A.B. prepared samples for PXCT experiments. B.C., M.G., L.S., A.D. and N.B. carried out the PXCT experiments. B.C. and M.G. analysed the PXCT results. G.X., J.N. and B.C. carried out the COMSOL simulation. All authors contributed to interpreting the results and writing the manuscript.

## **Chapter 7**

### **Conclusions and Future Work**

#### **7.1 Conclusions**

The work demonstrated in the dissertation is the first systematic research of three-dimensional (3D) spatial structures of coatings. This dissertation presented the 3D spatial structures of three varieties of coating specimens: silver epoxy adhesive, iron oxide alkyd paint and aluminium epoxy marine coating by using different 3D imaging methods. The shapes and spatial distributions of particles of the main functional ingredients of all these coating specimens were demonstrated. The research on the aluminium epoxy marine coating goes beyond 3D (quantitative) characterization of the aluminium flakes in the coating, such as shapes, sizes, volumes, orientations and spatial distributions and correlations of the target objects. By importing the measured 3D structures of the aluminium epoxy marine coating samples into detailed simulations, we have presented an approach for validating mechanistic assumptions on them and potentially provide a practical method to engineer the efficacy of anti-corrosion coatings by modelling electrochemical process in materials based on the actual structures. This could be used to evaluate the performance of materials, and shorten the industrial product research and development lifetime, compared with carrying out endurance studies of original specimens.

The transmission X-ray microscopy (TXM), ptychographic X-ray computed tomography (PXCT), X-ray holo-tomography and serial block-face scanning electron microscopy (SBFSEM) had been verified can be effective ways to reveal 3D spatial structures of complex industrial specimens. Among these methods, the TXM was proved to be good at measuring amplitude samples whose components have big difference of X-ray absorption capabilities. The PXCT presented especially strong power to reveal structures of complex phase objects such as aluminium epoxy marine coating whose components have similar X-ray absorption capabilities. X-ray holo-tomography has relatively simple experimental set-up, and has the same capabilities as PXCT since both of them are phase contrast X-ray imaging approaches, yet its achievable resolution still needs to be improved. As a comparative approach, SBFSEM proves to be a qualified candidate to reveal ultra-fine structures, such as that of the iron oxide alkyd paint, since it has extremely high-resolution naturally adopted from electron microscopy. The focused ion beam (FIB) tomography should be another proper tool to acquire 3D structures of coating samples, and could be employed in future work.

However, when presented with a phase object, the capabilities of TXM become quite limited, it cannot well resolve the contrast among different components in the phase samples, for instance, aluminium flakes, talc fragments and epoxy resin in the aluminium epoxy marine coating. PXCT, currently, is still a time-consuming method which, normally, would use about 24 hours of synchrotron X-ray beamtime to obtain a fully qualified 3D structure of a volume around  $30 \times 30 \times 30 \mu\text{m}^3$ . The X-ray holo-tomographic approach still needs to be further developed to get higher spatial resolution. Both SBFSEM and FIB tomography are destructive, which would induce physical damage to the samples and generate artefacts in the acquired images. Especially the SBFSEM whose imaging process involves direct mechanical contact with the imaging surfaces of specimens, this would have higher possibilities to produce the artificial effects such as shape deformation of features.

According to the experiments we carried out and the results presented in the dissertation, we draw these general conclusions, at least for the imaging of coatings: when facing an amplitude object, for example, silver epoxy adhesive, TXM should be employed for 3D spatial structural investigation because TXM can provide high-contrast images to these samples in relatively a short time. When a phase object is the target, PXCT or X-ray holo-tomography would be the best candidate for the 3D structure characterization since either of them can generate sufficient phase contrast to overcome the weak X-ray absorption differences among different components. However, currently, PXCT can reach higher resolution than the X-ray holo-tomography, yet the latter way has simpler experimental set-up. While facing a specimen such as iron oxide alkyd paint, which is neither a typical amplitude sample, nor a typical phase sample, and has tiny particles sized at a few hundreds of nanometre level, the best choice of measurement method depends on the experiment requirement. If high resolution 3D spatial structures are needed, SBFSEM or FIB tomography should be used as they can provide higher resolution than the X-ray imaging methods, and can even resolve single particles in the materials. If quick 3D imaging needed, the TXM is capable of the task. If quantitative information required, PXCT or X-ray holo-tomography needs to be employed for the purpose.

Presently, (full-field) transmission X-ray microscopes are publically available at many facilities based on either synchrotron X-ray sources or laboratory X-ray sources. Some of them are listed here: beamline 32ID-C at Advanced Photon Source of the Argonne National Laboratory; beamline X8C at National Synchrotron Light Source II of the Brookhaven National Laboratory; beamline 6-2c at the Stanford Synchrotron Radiation Lightsource of the Stanford University; beamline U7A at the National Synchrotron Radiation Laboratory, Hefei, China and the laboratory X-ray source based Xradia's NanoXCT at the Henry Mosley X-ray Imaging Centre of the University of Manchester. Actually, more TXM based beamlines are

under construction or in the development plans of several other synchrotron radiation X-ray facilities. Currently, the PXCT experiments can only be performed at cSAXS beamline at the Swiss Light Source, Paul Scherrer Institute. X-ray holo-tomography experiment can be carried out at quite a few beamlines world-wide based on free-propagation phase contrast mechanism, for instance, beamlines ID-22 and ID-19 at the European Synchrotron Radiation Facility, Grenoble, France; beamline BL13W1 at the Shanghai Synchrotron Radiation Facility, Shanghai, China. Nowadays, SBFSEM system with 3View unit, is still not a broadly-available tool for the general public. There are two 3View unit assembled SEMs accessible at the University of Manchester, one more such instrument is available at the University College London in the UK. Because of its low cost and wide accessible sample range, this method is becoming more and more popular. The FIB instrument is a quite common tool in those nanotechnology oriented research facilities such as my home institute, London Centre for Nanotechnology, where there are two FIB-SEM dual beam systems available for the public.

Except the case when 3D results are needed, as discussed above, the wave-front modulation coherent X-ray diffraction imaging also presented its capabilities to reveal structures of coating samples and can reach the similar resolution as TXM. Although, it is currently a two-dimensional approach, it can be developed into a 3D one with some effort.

## **7.2 Future Work**

More detailed analysis on some of the obtained 3D images still needs to be carried out, such as quantitative size and volume analysis of silver particles in the silver epoxy adhesive. Furthermore, precise finite element simulations of the coating properties based on the actual segmented 3D spatial structures can be performed in the future as well, for example, thermal and electrical conductivity simulations of the silver epoxy adhesive samples using the

obtained structures can be executed to reveal the thermal and electrical conduction activities in the material.

Making a direct comparison of the 3D structures of the same region of the same sample from different imaging methods is an interesting project for the future. In order to reach this target, well-fabricated specimens had better be prepared, and probably an FIB tool needs to be used to perform the sample fabrications. The FIB-fabricated samples can be measured by non-destructive X-ray imaging methods first and then transferred to electron microscopes to do either SBFSEM or FIB (destructive) tomography measurements. Such work can provide stronger evidence to verify the reliabilities of different 3D imaging methods themselves. It will also give a more convincing comparison of the advantages and disadvantages of different methods, and to help to give guidelines to the coating researcher or imaging facility users about how to choose suitable investigation tools for their researches.

In-situ 3D research of the coating drying/curing process is another direction for future work. This work can be extremely important for the coating industry since it could reveal the whole coating film forming process which transfers coating composites into protective layers. To investigate these processes, specific sample holders would need to be designed, for instance, sample holders for liquid or for high temperature measurements, and only non-destructive techniques can be used in such time-resolved experiments.

Developing the wave-front modulation coherent X-ray diffraction imaging method into a “single-shot” imaging approach for extended samples is an important topic for future work. The “single-shot” X-ray imaging system has great potential in studying structures, such as nano-objects, by using the 4th generation light sources, for instance X-ray free electron lasers (XFELs) which have a very high potentiality to damage samples. Another direction would be to combine image stitching technique with “single-shot” imaging to provide an efficient and

effective imaging method for objects of unlimited size, at least theoretically. If a square illumination could be used for extended sample measurement, the efficiency of the method could be further improved because, compared with the common circular illumination, the overlapping of a square illumination could be more effective and simpler.

# Curriculum Vitae

**Bo CHEN**

Date of Birth: 23rd December, 1983

## Education and Research Experience:

M.Phil./PhD: London Centre for Nanotechnology (LCN) and Department of Physics & Astronomy, University College London (UCL), London, the U.K., 2008.09-

Topic: Investigation and analysis of 3-dimensional spatial nano-structures of coatings by X-ray imaging. Experiments have been designed and performed at synchrotron radiation facilities such as APS at the ANL, ESRF, SLS and NSRL (China).

Supervisor: Prof. Ian K. Robinson

Master S.: School of Materials Science and Engineering, Tongji University, Shanghai, China, 2005.09-2008.03

Topic: Quantitative analysis of cement & its hydration products by X-ray powder diffraction.

Supervisor: Prof. PeiMing Wang

Bachelor S.: Department of Chemical Engineering, Wuhan University of Science and Engineering (presently Wuhan Textile University), Wuhan, Hubei, China, 2001.09-2005.07

Topic: Worked on synthesis and structure analysis of organic metal coordination compound crystals with Prof. HaiLiang Zhu from 2003 to 2005.

## Grant/Project:

- Co-Investigator of the National Science Foundation of China for Distinguished Young Scholars (Grant No. 51102181): Investigation of 3-dimensional spatial structures of composite cement by synchrotron X-ray computed tomography, 01/2012-12/2014

## Awards and Honours:

- Nominee of the Werner Meyer-Hse Memorial Award, 11<sup>th</sup> International Conference on X-ray Microscopy, 2012
- Young scientist bursary of the 4th European XFEL users' meeting, 2010
- Dorothy Hodgkin Postgraduate Awards (EPSRC-UK/UCL), 2008
- Annually travel support from the AkzoNobel Corporate, 2008-2011

- Recommended Excellent Postgraduate (Master) Dissertation, Tongji University, 2008
- 3 First-class Scholarships, Wuhan University of Science and Engineering, 2002-2005
- Excellent Student Model, Wuhan University of Science and Engineering, 2004-2005
- Excellent Student Leader, Wuhan University of Science and Engineering, 2002-2003
- Futian Scholarship, Wuhan University of Science and Engineering, 2004-2005
- Huali Scholarship, Wuhan University of Science and Engineering, 2003-2004
- Gaoshi Scholarship, Wuhan University of Science and Engineering, 2002-2003

#### **Social and Work Experience:**

- Member of Departmental Staff Student Consultative Committee, LCN/UCL, 2009-
- BASF (China) Chemical Company as Technical Service Engineer, 2008.03-2008.09
- Interned in WACKER Polymer Materials (Shanghai) Co. Ltd. 2006.07-2006.08

#### **Hobby:**

Playing tennis, entered quarter final of London Universities Grand Slam 2010

#### **Publications:**

1. Ying Zou, Bo Chen, Hua-Li Song, Lu-Lu Tang, Zhong-Duo Xiong and Hai-Liang Zhu. Crystal structure of {N-[2-(2-hydroxyethylamino)ethyl]-2-fluorobenzaldimine}-(3,5-dinitrobenzoato)silver(I) – water (1:0.25),  $\text{Ag}(\text{C}_7\text{H}_3\text{N}_2\text{O}_6)(\text{C}_{11}\text{H}_{15}\text{FN}_2\text{O})\cdot 0.25\text{H}_2\text{O}$ , *Zeitschrift Fur Kristallographie New Crystal Structures*, 2004, 219(3): 261–262.
2. Zhong-Lu You, Bo Chen, Hai-Liang Zhu and Wei-Sheng Liu. Aqua[2-(pyridin-2-ylmethyl iminomethyl)phenolato-k<sup>3</sup>N,N',O]copper(II) nitrate monohydrate, *Acta Crystallographica Section E Structure Reports Online*, 2004, E60, m884-m886.
3. Ji-Long Ma, Li Yang, Bo Chen, Ying Zou, Fan-Jin Meng and Hai-Liang Zhu. Crystal structure of bis[N,N'-bis(2-fluorobenzylidene)ethylenediamine]silver(I) 4-chlorobenzoate 4-chlorobenzoic acid,  $\text{Ag}(\text{C}_{16}\text{H}_{14}\text{N}_2\text{F}_2)_2(\text{C}_{14}\text{H}_9\text{O}_2\text{Cl}_2)$ , *Zeitschrift Fur Kristallographie New Crystal Structures*, 2004, 219(2):161-162.
4. Su-Yue Li, Zhong-Lu You, Bo Chen, Yong-Shan Lin, Zhong-Duo Xiong and Hai-Liang Zhu. trans-Bis{1-[3-(cyclohexylamino)propyliminomethyl]-2-naphtholato-k<sup>3</sup>O,N,N'}-cobalt(III) perchlorate, *Acta Crystallographica Section E Structure Reports Online*, 2004, E60, m999–m1001.
5. Sheng-Hui Chen, Sheng-Fang Li, Ying Zou, Li Yang, Bo Chen and Hai-Liang Zhu. Crystal structure of 1,3-di[2-(4,5-dihydrooxazole)]benzene,  $\text{C}_{12}\text{H}_{12}\text{N}_2\text{O}_2$ , *Zeitschrift Fur Kristallographie New Crystal Structures*, 2004, 219(2): 153-154.

6. Si-Chang Shao, Zhong-Lu You, Zhong-Duo Xiong, Bo Chen and Hai-Liang Zhu. 2-Nitrobenzaldehyde salicylhydrazone, *Acta Crystallographica Section E Structure Reports Online*, 2004, E60, o2187–o2188.

7. 王培铭, 陈波, 吴建国. 水泥浆体中钙矾石形成发展的 X 射线衍射原位测试法. *材料导报*, 2007, 21(12A): 8-10.

8. B. Chen, F. Zhang, F. Berenguer, R. J. Bean, C. M. Kewish, J. Vila-Comamala, Y. S. Chu, J. M. Rodenburg, and I. K. Robinson. Coherent X-ray Diffraction Imaging of Paint Pigment Particles by Scanning a Phase Plate Modulator, *New Journal of Physics*, 2011, 13: 103022.

9. B. Chen, M. Guizar-Sicairos, G. Xiong, L. Shemilt, A. Diaz, J. Nutter, N. Burdet, S. Huo, J. Mancuso, A. Monteith, F. Vergeer, A. Burgess and I. Robinson. Three-Dimensional Structure and Percolation Properties of a Barrier Marine Coating, submitted to *Nature Communications* (2012).